Fundamental Studies of MALDI with An Orthogonal TOF Mass Spectrometer

by

Hui Qiao

A dissertation

submitted to the Faculty of Graduate Studies

in partial fulfillment of the requirements for the degree of

Doctor of Philosophy

Department of Physics and Astronomy

University of Manitoba

Winnipeg, Manitoba, Canada

Contents

Abstract

The interaction between the matrix and analyte molecules are studied with a high resolution MALDI imaging technique in an orthogonal-injection time of flight (TOF) mass spectrometer. The analyte incorporation and distribution patterns have been clearly demonstrated. Purified protein analytes were found to be homogeneously incorporated in large single crystals of DHB and sinapinic acid matrices, with no evidence for preferred crystal faces. Segregation of some species was observed and appeared to correlate with analyte hydrophobicity, and to a lesser extent analyte mass or mobility. Similar segregation phenomena were observed with confocal laser scanning microscopy of the same analytes labeled with fluorescent dyes in 2,5-DHB single crystals. The above investigations may shed some light on optimizing sample preparation with different matrices.

The influence of incident laser parameters on sensitivity in MALDI has been investigated using orthogonal-injection TOF instruments. A qualitative comparison was first made between the beam profiles obtained with a N_2 laser and a Nd:YAG laser using 2-m long optical fibers. The N_2 laser gives better sensitivity, consistent with a more uniform fluence distribution and therefore better coverage of the N_2 laser profile. Most of the difference disappears when a 30-m long fiber is used or when the fibers are twisted during irradiation to smooth out the fluence distribution. In more systematic measurements, the total integrated ion yield from a single spot (a measure of sensitivity) was found to increase rapidly with fluence to a maximum, and then saturate or decrease slightly. Thus, the optimum sensitivity is achieved at high fluence. For a fluence near threshold, the integrated yield has a steep (cubic) dependence on the spot size, but the yield saturates at

higher fluence for smaller spots. The area dependence is much weaker (close to linear) for fluence values above saturation, with the result that the highest integrated yields per unit area are obtained with the smallest spot sizes. The results have particular relevance for imaging MALDI, where sensitivity and spatial resolution are important figures of merit.

Finally the detection properties of the MCP detector were studied with a hybrid MCP and CuBe venetian blind converter detector. The measurements show that the detection efficiency of the MCP drops with the increasing of ion mass and the decreasing of the ion energy. For transferrin (79,500 Da), the relative detection efficiency of the MCP is about 40% at 10.6 keV and it decreases to about 5% at 4.6 keV. The secondary electron emission coefficient of the MCP shows a linear dependence on mass and a power law dependence on velocity ($\sim$3.2). No clear velocity threshold is observed for secondary electron emission.

Acknowledgments

I am grateful to my supervisor, Dr. Werner Ens, to give me the opportunity to join in the family of mass spectrometry. I would like to thank for his continuous help, advice and guidance in my research. Whenever I got stuck in the project, his brilliant suggestions always help me get it through. Without his encouragement and constant guidance, I could not have finished this thesis. I am also grateful to Dr. Standing to give me useful suggestions and supports on my research.

I would like to thank Victor Spicer for his consistent help. I am impressed by his broad knowledge in programing, electronics, and instrumentation. Without his help I cannot build the Voltage-to-Frequency converter circuit from scratch. I enjoyed the time of working with and learning from him.

I would like to thank Dr. Vladimir Collado and Dr. Gamini Piyadasa for the collaboration and helpful discussion. I would also like to thank Dr. Oleg Krokhine to patiently teach me some basics about proteomics. I am also thankful to Dr. Lynda Donald for her good suggestions in my research.

I also would like to thank our mechanical technician Mr. Ken Williams for his help. Thanks Mr. Gilles Roy for his consistent support.

My very special thanks to all who are always in my heart - my beloved wife Jing, her understanding, encouragement and constant support are the most important motivations which help me finally finish my study. Whenever I encounter some difficulties or feel depression with my research work, she always gives me good suggestions and consistent

encouragements to work them out. Everyday talking on the phone becomes our happiest time because we are not staying together during our Ph.D. studies since we got married. Although this period of time is tough for us, I always treasure our loves every moment. I am also indebted to my and my wife's parents, brothers for their love, unconditional support, and encouragement. This thesis will be the best gift for them.

List of Tables

Chapter 1

Introduction

1.1 History of time of flight mass spectrometry

Time-of-flight mass spectrometers work on the simple physical principle that ions with a constant energy, will separate according to their mass when they are injected into a field free flight path simultaneously. The flight path is in vacuum, therefore no energy loss of ions is involved through collisions. The measurement of flight-time starts when the ions are injected into the flight path and stops when each ion strikes the detector, giving the total flight-time for ions of a particular mass. The flight-time can be easily converted to mass values according to the basic physical relationship:

$$(m/q) = (\frac{2eV}{D^2})t^2 \tag{1.1}$$

where eV is the constant energy of the ions, q is the number of charge, D is the length of the flight path, and t is the total flight-time.

The concept of the time-of-flight mass spectrometer was proposed by Stephens in 1946 [1]. In 1948, Cameron and Eggers reported the first experimental demonstration of a time-of-flight mass spectrometer [2]. In 1955, Wiley and McLaren introduced a time-of-flight

mass spectrometer utilizing a two-stage, pulsed ion extraction scheme that systematically addressed the effects of the initial spatial and velocity distributions of ions upon mass resolution [3]. The most innovative aspect of their scheme was the introduction of a time-delayed extraction, known as time-lag focusing. This compensated to some extent the initial velocity distribution of ions and improved the mass resolution. In 1973 Mamyrin and co-workers introduced an ion mirror (reflectron) in order to compensate for the kinetic energy distribution of ions [4], allowing longer flight-time so that increasing the time dispersion. However, the lack of technologies to facilitate the recording and processing of the mass spectrum in the nanosecond time-frame and the slowly developing ionization methods limited the development of the time-of-flight instruments.

Electron impact (EI) ionization had been used for the earlier time-of-flight mass spectrometers [2, 3]. This method required volatile molecules only, limiting the range of compounds that could be analyzed. This technique generates a continuous ion beam that was mostly used on quadrupole instruments. The pulsed electron-impact sources were also used with time-of-flight instruments, but the mass resolution and duty cycle were much lower.

Although the field desorption (FD) developed in 1960 [5] and the fast atom bombardment (FAB) developed in 1981 [6] allowed the nonvolatile molecules to be ionized without prior derivatization, the produced continuous ion source was not easily pulsed. These techniques did little to advance the technology or the popularity of the time-of-flight instruments.

In 1974, Macfarlane and co-workers introduced plasma desorption mass spectrometry (PDMS) [7], in which ^{252}Cf fission fragments produce secondary molecular ions from nonvolatile compounds. This is an intrinsically pulsed ion source. This technique utilized a time-to-digital converter (TDC) and had a profound effect on the role of time-of-flight mass spectrometers in biological research. It was capable of molecular measurements of peptides and small proteins in the mass range up to 20 kDa [8]. However, the wide acceptance of this technique continued to be limited by its low mass resolution. At about the same time laser desorption was introduced by Hillenkamp and co-workers [9]. It was later found useful for the structural analysis of biological compounds [10, 11], although

examples of high mass were scarce.

More recently, two new ionization techniques were introduced that have greatly strengthened the role of mass spectrometry in biological research. Matrix-assisted laser desorption/ionization (MALDI), introduced by Karas and Hillenkamp [12], enabled the molecular weight determination of proteins with masses exceeding 300 kDa [13], and had some similarity to that of Tanaka *et al.* [14]. Because this is a pulsed technique, it was most easily used on time-of-flight mass spectrometers. At about the same time the introduction of electrospray ionization (ESI) by Fenn and co-workers had enabled the ionization of the large and polar molecules by forming a series of multiply charged ions, with the molecular weight up to 130,000 Da [15, 16]. With the development of new ionization techniques, time-of-flight mass spectrometers experienced a rapid progress in the following years. Delayed extraction had been revisited for MALDI, providing extraordinary mass resolution for the axial injection time-of-flight instruments [17, 18]. A new approach for continuous ionization sources using orthogonal extraction [19, 20], which was first reported by O'Halloran *et al.* in 1964 [21], was redeveloped. It enabled the successful interfacing of electrospray ionization sources to the time-of-flight mass spectrometer [20, 22].

The orthogonal-injection TOF mass spectrometry also enabled the construction of hybrid quadrupole-TOF mass spectrometers [23, 24], in which a parent ion is selected in a quadrupole mass filter Q1, and is broken up in a collisional cell within an RF-only ion guide. The daughter ions then enter the TOF mass analyzer, which examines the complete mass spectrum without scanning (parallel detection). It has been rapidly embraced by the analytical community as powerful and robust instruments with unique capabilities such as high sensitivity, high resolving power, and high mass accuracy. In particular, they combined the high performance of orthogonal TOF analysis in both the mass spectrometry (MS) and tandem MS (MS/MS) modes, with the well accepted and widely used techniques of ESI and MALDI ionizations [25, 26].

Besides the development of the ionization techniques, many developments of the TOF mass spectrometer in the past decades, particularly the rediscovery of techniques like

delayed-time extraction and orthogonal-injection are due to the rapid advancement in the supporting technologies, which include the nano- and pico-second timing electronics and the fast processing and storage of digitized time signals affordable by advances in computer technology. It would be fair to say that the revolution in digital electronics has supported time-of-flight mass spectrometer to a greater extent than most other forms of mass spectrometry that rely more heavily on analog signal processing.

1.2 Ionization methods: MALDI/ESI

1.2.1 ESI

The idea of using electrospray dispersion of an analyte solution in a bath gas to produce ions for mass analysis originated with Dole *et al.* in 1968 [27]. They showed the possibility of producing intact ions of macromolecules into the gas phase directly from solution using an electrospray source. The potential of this technique for ionization of large non-volatile molecules was recognized after coupling ESI with mass spectrometers like quadrupole [15, 28] and magnetic sector [29]. The accessible mass up to 130,000 Da was obtained in the late 1980s [16, 30, 31], which demonstrated the experimental evidence of the power of this technique.

Some recent studies in ESI fundamentals were reviewed in [32]. In ESI mass spectrometry, a dilute solution of analyte is pumped through a capillary at a very low flow rate (0.1-10 μL/min). A high voltage (2-5 kV) is applied to the capillary. This voltage can be either negative or positive, depending on the analytes chosen. The applied voltage provides the electric-field gradient required to produce charge separation at the surface of the liquid. As a result, the liquid protrudes from the capillary tip in what is known as a 'Taylor cone' shown in Fig.1.1. When the solution that comprises the Taylor cone reaches the Rayleigh limit [33] (the point at which Coulombic repulsion of the surface charge is equal to the surface tension of the solution), droplets that contain an excess of positive or negative
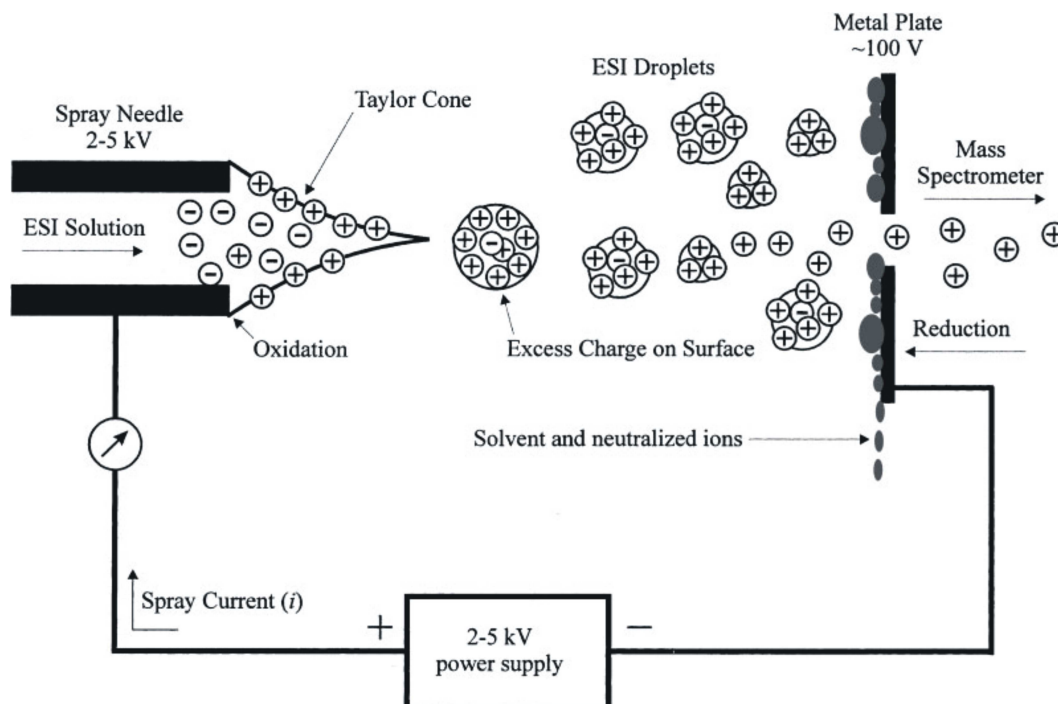
Figure 1.1: Schematic diagram of the electrospray ionization process. The analyte solution is pumped through a needle to which a high voltage is applied. A Taylor cone with an excess of positive charge on its surface forms as a result of the electric field gradient between the ESI needle and the counter electrode. Charged droplets are formed from the tip of the Taylor cone, and these droplets evaporate as they move towards the entrance to the mass spectrometer to produce free, charged analyte molecules that can be analyzed for their mass-to-charge ratio [32].

charge detach from its tip. These droplets move through the atmosphere towards the entrance to the mass spectrometer, and generate charged analyte molecules (ions). There are mainly two proposed mechanisms of ion generation. One of them is called 'Coulomb fission ' [27]. It assumes that the increased charge density due to solvent evaporation causes large droplets to divide into smaller and smaller droplets, which eventually consist only of single ions. A second mechanism, known as 'ion evaporation', assumes that the increased charge density that results from solvent evaporation eventually causes coulombic repulsion to overcome the liquid's surface tension, resulting in a release of ions from droplet surfaces [34]. Regardless of the mechanisms by which they are produced, the ESI process generates vapor phase ions that can be analyzed for their mass-to-charge ratio within the mass spectrometer.

In electrospray processes, the ions observed may be quasimolecular ions created by the addition of a proton (a hydrogen ion) and denoted $[M + H]^+$, or of another cation such as sodium ion, $[M + Na]^+$, or the removal of a proton, $[M - H]^-$. Multiply-charged ions such as $[M + 2H]^{2+}$ are often observed. For large macromolecules, there can be many charge states, occurring with different frequencies; the charge can be as great as $[M + 50H]^{50+}$, for example. The formation of ions in electrospray is somewhat analogous to acid-base reactions. Redox reactions do occur and a circuit with measurable current flow exists, but atomic and molecular ions are the primary carriers of charge in the solution and gas phases.

The ESI process takes place at atmospheric pressure. Because mass analysis can only be accomplished at low pressure, it is necessary to transfer ions from atmospheric pressure region to a low-pressure region before they can be analyzed by the mass spectrometer. Generally the differential pumping is employed to achieve it, such that the mass spectrometer consists of separate chambers at decreasing pressures.

Because the ESI process produces neutral species, ions, and clusters of ions with neutrals, the first challenge that must be overcome in introducing ions into the vacuum region is to separate the ions from the neutrals and to accomplish complete desolvation. Before ions even enter into the mass spectrometer, droplet formation can be aided by the coaxial flow of neutral gas (known as sheath gas) around the needle tip. It also aids in droplet desolvation [28]. Off-axis positioning of the spray needle is also helpful to the separation of ions from neutrals because the outer region of the spray generally consists of smaller, lighter, more desolved droplets [33]. A dry nitrogen 'curtain' gas, which is normally applied just behind the first orifice in the mass spectrometer, and a heated capillary [35] can also facilitate the desolvation process and help to accomplish the declustering of ions from neutrals.

1.2.2 MALDI

The use of a matrix to help ionization of macromolecules with laser desorption was proposed by two groups: Koichi Tanaka [14] and Michael Karas and Franz Hillenkamp [12] in the late 1980s. Tanaka used a mixture of ultra fine metal powder in glycerol as a matrix, however this method is not used currently for biomolecules analysis. Karas and Hillenkamp used organic compounds as the matrix, and they named this method as matrix-assisted laser desorption/ionization (MALDI) which is widely used today in mass spectrometry for large, nonvolatile biomolecules, in particular peptides, proteins, oligonucleotides, and oligosacchariddes. The accessible mass range of molecular ions has been extended up to 300,000 Da [13]. Unlike the ESI technique producing a continuous ion beam, MALDI is inherently a pulsed ion source which makes it directly suitable for the time-of-flight mass spectrometer.

The procedure of the MALDI technique is relatively simple. A small droplet of the mixture solution of the analyte and matrix is deposited onto the target (normally a conductive plate). After the crystallization of the sample droplet, the sample is then loaded into the mass spectrometer and irradiated by the laser beam. The matrix as an intermediate medium absorbs the laser energy and transfers it to the analyte molecules, which allows the desorption and ionization of the analyte molecules. The resulting ions will then be extracted from the ion plume and guided into the mass analyzer through the applied acceleration voltage. A schematic diagram of MALDI source is shown in Fig.1.2. The generally used wavelengths in MALDI are within the UV and IR ranges. Corresponding matrices have been chosen for each wavelength range. The general rule of thumb for choosing a matrix is that the matrix should have strong absorption of laser energy at the particular wavelength. The key functions of the matrix have been generally accepted: first, the matrix is essential to dilute, isolate, and incorporate the analyte molecules; second, the matrix must have strong absorption of laser energy to disintegrate the matrix-analyte solid; third, the matrix must be easy to sublime to release the ion plume into the vacuum.

Although MALDI has broad applications in the biological analysis, its underlying mech-
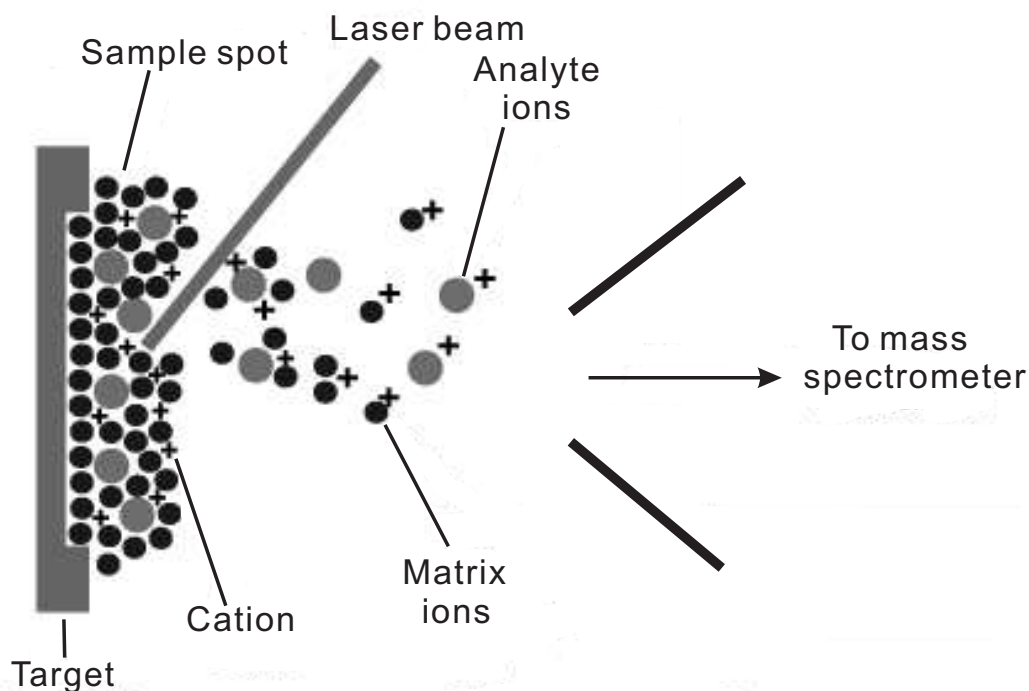
Figure 1.2: Schematic of the MALDI ionization process. The prepared sample droplet is deposited onto the target. When the laser beam irradiates on the sample spot, the matrix absorbs the laser energy and transfer it to the analyte molecules, resulting in the desorption and ionization of analytes. The ionized analyte molecules will be transmitted to the mass spectrometer for their mass-to-charge ratio analysis.

anisms are still not well understood. Most of the developments are rather dependent on the empirical approaches for sample handling, pretreatment, and preparation according to the class of analytes investigated. It is difficult to completely understand the mechanisms of MALDI due to a large number of variables related to this process. For the laser system it has different laser wavelengths, pulse energy and duration, laser spot size and beam profiles. There are different matrices, different classes of analyte molecules, and different sample preparation methods. The mass spectrum can also be recorded either in the positive or negative ion mode. All these parameters affect the mass spectrum through the ion formation process. Various aspects of the phenomenon have been studied, either from a physical point of view [36–41] or from a chemical or thermodynamic one [42–45]. The influence of these parameters on the ion desorption of MALDI process has been reviewed

by Dreisewerd [46].

In a recent review paper about the ion formation in UV-MALDI by Knochenmuss [47], a two-step framework of ionization model was proposed. Primary ion formation or separation is the first step; ion-molecule reactions in the expansion of ion plume follow, giving rising to secondary ions which reach the detector. The various models for generation of primary ions are still somewhat divergent, but secondary reactions in some form are no longer controversial.

Primary ionization

For the primary ionization, the cluster model was proposed by the Karas group [48]. The ions were assumed to be largely preformed in the solid matrix based on the study of incorporation of analytes into the matrix crystal using the pH sensor dyes which shows that the solid samples tended to retain the color of the original solution, indicating that the dye molecules had the same de/protonation state as in solution [49, 50]. These preformed ions will experience charge separation, proton transfer, and charge reduction during the photonionization and desolvation process.

Secondary ionization

Once the laser irradiates the sample, ionization only occurs shortly (< 10 ns) [51, 52] after the laser pulse because this requires concentration of energy. Later, the energy density is drastically reduced by conversion to heat and physical expansion, and the material begins to relax, both physically and chemically. The expansion of the material as it converts to a dilute gas is much slower, up to several microseconds. This allows completion of secondary reactions between the matrix and analyte molecules. Since the mobility of ions in the cluster is not as high as in the gas phase, the ion-molecule reactions between the matrix and analyte molecules are more intensive. This is increasingly important to measure gas-phase thermodynamic properties of matrices and analytes, since these have a major, even definitive, impact on the final spectrum. The secondary reactions such as the matrix suppression and analyte suppression effects, proton and electron transfer,
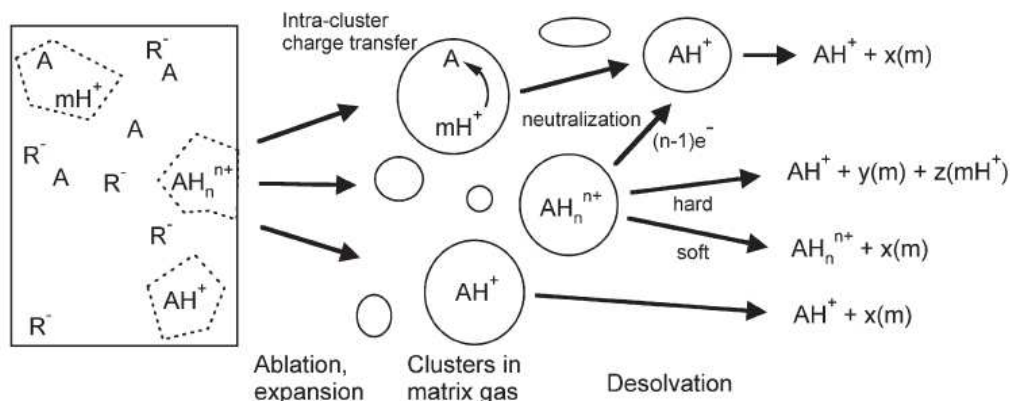
Figure 1.3: Sketch of the major processes proposed in cluster models of MALDI ionization. m=matrix, A=analyte, R_- = generic counterion. Preformed ions, separated in the preparation solution, are contained in clusters ablated from the initial solid material. Some clusters contain a net excess of positive charge, others net negative (not shown). If analyte is already charged, here by protonation, cluster evaporation may free the ion. In other clusters charge may need to migrate from its initial location, e.g. on matrix, to the more favorable location on analyte (secondary reaction). For multiply charged analytes, hard and soft desolvation processes may lead to different free ions. Neutralization by electrons or conterions takes place to some degree, but is not complete [47].

and cationization, seem to mainly happen in the expanded ion plume rather than in the primary ionization stage. These reactions are dominated by the matrix molecules as the most common collision partners, which lead to a certain commonality of MALDI behavior for all ion types. Fig.1.3 shows the major processes of ionization.

This two-step model has summarized the recent studies on the ion desorption mechanisms of MALDI. It can explain some of the most important features of the MALDI process. However, there are still some controversies about the generation of primary ions in the first step; besides the cluster model, a photoexcitation/pooling model has also been widely discussed [53].

1.3 Time-of-flight mass spectrometry

As briefly described in the section about the history of time-of-flight mass spectrometers, the development of instrumentation geometry experienced mainly two stages in terms of ion injection: axial TOF and orthogonal-injection TOF. Consistent innovations to improve mass resolution, mass accuracy, and sensitivity of the time-of-flight mass spectrometers were also developed.

1.3.1 Axial TOF

Prior to the rediscovery of orthogonal-injection TOF in the late 1980s, most of the TOF mass spectrometers were exclusively axial TOF. In the past, the main disadvantage of the axial TOF systems has been the poor mass resolution because of the initial spatial and velocity spreads of the ion source.

The influence of the initial ion conditions was first discussed by Wiley and McLaren in 1955 with ion sources produced by electron impact [3]. They proposed the 'space focusing' and 'time-lag focusing' techniques to correct the first or even higher order initial spatial and velocity spreads. The ion mirror (reflectron) was also introduced to compensate for the kinetic energy distribution of ions [4, 54], allowing longer flight-time therefore increasing the time spread and improving the mass resolution. More recently, time-delayed extraction (same as the 'time-lag focusing') has been re-visited in MALDI that minimizes the effect of initial ion velocity spread and allows much better resolution and mass accuracy in MALDI-TOF [17, 55].

There are some mathematical models describing the influence of initial ion conditions and instrument geometry on mass resolution [3, 56–58]. Normally these models are given under the assumption that the electric fields are uniform which allows the 'exact' calculations of flight-time. In this section, the general ideas about improving the mass resolution will be briefly described.
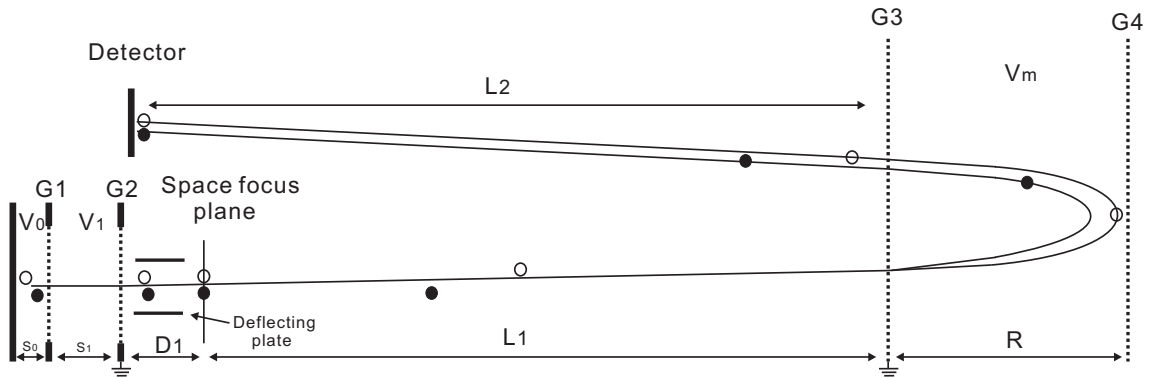
Figure 1.4: Schematic of an axial TOF mass spectrometer with a two-stage ion source and a single stage-ion mirror.

Space and velocity focusing

Fig.1.4 shows an axial TOF mass spectrometer with a two-stage acceleration region and a single-stage ion mirror, each with a uniform field. Assuming that ions have a pure spatial spread in the acceleration region, these ions are subject to 'space focusing', i.e. there is some plane beyond the acceleration region that ions of the same mass will reach at approximately the same time. This is because ions initially close to the grid acquire less energy in the acceleration region than those more distant ions and therefore are overtaken by the latter after traveling some distance determined by their original position and accelerating electric fields. In the special case of a single uniform field (single-stage acceleration region), the space-focus plane is a short distance $D1 = 2s_0$ beyond the acceleration region if the ions originate at an average distance s_0 inside it. If a two-stage acceleration region is used as shown in Fig.1.4, the position of the space-focus plane is at $D1 = 2(s_0 + \frac{E1}{E2}s_1)^{3/2}/s_0^{1/2}$ to the first order approximation. It can be adjusted by changing the ratio of the electric fields in the two regions. When the ions arrive at this plane, they will have a velocity spread because of the differing amounts of energy gained during acceleration, so the original spatial spread has been exchanged for a velocity spread.

The above technique does not give perfect spatial focusing, even in the ideal case, but the usual limitation results from an initial velocity spread in addition to the spatial spread. The worst case involves two ions at the same position but with velocities in opposite

directions when the extraction pulse is applied. The two ions will arrive at the space-focus plane separated by a 'turn-around time'.

To correct the initial velocity spread, 'time-lag focusing', now usually called delayed extraction can be used. In this technique, a delay is introduced between ion production and the application of the acceleration fields, during which the ions drift freely. For simplicity, consider ions starting with zero spatial spread, i.e. with a pure velocity spread. When the accelerating field is applied, the ions will be separated in space according to their velocity. Those ions with higher initial velocity will be closer to the end of the acceleration region, and will receive a smaller acceleration impulse. If the time delay and the amplitude of the accelerating voltage are adjusted properly, ions of the same mass will arrive at the focal plane at approximately the same time. However, the delayed time $\Delta t \propto (m/V)^{1/2}$ [58], which indicates a strong mass dependence so that the best resolution is achieved only over a relatively narrow mass range.

In the general case there may be both spatial and velocity spreads in the initial ion distribution, so some compromise is necessary to give optimum focusing. However, two currently popular ionization methods, ESI and MALDI, approximate the two limiting cases described above. Ions suitably injected from an ESI source have an appreciable spatial spread, but a very small velocity spread. A pure velocity spread is approximated by the geometry normally used for MALDI, since the MALDI ions are ejected from an equipotential target by a very short laser pulse. In a simple linear TOF spectrometer, resolution can be optimized in both cases by using a two-stage acceleration region and setting the accelerating fields so that the focal plane coincides with the plane of the detector.

Kinetic energy compensation with an ion mirror

As discussed above, both space focusing and velocity focusing can focus the ions of the same mass but with initial spatial and velocity spreads onto a focal plane at same flight-time. However, the ions will have a rather intense energy distribution on this focal plane. Compensating for the kinetic energy distribution provides an opportunity for improving

the mass resolution. This problem is alleviated by the introduction of a reflector or ion mirror, as first proposed by Mamyrin [4].

After the focal plane, the ion then travels freely to the detector. Assume the velocity of ion on the focal plane is v_z, for $L = L_1 + L_2$, the time spend in free flight is L/v_z, and the time spent in the mirror is $2mv_z/qE$, where E is the magnitude of the retarding electric field. If $v_z = v_0 + \delta$, we can expand as a function of (δ/v_0) to give a total flight-time:

$$t = \left(\frac{2mv_0}{qE} + \frac{L}{v_0}\right) + \left(\frac{\delta}{v_0}\right)\left(\frac{2mv_0}{qE} - \frac{L}{v_0}\right) + ... \tag{1.2}$$

Setting $2mv_0/qE = L/v_0$ removes the first order term in δ/v_0. Thus the reflector eliminates the effect of a velocity distribution δ to first order. Since $E = V/R$, where V is the retarding potential on the mirror (equal to the acceleration potential), R is the minimum length needed for the ion mirror to reflect ions back, the first order condition can be rewritten as follows:

$$\frac{2mv_0}{qE} = \left(\frac{L}{v_0}\right)$$
$$4\left(\frac{1}{2}mv_0^2\right)R = qVL$$
$$4R = L \tag{1.3}$$

Higher order terms can be removed by the use of more complicated electric fields, for example by the two-stage mirror described by Mamyrin, which is especially useful for an orthogonal-injection MALDI TOF because the kinetic energy distribution on the focal plane becomes much more intense due to the larger spatial spread of the ion beam. It has to be noted that the ion mirror does not in fact correct, or even reduce, the kinetic energy distribution. However, it does compensate for the kinetic energy distribution by ensuring that ions with differing energies (but the same mass) will arrive at the detector at the same time. In effect, it reproduces the ion packet (Δt) at the source or space focal

plane, but at much longer distance and at a later time (t), so that the mass resolution improves.
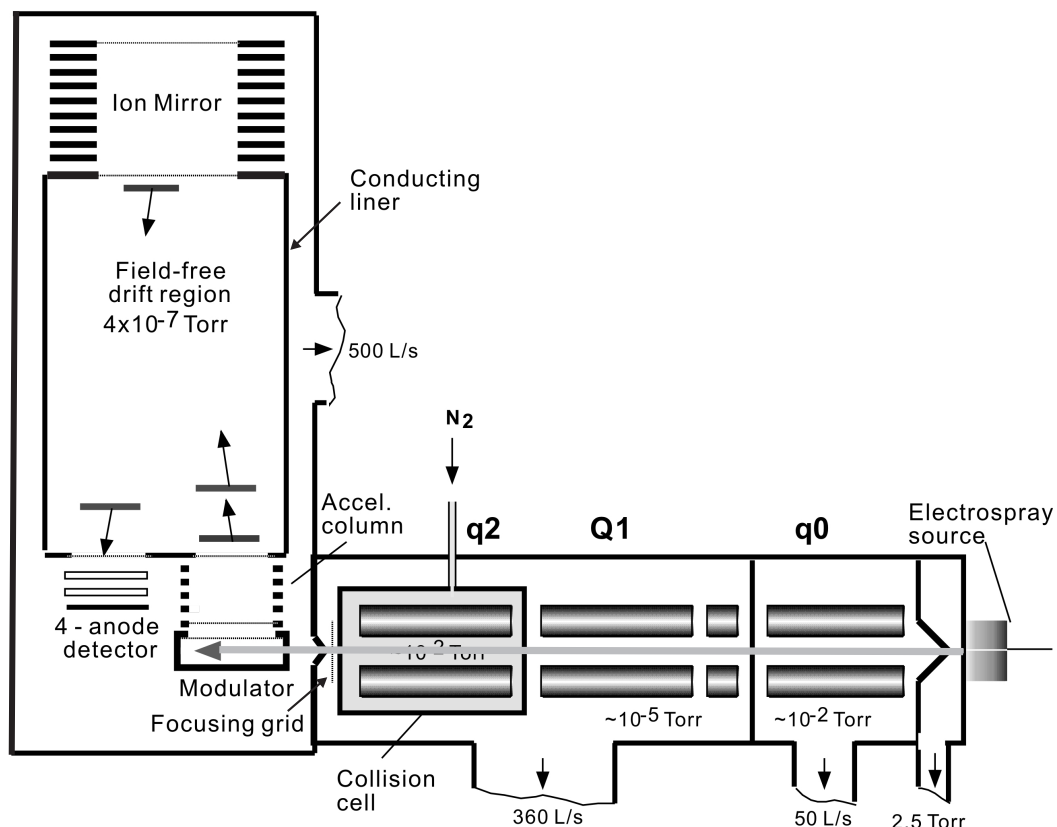
1.3.2 Orthogonal-injection TOF

As described in the section about the history of TOF mass spectrometry, the rediscovery of the orthogonal-injection TOF took place in the late 1980s by the groups of Guilhaus and Dodonov [19, 20]. In the Dawson and Guilhaus report [19], orthogonal extraction was used to improve both the duty cycle and mass resolution for a linear, electron impact (EI) ionization mass spectrometer. In the Dodonov report [20], orthogonal extraction was first used on a reflectron instrument to provide compatibility of the TOF mass analyzer with the continuous ion source formed by electrospray ionization [20]. MALDI ion sources were also used in orthogonal TOF later [59, 60]. Originally in orthogonal TOF instrument most of the ion sources were directly introduced into the TOF analyzer from the ion source through an interface that merely provides collimation to define the beam shape and by differential pumping to allow ions to be transferred from the source at atmospheric pressure to high vacuum in the spectrometer. The ion beam becomes divergent during the transmission from the ion source. This increases the spatial spread of the ion beam in the extraction region of the TOF analyzer. The initial velocities of the ion source are relatively independent of the analyte mass due to the 'supersonic expansion' in the cases of MALDI and ESI in which the ion beam enters the mass spectrometer from atmospheric pressure to high vacuum regions. This results in a mass-dependent energy distribution. Since the acceleration in the TOF analyzer contributes mass-independent energy, considerable mass discrimination in the ion trajectories is produced if the ion beam is injected into the TOF analyzer directly. The introduction of collisional cooling of the ions in a RF quadrupole ion guide at relatively high pressure can equilibrate the initial energies to near-thermal values [35]. This will produce a beam with a small spatial and energy spread, and these properties are almost independent of the original conditions of the ion beam delivered by the source. The mass resolution can also be improved. By reaccelerating the cooled ions to

a mass-independent energy, their velocity will be mass-dependent. So when injecting these cooled ion beams into the TOF analyzer, mass discrimination can be avoided. Another main advantage of orthogonal-injection TOF is that the decoupled ion source provides the possibility of studying the structure of interesting molecular ions by using a quadrupole to select parent ions and a collision cell for collisional induced dissociation (CID). A schematic diagram of a typical orthogonal-injection MALDI is shown in Fig.1.5. Recently the development and characteristics of orthogonal TOF mass spectrometry have been reviewed [25, 61]. In this section, some important features of the orthogonal TOF mass spectrometer will be discussed briefly.

Mass resolution and calibration

In axial MALDI TOF mass spectrometers, the mass resolution is mainly affected by the velocity distributions since the ions are generated from the same surface as discussed in the axial TOF section. Although the mass resolution can be improved by using time-delayed velocity focusing, it is limited only to a narrow mass range. The optimum focusing conditions also depend on laser fluence, matrix, and sample preparation methods. However, in orthogonal-injection TOF mass spectrometers the initial energy distributions of the ion source have been greatly reduced by collisional cooling of ions in a RF-quadrupole ion guide leaving only space spread of the ion beam in the extraction region. The initial conditions of the ion source are largely decoupled from the TOF analyzer. This provides more flexibility of using different laser fluence, matrix, and sample preparation methods. The mass resolution can be improved by correcting the space spread of the ion beam in the extraction region using space focusing. Combined with the ion mirror, the kinetic energy distribution of ions can also be compensated by ensuring ions with same mass but different energies arriving at the detector at the same time. The total drift length and flight-time of ions are also increased, allowing larger time spread. Finally, the resolution will then be limited in most practical situations by other factors, such as turnaround time or the temporal characteristics of the electronics.

Due to the collisional cooling of the ions in the quadrupole ion guide, the ion velocity is

Figure 1.5: Schematic of a typical orthogonal-injection time of flight mass spectrometer with an ESI ion source. The relative high pressure in the first quadrupole q0 provides collisional cooling of the ion beam. For the single ms application, Q1 and q2 are working in RF-only mode to generate a collimated ion beam. For the ms/ms application, Q1 is acting as a mass filter to select the interested ions. The fragmentation of interested ions is achieved by collisional induced dissociation (CID) in q2 by elevating the local pressure. The ion beam is injected into the time of flight region by the modulator with high repetition rate (up to 10 kHz). The ion mirror compensates the kinetic energy distribution of the ion beam to improve mass resolution. The ions will be detected by the MCP detector arranged in a Chevron configuration.

reduced to near thermal-energy. In the extraction region of the TOF analyzer, the ion velocity spread in the TOF direction is very low and nearly negligible. After the spatial spread is corrected by the space focusing, the total flight-time will be approximately independent of the initial spreads. So finally the flight-time can be written as:

$$t = A(\frac{m}{z})^{1/2} + B \qquad (1.4)$$

It shows that the total flight-time is linear to the $(m/z)^{1/2}$. The coefficient is determined only by the geometry of the instrument and the voltages on the ion source and ion mirror. Practically, the linearity of flight-time versus $(m/z)^{1/2}$ does not pass through the origin. There is a small offset of flight-time, which is due to the rise-time of the extraction pulse, the response time of the detector, and the time delay in the electronics (amplifier, CFD,etc.).

Therefore the calibration of the instrument becomes easier. Only two points with known masses can be used to determine the constants A and B. The calibration in an orthogonal TOF instrument is not affected by the initial conditions of the ion source and is much more accurate. However in an axial TOF, the calibration may be affected by the initial conditions such as the laser fluence, the sample preparation, and the matrix. Its calibration typically requires 3 or 4 mass peaks.

Duty cycle and efficiency

The duty cycle normally refers to the sampling duty cycle which is the ratio of the number of ions accelerated from the extractor to the number of ions that enter it. In the axial TOF, the duty cycle is about 100% since all the ions desorbed will be extracted to the TOF analyzer. But for the orthogonal-injection TOF, to avoid overlap of consecutive spectra, the extraction pulse cannot be applied until the slowest ion from the previous pulse has reached the detector. During the period between two extraction pulses, there will also be

ion packets continuously passing through the extraction region without being accelerated. The length of the extracted ion packet is Δl. The total length of the ion packet passing through the extraction region is D which is proportional to the axial velocity of the ion packet. So the duty cycle for certain m/z will be $\Delta l/D$. If the energy of the incoming ions is constant, the total length D of the ion packet passing through the extraction region will be inversely proportional to the $(m/z)^{1/2}$ of the ions. Therefore the higher m/z is, the larger the duty cycle is. Provided that the total length of the transmitted ion packet for the highest $(m/z)_{max}$ is D, the duty cycle can be expressed as

$$Duty \ cycle = \frac{\Delta l}{D} \sqrt{\frac{(m/z)}{(m/z)_{max}}} \tag{1.5}$$

In practice, Δl is normally the diameter of the aperture of the extractor; D is the distance between the centers of the extractor and the detector.

From the above discussion, the orthogonal TOF has discrimination against low m/z within a spectrum. Normally the higher m/z region of the spectrum contains the ions of greatest importance. The mass discrimination in orthogonal TOF is, therefore, favorable to the falling sensitivity as m/z increases which is characteristic of the quadrupole ion guide. In most orthogonal TOF mass spectrometers, the maximum duty cycle is typically about 30% for the largest ion in a spectrum. It varies with the m/z of the ions and the instrumental parameters. However, by trapping ions in the collision cell and then gating them out in short bursts synchronized with TOF extraction we can restore the duty cycle at the expense of mass range. Different modes of operation are achievable: from a 100% duty cycle restoration for a narrow mass range to $< 50\%$ duty cycle for a wider mass range [62].

Taking the transmission of grids and the detection efficiency of the detector into account, and assuming the duty cycle is measured at its maximum, the efficiency of the orthogonal

TOF mass spectrometer can be written as

$$E = T_G Y_{det} \frac{\Delta l}{D}$$
$$= T_G Y_{det} \Delta l f (\frac{m}{2zeV_{acc}})^{1/2} \tag{1.6}$$

where T_G is the product of the transmissions of all grids, Y_{det} is the detection efficiency of the detector, f is the extraction frequency, V_{acc} is the acceleration voltage. It is obvious that a higher duty cycle will improve the efficiency of the orthogonal TOF if the transmission of grids and detection efficiency are fixed. However for the axial instrument the efficiency would be higher because of the higher duty cycle (approaching 100% because $\Delta l = D$). It has no mass-discrimination either. But the lower resolution of the axial instrument would result in the signal being more widely distributed in time and this would decrease the signal-to-noise ratio to some extent.

Ion detection and recording

Ion detection of MALDI TOF mass spectrometers is normally accomplished by two microchannel plates (MCPs) arranged in the Chevron configuration [63]. The ion signals can be recorded by either analog or digital techniques. These two techniques are applicable in rather different experimental regimes, each of which has its own advantages.

For the analog measurement, transient recorders are commonly used. It records the ion current pulse from the detector. The amplitudes of the ion current pulse are digitized at a sampling rate of about 10^9 Hz. In the case of 8-bit transient recorders, the amplitudes are converted into numerical values of $0 - 255$. Since the ion current is recorded, the transient recorders have a wide ion rate range. This is particularly useful when multiple ions strike the detector at the same time. So they are more suitable in the axial TOF instruments because there are more ions injected per extraction pulse. Since the transient recorders create a digital profile of the ion detector signal, which represents the intensity distribution of the detected ions, a more accurate mass assignment can be achieved. However, there are also some limitations for this type of recorder. First, for each time

bin the amplitudes of the ion currents will be digitized. There can be many thousands of time bins and thus a significant amount of data generated. All these should be processed, stored and transferred to the computer before the next extraction pulse occurs. This limits the extraction frequency and then the duty cycle of the transient recorder. Second, the transient recorder is sensitive to the pulse shape produced by a single ion pulse at the detector. The ion pulse width $(1 - 2 \text{ ns})$ will broaden the mass peak in the mass spectrum, affecting the mass resolution.

For the digital measurement, time-to-digital converters (TDC) are mostly used. The recording system begins with a constant-fraction discriminator (CFD). Since the CFD triggers on the leading edge of the ion pulse, the advantage of a TDC system is its ability to eliminate any broadening of the ion pulse originating in the detector and amplifier. So the width and the shape of the detector output signal are not critical. The timing resolution with TDC is limited only by the ability of a CFD to define the time associated with a given pulse (independent of its amplitude). This can easily be achieved to considerably better than ns precision. And TDCs employ an ion-counting approach that eliminates the need for multi-bit conversion and for rapid storage of multi-bit data. The data transfer will be much faster than transient recorders. However the ion rate of the TDC is limited by the counting dead time (several ns). Therefore only the first ion can be recorded during the dead time even if more than one ion with the same m/z arrive at the detector. The result is the mass peak is distorted because the intense peaks and the portions of the spectrum adjacent to the intense peaks on the high time side are suppressed. Therefore there will be an observed shift in the measured ion arrival time towards shorter times. This shift directly translates to a smaller mass value. The mass assignment of that particular ion will be not accurate. One solution to the peak distortion is to reduce the total number of ions with each extraction pulse. The other one is to used multi-anode detectors to expand the ion rate of the TDC. The characteristics of the TDC are particularly suitable for the orthogonal TOF instrument, since the collisional cooling in the ion guide spreads the ion pulse out along the quadrupole axis, producing a quasi-continuous beam. The beam can be injected into the spectrometer at a high repetition rate up to 10 kHz, which

greatly reduces the number of ions within one extraction pulse. In most cases, the average count rate is much less than one ion per injection pulse per ion species, so the ion peak distortion recording with TDC is negligible in the orthogonal TOF.

1.4 Overview of the thesis

This thesis reports some systematically fundamental studies of the analyte distribution in MALDI samples, the influence of laser properties on the ion desorption/ionization in MALDI, and the ion detection properties of MCP detector using an orthogonal-injection MALDI TOF mass spectrometer. These studies are particular important for better understanding the mechanisms of MALDI mass spectrometry and help to improve its performance in practical applications.

It is divided into six chapters. In the first chapter, the history of time of flight mass spectrometry was reviewed; the two typically used ionization techniques: ESI and MALDI were briefly introduced; the working principles of TOF mass spectrometer including the axial and orthogonal TOF geometries were introduced; some important features such as space focusing, velocity focusing, duty cycle and efficiency, and ion detection and recording were discussed.

The second chapter describes the study of the analyte distribution in MALDI samples using a high resolution MALDI imaging mass spectrometer. We first mapped the analyte distribution on typical preparations of MALDI samples with common matrices. Then large single crystals of DHB and sinapinic acid were grown to examine the incorporation of analytes within the crystals. Confocal scanning microscopy was also used to examine the analyte distribution with dye-labeled proteins in single large 2,5-DHB crystals.

In the third chapter, the study of the influence of the laser beam profile on the ion desorption/ionization in MALDI is reported. The ion desorption performances of a N_2 laser and a Nd:YAG laser were first compared. The N_2 laser shows generally better sensitivity than the Nd:YAG laser. The laser beam profiles at the end of the fibers were

then studied for both lasers in order to figure out their different performances. The effects of twisting the fiber during irradiation or using longer fiber on the ion desorption performance were also studied.

In the fourth chapter, the study of the influence of laser fluence and spot size on the ion desorption/ionization properties in MALDI is reported. Different size fibers were used to achieve a wide range of laser fluence and spot size. The dependence of ion yield per shot and sensitivity on laser fluence were studied. The area dependence of sensitivity was discussed for low and high laser fluence regimes. The spot size related scanning mode in MALDI imaging was also discussed.

The fifth chapter describes the study of the detection efficiency of the MCP detector was studied with a hybrid detector consisting of an MCP and a CuBe venetian blind converter. The CuBe venetian blind converter is intended to provide normalization for studying the detection properties of MCP. The detection properties of MCP were studied with different ion masses and energies. The secondary electron emission properties were also analyzed.

In the last chapter, a summary is briefly made for the results obtained in the thesis.

References

[1] Stephens, W. E. *Phys. Rev.* **1946**, *69*, 691.

[2] Cameron, A. E.; Eggers, D. F. *Rev. Sci. Instr.* **1948**, *19*, 605.

[3] Wiley, W. C.; Mclaren, I. H. *Rev.Sci.Instrum.* **1955**, *26*, 1150–1157.

[4] Mamyrin, B. A.; Karatajev, V. J.; Shmikk, D. V.; Zagulin, V. A. *Sov. Phys. JETP* **1973**, *37*, 45.

[5] Beckey, H. D.; Schuelte, D. Z. *Instr.* **1960**, *68*, 302.

[6] Barber, M.; Bordoli, R. S.; Sedgwick, R. D.; Tyler, A. N. *J. Chem. Soc. Chem. Commun.* **1981**, 325.

[7] Macfarlane, R. D.; Skowronski, R. P.; Torgerson, D. F. *Biochem. Biophys. Res. Commun.* **1974**, *60*, 612.

[8] Cotter, R. J. *Anal. Chem.* **1988**, *60*, 781A.

[9] Hillenkamp, F.; Kaufmann, R.; Nitsche, R.; Unsold, E. *Appl. Phys.* **1975**, *8*, 341.

[10] VanBreemen, R. B.; Snow, M.; Cotter, R. J. *Int. J. Mass Spectrom. Ion and Phys.* **1983**, *49*, 35.

[11] Cotter, R. J. *Anal Chem.* **1984**, *56*, 485A.

[12] Karas, M.; Hillenkamp, F. *Anal. Chem.* **1988**, *60*, 2299–2301.

[13] Karas, M.; Ingendoh, A.; Bahr, U.; Hillenkamp, F. *Biomed. Environ. Mass Spectrom.* **1989**, *18*, 841.

[14] Tanaka, K.; Waki, H.; Ido, Y.; Akita, S.; Yoshida, Y.; Yoshida, T. *Rapid. Commun. Mass Spectrom.* **1988**, *2*, 151.

[15] Yamashita, M.; Fenn, J. B. *J.Phys.Chem.* **1984**, *88*, 4671–4675.

[16] Fenn, J. B.; Mann, M.; Meng, C. K.; Wong, S. F.; Whitehouse, C. M. *Science* **1989**, *246*, 64–71.

[17] Brown, R. S.; Lennon, J. J. *Anal. Chem.* **1995**, *67*, 1998–2003.

[18] Colby, S. M.; King, T. B.; Reilly, J. P. *Rapid Commun. Mass Spectrom.* **1994**, *8*, 865–868.

[19] Dawson, J. H. J.; Guilhaus, M. *Rapid Commun. Mass Spctrom.* **1989**, *3*, 155.

[20] Dodonov, A. F.; Chernushevich, I. V.; Laiko, V. V.; In *Proceedings of the 12th International Mass Spectrometry Conference*, 1991; p 153.

[21] O'Halloran, G. J.; Fluegge, R. A.; Betts, J. F.; Everett, W. L.

[22] Verentchikov, A. N.; Ens, W.; Standing, K. G. *Analytical Chemistry* **1994**, *66*, 126–133.

[23] Morris, H. R.; Paxton, T.; Dell, A.; Langhorne, J.; Berg, M.; Bordoli, R. S.; Hoyes, J.; Bateman, R. H. *Rapid Communications in Mass Spectrometry* **1996**, *10*, 889–896.

[24] Shevchenko, A.; Chernushevich, I.; Ens, W.; Standing, K. G.; Thomson, B.; Wilm, M.; Mann, M. *Rapid Communications in Mass Spectrometry* **1997**, *11*, 1015–1024.

[25] Chernushevich, I. V.; Ens, W.; Standing, K. G. *Anal. Chem.* **1999**, 452A–461A.

[26] Chernushevich, I. V.; Loboda, A. V.; Thomson, B. A. *J. Mass Spectrom.* **2001**, *36*, 849–865.

[27] Dole, M.; Mack, L. L.; Hines, R. L.; Mobley, R. C.; Ferguson, L. D.; Alice, M. B. *J. Chem. Phys.* **1968**, *49*, 2240.

[28] Bruins, A. P.; Henion, J. D.; Covey, T. R. *Anal. Chem.* **1987**, *59*, 2642.

[29] Aleksandrov, M. L.; Gall, L. N.; Krasnov, N. V.; Nikolayev, V. I.; Pavlenko, V. A.; Shkurov, V. A. *Dokl. Phys. Chem.* **1985**, *277*, 572.

[30] Covey, T. R.; Bonner, R. F.; Shushan, B. I.; Henion, J. D. *Rapid Commun. Mass Spectrum.* **1988**, *2*, 249.

[31] Smith, R. D.; Loo, J. A.; Barinaga, C. J.; Udseth, H.; In *paper presented at the 5th Symposium on LC-MS*, 1988.

[32] Cech, N. B.; Enke, C. G. *Mass Spectrom. Rev.* **2001**, *20*, 362.

[33] Taflin, D. C.; Ward, T. L.; Davis, E. J. *Langmuir* **1989**, *5*, 376.

[34] Iribarne, J. V.; Thomson, B. A. *J. Chem. Phys.* **1976**, *64*, 2287.

[35] Krutchinsky, A. N.; Chernushevich, I. V.; Spicer, V. L.; Ens, W.; Standing, K. G. *J.Am. Soc. Mass Spectrom.* **1998**, *9*, 569–579.

[36] Ens, W.; Mao, Y.; Mayer, F.; Standing, K. G. *Rapid Commun. Mass Spectrom.* **1991**, *5*, 117–123.

[37] Zhou, J.; Ens, W.; Standing, K. G.; Verentchikov, A. *Rapid Commun. Mass Spectrom.* **1992**, *6*, 671–678.

[38] Dreisewerd, K.; Schurenberg, M.; Karas, M.; Hillenkamp, F. *Int. J. Mass Spectrom. Ion Processes* **1995**, *141*, 127–148.

[39] Strupat, K.; Kampmeier, J.; Horneffer, V. *Int. J. Mass Spectrom. Ion Processes* **1997**, *169/170*, 43–50.

[40] Niu, S.; Zhang, W.; Chait, B. T. *J. AM. Soc. Mass Spectrom.* **1998**, *9*, 1–7.

[41] Chen, X.; Carroll, J. A.; Beavis, R. C. *J. Am. Soc. Mass Spectrom.* **1998**, *9*, 885–891.

[42] Ehring, H.; Karas, M.; Hillenkamp, F. *Org. Mass Spectrom.* **1992**, *27*, 472.

[43] Zenobi, R.; Knochenmuss, R. *Mass Spectrom. Rev.* **1998**, *17*, 337.

[44] Knochenmuss, R. *J. Mass Spectrom.* **2002**, *37*, 867–877.

[45] Knochenmuss, R.; Zenobi, R. *Chem. Rev.* **2003**, *103*, 441.

[46] Dreisewerd, K. *Chem. rev.* **2003**, *103*, 395–425.

[47] Knochenmuss, R. *Analyst* **2006**, *131*, 966–986.

[48] Karas, M.; Kruger, R. *Chem. Rev.* **2003**, *103*, 427–439.

[49] Horneffer, V.; Reichelt, R.; Strupat, K. *Int. J. Mass Spectrom.* **2003**, *226*, 117–131.

[50] Kruger, R.; Pfenninger, A.; Fournier, I.; Gluckmann, M.; Karas, M. *Anal. Chem.* **2001**, *73*, 5812.

[51] Puretzky, A. A.; Geohegan, D. B.; Hurst, G. B.; Buchanan, M. V.; Luk'Yanchuk, B. S. *Phys. Rev. Lett.* **1999**, *83*, 444.

[52] Leisner, A.; Rohlfing, A.; Rohling, U.; Dreisewerd, K.; Hillenkamp, F. *J Phys Chem B* **2005**, *109*, 11661–11666.

[53] Knochenmuss, R. *Anal. Chem.* **2003**, *75*, 2199–2207.

[54] Tang, X.; Beavis, R.; Ens, W.; Lafortune, F.; Schueler, B.; Standing, K. G. *Int. J. Mass Spectrom. Ion Processes* **1988**, *85*, 43–67.

[55] Vestal, M. L.; Juhasz, P.; Martin, S. A. *Rapid Commun. Mass Spectrom.* **1995**, *9*, 1044–1050.

[56] Laiko, V. V.; Dodonov, A. F. *Rapid Commun. Mass Spectrom.* **1994**, *8*, 720–726.

[57] Cotter, R. J. *ACS Professional Reference Books* **1997**, .

[58] Vestal, M.; Juhasz, P. *J. Am. Soc. Mass Spectrom.* **1998**, *9*, 892.

[59] Spengler, B.; Cotter, R. J. *Anal. Chem.* **1990**, *62*, 793.

[60] Krutchinsky, A. N.; Loboda, A. V.; Spicer, V. L.; Dworschak, R.; Ens, W.; Standing, K. G. *Rapid Commun. Mass Spectrom.* **1998**, *12*, 508–518.

[61] Guilhaus, M.; Selby, D.; Mlynski, V. *Mass Spectrom. Rev.* **2000**, *19*, 65.

[62] Chernushevich, I. V. *European Journal of Mass Spectrometry* **2000**, *6*, 471–479.

[63] Colson, W. B.; McPherson, J.; King, F. T. *Rev. Sci. Instr.* **1973**, *44*, 1694.

Chapter 2

Analyte distributions in MALDI samples using MALDI imaging mass spectrometry

2.1 Introduction

Since the introduction of matrix-assisted laser desorption/ionization (MALDI) mass spectrometry in 1988 [1, 2], it has increasingly become one of the most powerful analytical tools in biomolecular analysis [3]. Different matrices [4–6] and sample preparation procedures [7–9], have also been proposed, with significant differences in mass spectral sensitivity, resolution and reproducibility. It is generally accepted that the matrix absorbs the laser energy and undergoes a phase change, producing isolated intact gas-phase ions of the embedded analyte molecules. Despite the wide applications of MALDI MS, most of the understandings come from the empirical testing rather than from the underling physical and chemical processes. The mechanisms behind the interaction of matrix and analyte molecules inside the MALDI matrix crystal before ablation are still not fully understood.

The incorporation of analytes into MALDI matrices has been investigated by several laboratories [10–20]. Strupat *et al* showed that proteins are incorporated into slowly grown single crystals of 2,5-dihydroxybenzonic acid (2,5-DHB) and succinic acid, by analyzing redissolved crystals [10, 21]. Using X-ray crystallography, they also showed that the

crystal structure is unperturbed by the presence of the protein doping [10, 21], suggesting a solid solution (analyte molecules are solvated by the matrix molecules in the solid) [3]. The analyte incorporation via solid solution is also confirmed by using high resolution field emission scanning electron microscopy (SEM) with Au-labels as potential protein markers [14]. The incorporation of dye-labeled proteins in 2,5-DHB was later shown to be homogeneous, using confocal laser scanning microscopy, which also showed that labeled proteins are excluded from crystals of 2,6-DHB [18].

Beavis *et al.* studied the interaction of sinapinic acid with dye-labeled proteins and observed an inhomogeneous incorporation pattern resembling an hourglass shape [16]. They suggested that proteins are preferentially or exclusively incorporated into the more hydrophobic face of a single sinapinic acid crystal. However, Mitchell *et al.* have questioned these conclusions: they observed the identical hourglass shape zone with neat dye incorporation at the hydrophobic surface [22]. Moreover, Strupat *et al.* argue from crystallographic data that there are no major hydrophobic domains in succinic acid and DHB crystals, so incorporation of proteins in these crystals must be based on non-hydrophobic interactions [10]. Gluckmann *et al.* also ruled out that incorporation is driven by hydrophobic interactions by finding that the hydrophilic oligosaccharides get embedded into 2,5-DHB as well [23].

Dai *et al.* used confocal laser scanning microscopy to investigate the incorporation of analytes in 2,5-DHB and sinapinic acid matrix crystals formed by fast and slow evaporation methods [15]. The results show that uniform protein incorporation in the slowly grown crystals, but non-uniform distribution of protein analyte in dried droplet preparations. Their results also show evidence of analyte segregation in simple mixtures in crystals formed by fast evaporation.

Kruger *et al.* used pH indicator dyes to serve as molecular probes to inspect the color changes between matrix and analyte solution and the corresponding matrix crystals. It shows that the analyte's charge states do not change and also show the incorporation of the analytes to the matrix crystal [24].

Most investigations of analyte incorporation in matrices to date have involved the use of an intermediate label: dye-labeled proteins (horse skeletal myoglobin) [16] and pH indicator dyes [24], fluorescence-labeled proteins (fluorescein isothiocyanate (FITC) [15], Texas Red-labeled avidin) [14] and Au-labeled proteins [3]. These labels may affect the properties of analytes or the presence of unbound labels may mask the properties of the analyte [22]. Moreover, the use of labels introduces additional complexity to the experiment. For example, when using fluorescent materials in confocal laser scanning microscopy, the proper way of labeling proteins, removing the excess dyes, the pH dependence, the variations of the fluorescence intensity for different proteins, and the influence of the refractive index mismatches and the birefringence of the crystals all need to be carefully considered.

MALDI imaging mass spectrometry avoids all the problems described above [25, 26]. The technique was developed to analyze thin layer chromatograms [25], and for the study of biological tissue [27, 28], but clearly offers the most direct way to study the distribution of analyte in MALDI samples. However, most MALDI imaging systems have rather modest spatial resolution in the range of 100 μm. Garden and Sweedler improved this to about 25 μm to study the heterogeneity of different types of MALDI sample preparation [20], but this was not sufficient to study the incorporation of analyte in individual crystals. We have recently constructed a MALDI imaging instrument with spatial resolution in the range of 10 μm [29, 30], and have reported preliminary results of analyte incorporation in large MALDI crystals, demonstrating homogeneous incorporation of pure analytes, but segregation of the components of some mixtures [31]. More recently,Bouschen and Spengler have reported even better spatial resolution of about 1 μm [32], and have shown segregation of analytes in small 2,5-DHB crystals in dried-droplet preparations [33].

In this chapter, we report more detailed investigations of analyte distributions in MALDI matrices using a custom MALDI imaging mass spectrometer with better than 10 μm spatial resolution. We first map the analyte distribution on typical preparations of MALDI samples using the common matrices. Then large single crystals of DHB and sinapinic acid were grown to examine the incorporation of analytes within the crystals. For comparison,

some fluorescence microscopy is also used to examine the analyte distribution with dye-labeled proteins in 2,5-DHB crystals. Finally, some effects of laser ablation such as the decrease of ion signal and the increase of matrix clusters were studied, which might be related to the morphology change of the matrix crystal surface due to laser ablation.

2.2 Experimental

2.2.1 Instrumentation

Orthogonal-injection TOF

The experiments were performed on a modified Qstar mass spectrometer [34], supplied by MDS Sciex (Concord, ON, Canada), shown schematically in Fig.2.1. This is a typical orthogonal-injection TOF mass spectrometer with a collisional cooling ion guide. This geometry has some particular advantages. First, the ion plume is collisionally cooled due to the high pressure in ion source ($\sim$1 torr) and the first quadrupole region. The ion plume can be spread out along the the quadrupole axis after the collisional cooling, producing a quasi-continuous ion beam [35], which can be treated just like an electrosprayed ion beam. The orthogonal geometry makes it unnecessary to synchronize the laser pulse and the extraction pulse. So the ion beam can be injected into the TOF analyzer at a high repetition rate (up to 10 kHz) as in ESI-TOF, although the laser itself runs at only about 50 Hz. This reduces the number of ions in a single-time measurement by a factor of $\sim$10,000/50, and thus eliminates the problems of peak saturation and detector shadowing from intense matrix signals [36]. Second, due to the collisional cooling, the ion source is decoupled from the TOF mass analyzer, which makes the mass measurement independent of the initial spatial and velocity distributions of the ion plume. Thus, it provides greater flexibility when experimenting with different sample preparation methods and different laser wavelengths, pulse widths, and fluences. Third, a good quality ion beam with smaller spatial and velocity spread can be obtained after the collisional cooling. Combined with
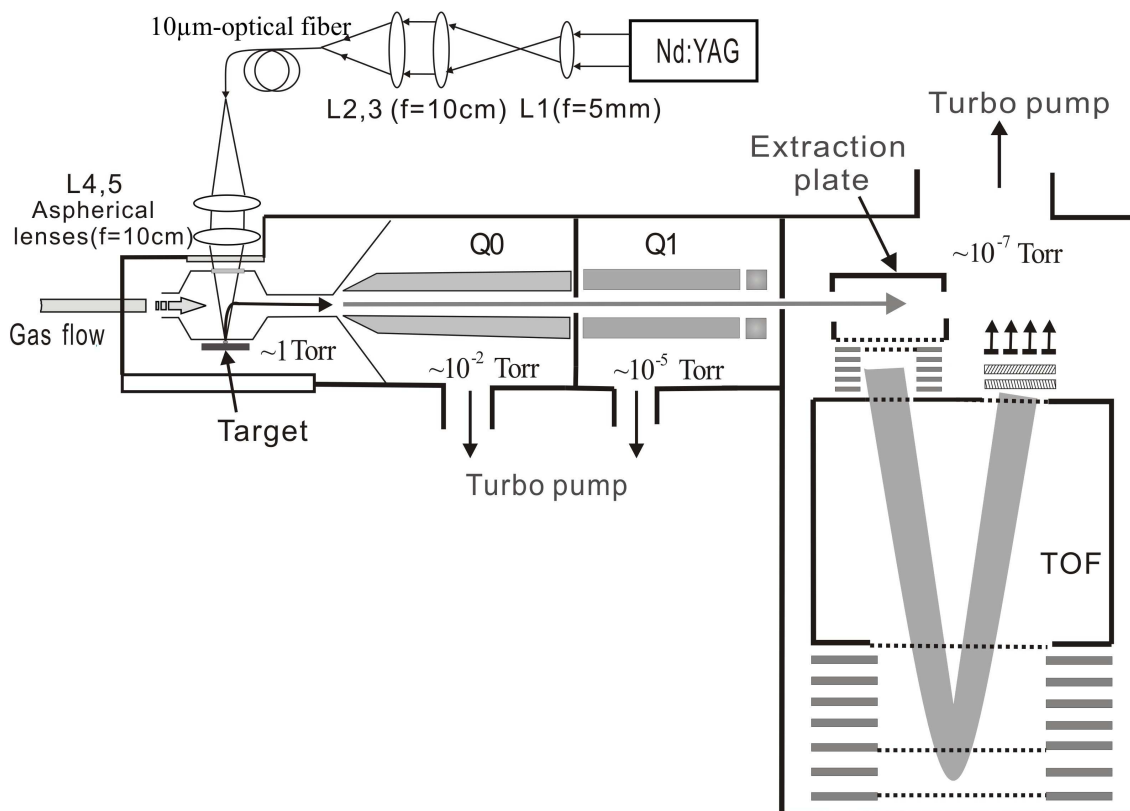
Figure 2.1: Schematic diagram of an orthogonal-injection MALDI imaging mass spectrometer. The laser beam was focused into the fiber by three lenses. L1: f = 5 mm, L2,3: f2 = f3 = 10 cm. The fiber output was imaged onto the sample plate by two aspherical lenses L4,5 (f4 = f5 = 10 cm) arranged in infinite conjugation. The laser beam is arranged normal to the sample target in order to achieve higher spatial resolution. The desorbed ions are driven into the ion guide by the combination of a smooth gas flow and electric fields. The pressure in the ion source is about 1 Torr. Both Q0 and Q1 are operated in RF-only mode.

the kinetic energy compensation of the reflector (two-stage mirror), the mass resolution can reach up to ~10,000. All these advantages are beneficial for the MALDI imaging experiment: for example, since the ion source is decoupled, the topology and charging effect of the sample is not going to affect the mass resolution; high repetition and high fluence lasers can be used to improve the sensitivity and data acquisition rate.

In this experiment, the laser beam from a Nd:YAG laser (wavelength: 355 nm, pulse width: ~8 ns, JDS Uniphase, model S355B-100Q, Manteca, CA) operated at 1 kHz repetition rate was coupled through a 3-lens optical system into 2-m long fiber optic patch cord, 10

μm in diameter (OZ Optics Ltd. Ottawa, Canada). The fiber had a step-index profile with a numerical aperture $\sim$0.22. Alignment was performed with an attenuated beam by maximizing the transmitted intensity, and then backing the fiber off about 10 to 20 μm to avoid damaging the end. The fiber output was imaged onto the target with two custom-made 10-cm focal length aspherical lenses (R. Mathews Optical Works, Inc., Poulsbo, WA, USA) arranged in infinite conjugation. This arrangement allowed the laser spot size to closely approximate the fiber diameter (10 μm). The target is mounted on a robotic microstepping 2D-positioner with a relative positioning resolution of 0.5 μm (PI-Physik Instrumente, L.P., Auburn, MA, USA). The image is generated by rastering the target with the laser in a fixed position. Two rf-only quadrupole ion guides were used, one with segmented rods to reduce transit time. The TOF portion was modified to operate with 11 kV acceleration voltage.

MALDI imaging ion source

In MALDI imaging experiments, spatial resolution is one of the most important parameters for evaluating the molecular mass distribution. The best spatial resolution is directly affected by the laser beam spot size. Currently, most applications of MALDI imaging experiments [27, 37, 38] are performed on axial-injection TOF instruments. The spatial resolution is typically 100 μm or worse. Spengler *et al.* [32] improved the spatial resolution down to < 1 μm using a specially designed objective lens with central bore, and focusing the laser beam onto the target normally with an axial TOF instrument.

Compared to the axial TOF instrument, some advantages of using orthogonal-injection MALDI TOF for imaging mass spectrometry have been discussed above. In an orthogonal-injection MALDI imaging instrument, the mass spectrum is independent of variations of sample properties (such as thickness) and sample preparation methods. And it also allows much greater flexibility for the laser properties such as the repetition rate, the fluence of the lasers, and the laser geometry. Some preliminary imaging experiments with an orthogonal-injection MALDI mass spectrometer have been reported by Hsieh *et al.* on a Qstar instrument(MDS Sciex, Concord, ON, Canada) [39]. However, the lateral resolution
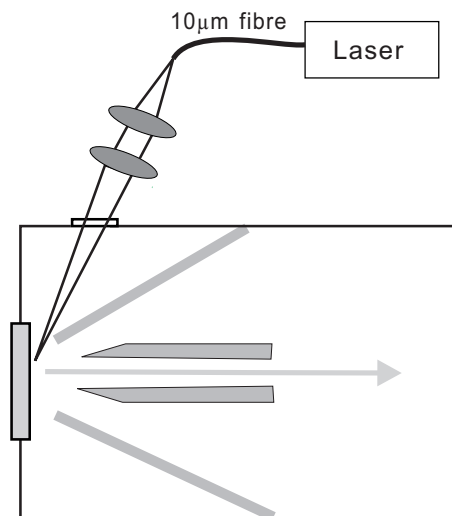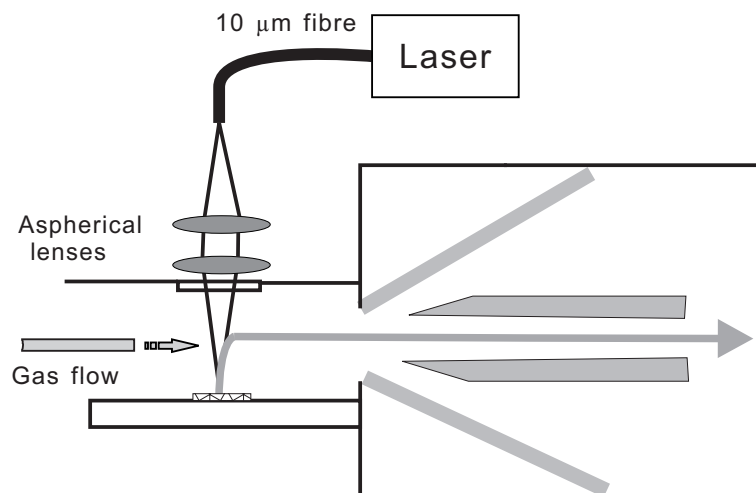
Figure 2.2: Schematic diagram of a typical MALDI ion source with glancing incidence of the laser beam. The incident angle is at about 60° with respect to the normal of the target. The laser beam spot is an ellipse instead of a circle making the spot size relatively larger.

is still limited to about 100 μm due to the glancing incidence of the laser beam.

The typical laser incident angles in the orthogonal-injection MALDI TOF mass spectrometer are ranging from 30 to 60 degrees with respect to the normal of the target as shown in Fig.2.2. In this case, the laser beam spot on the target is like an ellipse instead of a circle. The laser beam spot size is relatively larger.

In order to reduce the laser beam spot size and improve the lateral resolution of MALDI imaging, we have developed a novel MALDI imaging ion source shown in Fig.2.3 [29]. In this design, the sample target has been modified by rotating it by 90°. The incidence of the laser beam can be easily arranged normal to the target, so the minimum spot size can be achieved. By arranging the aspherical lenses in an infinite conjugation, the laser beam spot size is approximately equal to the size of the optical fiber about 10 μm in our experiment.

Desorbed ions are drawn into the ion guide through a 4 mm diameter cone by a combination of gas flow and an electric field set up by a small, segmented cell. The schematic diagram of the ion transmission in the ion source is shown in Fig.2.4. The electric fields
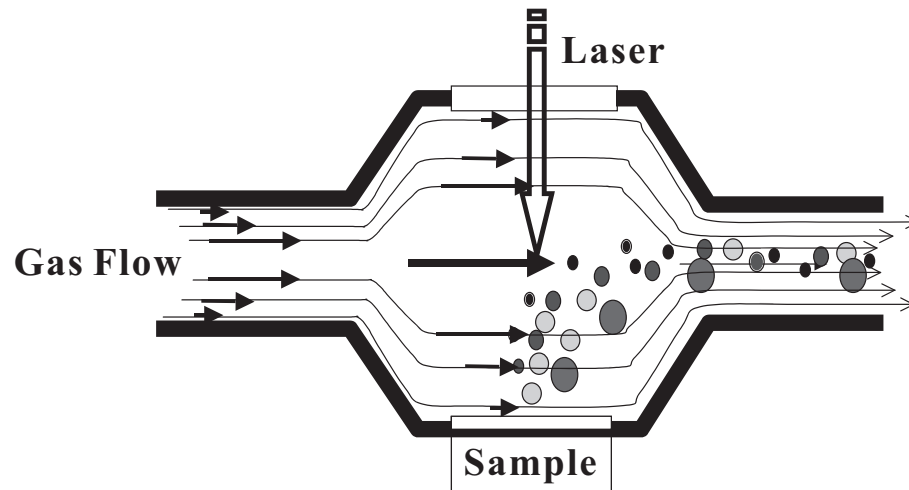
Figure 2.3: Schematic diagram of a MALDI imaging ion source with normal incidence of the laser beam. The output of the fiber is imaged 1:1 onto the target with two aspherical lenses. The minimum laser spot size can be achieved which is approximately equal to the size of the optical fiber.

from segmented electrodes (not shown) can provide a better focusing of the desorbed ions.
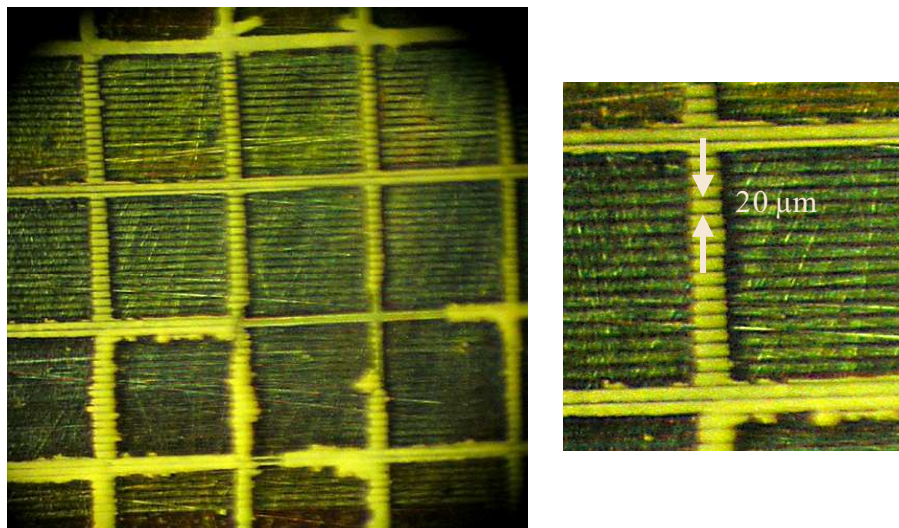
The spatial resolution of this setup was determined by examining samples deposited on nickel grid. Fullerenes were first evaporated onto a stainless steel plate to form a thin layer. A 70 lpi (line per inch) nickel mesh was coated with bradykinin and placed on top of the stainless steel plate. This sample was then scanned with the imaging setup. The beam damage on the sample can be examined with an optical microscope. As shown in Fig.2.5, the scan step was set as 20 μm, i.e. the space between two damaged tracks. It is clear that the width of the damaged track is smaller than half of the space between two damaged tracks, so the effective spatial resolution is better than 10 μm.

A 500 lpi nickel mesh with evaporated C60/C70 on target was also examined for the spatial resolution. In this case, wires are 10 μm, and the spacing is 50 μm. The microscopy and MALDI images are shown in Fig.2.6. The pixel is 5 μm $\times$ 5 μm. The image of wires (black lines) is clearly shown, so the spatial resolution is better than 10 μm, the fiber diameter.
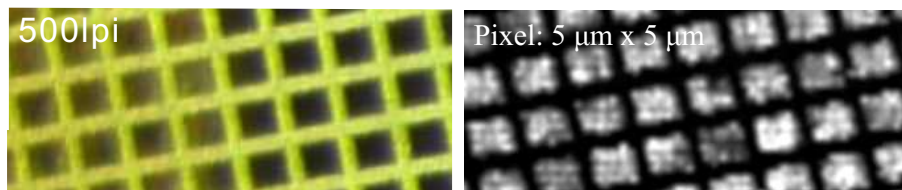
Constructing the MALDI images

Figure 2.4: Schematic diagram of the imaging ion source with orthogonal laser irradiation. Desorbed ions are drawn into the ion guide by a combination of a smooth gas flow and a segmented electric field (not shown).


Figure 2.5: Optical microscopy images of the burn mark on a grid sample for evaluating the spatial resolution of the imaging setup. The space between two laser beam damaged tracks is 20 μm. The width of the damaged track is less than half of the space between two damaged tracks. The spatial resolution of this imaging setup is better than 10 μm.

Figure 2.6: Optical microscopy and MALDI images of a fine grid for evaluating the spatial resolution of the imaging setup. The grid is 500 lpi, about 10 μm thickness and 50 μm spacing. The pixel is 5 μm $\times$ 5 μm. The spatial resolution is better than 10 μm.

The MALDI imaging process is just analogous to that of digital imaging in photography where each image is composed of an ordered array of thousands of pixels and each pixel is composed of individual color channels. However, the images from MALDI imaging experiments are assembled from an ordered array of mass spectra taken across the sample. So in order to construct the MALDI images, we have to know the coordinates of each pixel and the corresponding mass spectra. In this experiment, MALDI images were constructed using a custom software and hardware. The target motion is controlled by a pre-programmed, multi-axis, stepper-motor controller. It is rastered in one dimension at a fixed velocity of about 250 μm/s, followed by a small step (10μm) corresponding to the laser spot size in the orthogonal direction. The start of each new raster line produces a timing pulse (time marker) that is recorded by the time-to-digital converter (TDC) in a dedicated channel for later synchronization. Fig.2.7 shows the block diagram of the procedure of recording the mass spectrum and the time marker during recording the mass spectrum. The idea of recording the time marker is as follows: When the step motor starts a new scan along the horizontal axis, the motor controller will produce a TTL pulse. This pulse is first fed into a delay generator to generate pulse with 1 ms pulse width. Then it is input into a Linear gate module as a gate signal. Meanwhile, the synchronized start signals (3 kHz, i.e. $\sim$330 μs pulse width) from the TDC are also fed into the same linear gate module with a certain delay ($\sim$50 μs) as an input signal. So the output from the linear Gate will have only three pulses within the 1 ms gate pulse width. The output of the linear gate module will be recorded through one of the TDC channels and embedded in the mass spectrum. The position on the target correlates with elapsed experiment time. The data acquisition system records all the time-of-flight events for an experiment
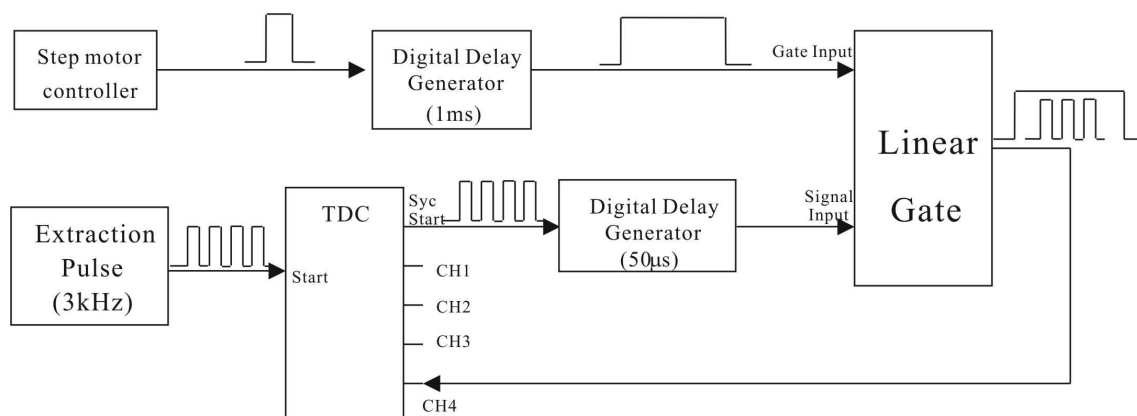
Figure 2.7: Schematic diagram of time marker recording system in MALDI imaging experiment. When there is a new scan along the horizontal axis, the signal generated from the step motor will be processed and recorded in the mass spectrum through TDC.

in a memory-spooled file (typically hundreds of megabytes in size). Spools were analyzed off-line to reconstruct mass-dependent images, or mass spectra from selected areas on the target. The 3-peaks signature is recognized by the analysis software during imaging generation.

Fluorescence microscopy

Fluorescence microscopy was used to study incorporation of dye-labeled proteins in some MALDI crystals for comparison. The analytes were labeled with two different fluorescent dyes: FITC (Fluorescein isothiocyanate isomer I, Sigma-Aldrich, ON, Canada) excited at 488 nm and TRITC (Tetramethylrhodamine isothiocyanate isomer R, Sigma-Aldrich, ON, Canada) excited at 561 nm. Simple fluorescent images were obtained with an Olympus BX60 confocal optical microscope (Olympus America Inc. Center Valley, PA, USA), using an UplanF1 lens($20\times$, N.A.= 0.5). Confocal scanning laser fluorescence images were obtained with Zeiss LSM710 microscope (Carl Zeiss Canada Ltd, 45 Valleybrook Dr. Toronto, Canada) with the $10 times$ magnification lens (N.A.=0.5).

2.2.2 Sample preparation

MALDI sample preparations

The matrices, 2,5-dihydrobenzonic acid (DHB), trans-3,5- dimethoxy- 4-hydroxy- cinnamic acid (sinapinic acid, SA), 4-hydroxy-α-cyanocinnamic acid (α-HCCA), were purchased from the Sigma-Aldrich Company (ON, Canada) and were used as supplied commercially without further purification. The peptide and protein analytes are listed in Table 2.1. All peptide and protein samples were obtained from Sigma-Aldrich Company (Ontario, Canada), except enkephalin, which was obtained from the American Peptide Company (Sunnyvale, CA, USA). The hydrophobicity of these analytes is calculated according to the B&B index (representing the hydrophobicity scale of the amino acid residues) [40].

Table 2.1: List of proteins and peptides used in this experiment.

Name & Amino acid sequence	MW (Da)	B&B index [40]
Enkephalin (YAGFLR)	726	-2490 (hydrophobic)
Substance p (RPKPQQFFGLM)	1347	-1790 (hydrophobic)
Bacitracin (ICLEIKNDHFI) [41]	1422	-4000 (hydrophobic)
Melittin (GIGAVLKVLTTGL PALISWIKRKRQQ)	2845	-4470 (hydrophobic)
Horse heart cytochrome c Sequence [42]	12,327	7350(hydrophilic)
Bovine pancreas trypsin inhibitor Sequence [42]	23,460	5780 (hydrophilic)
Bovine serum albumin Sequence [42]	66,430	-22,220 (hydrophobic)

Samples were prepared using dried-droplet [1], thin-layer [7], crushed crystal [8], and single larger crystal preparation methods [10, 43].

• **Dried-droplet preparation**

In the dried-droplet method, 2,5-DHB was dissolved at a concentration of 100 mg/mL in a mixture of acetonitrile/water (1:1, v/v) and 0.1% trifluoroacetic acid (TFA). Sinapinic acid matrix was dissolved in the solution at a concentration of 20 mg/mL with the same solvent. α-CHCA matrix was prepared to a saturated solution using the same solvent. All analytes were dissolved in bi-distilled water with a concentration of 10 pmol/μL. A 1.0 μL aliquot of the premixed solution of matrix and analyte was dropped on the stainless steel target and air-dried.

- **Thin layer preparation**

For the thin layer preparation, 2,5-DHB matrix was dissolved in ultrapure acetone at a concentration of 100 mg/mL. A 1.0 μL aliquot of this solution was applied on the target. A thin microcrystalline layer of matrix formed after fast evaporation of the solvent. A 1 μL of the analyte solution was applied onto the thin matrix layer.

- **Crushed crystal preparation**

To prepare crushed crystal samples, the same 2,5-DHB solution as prepared in dried-droplet method was used. A 1.0 μL aliquot of this matrix solution was first spotted on a target. After it crystallized, it was crushed as described in [8], and then the analyte solution was applied on top of the crushed matrix layer. For all the above three methods, the final molar analyte-to-matrix ratio was kept at $\sim 2 \times 10^{-5}$ as typically used in MALDI [43].

- **Single crystal**

To grow larger crystals [10, 43], 2,5-DHB and sinapinic acid matrices were prepared at concentrations of 100 mg/mL and 20 mg/mL, respectively, with the same solution as used in the dried-droplet method. Matrix solutions were mixed with analyte solution at a final molar analyte-to-matrix ratio of $\sim 2 \times 10^{-5}$. The mixed solutions were swirled in a vortex

mixer and centrifuged. The supernatant solutions were taken and divided into vials. These vials were then warmed up to $\sim 45°C$ in a water bath for about 30 minutes and then allowed to cool to the room temperature. The vials were then taken out and put in the refrigerator ($4°C$) with the vial lid open for about two days in a dark place. Normally the single large crystals as large as $1 \times 0.6 \times 0.4$ mm^3 (2,5-DHB) and $1 \times 0.3 \times 0.2$mm^2 (SA) were obtained. The crystals were washed in the bi-distilled water to remove the mother solution coated on the surface of the crystal. The single crystals could be fixed to the stainless steel target with a drop of bi-distilled water.

Fluorescent labeling of proteins

To label the analyte proteins, the protein solutions were exchanged into borate buffer (pH 8.5,50 mmol/L) by dialysis for about 2 hours using a 500 Da molecular mass cutoff (MMCO) membrane in a beaker containing 2 L of the borate buffer, which was placed on a stir plate. The amounts of FITC and TRITC for each labeling reaction were determined depending on the amounts of samples to be labeled. In this experiment, we used a 24-fold molar excess of fluorescent dyes to the proteins for both fluorescent dyes. Both dyes were dissolved in DMSO (Dimethyl Sulfoxide). The concentration of each protein was 10 pmol/μL. The concentrations of both FITC and TRITC are 10mg/mL. Dialyzed proteins were transferred to a reaction tube and the appropriate amount of dyes was also transferred to the protein-containing reaction tube correspondingly; they were mixed and incubated at room temperature for one hour. The excess fluorescent dyes were removed by transferring the sample to a new 500 Da MMCO membrane; the samples were dialyzed in PBS (Phosphate Buffered Saline) for about one hour at room temperature. During the dialysis, the samples were stirred and covered with aluminum foil to protect the dyes from ambient light. Also the samples labeled with FITC and TRITC were dialyzed separately in different beakers to avoid cross-contamination. After the samples were labeled with fluorescent dyes, they were mixed with 2,5-DHB matrix solutions to grow the 2,5-DHB single large crystals following the procedure described above.

The acidic matrix solution used strongly quenches the signal from these dyes, particularly from FITC, making relatively long exposures (or high gains)necessary. Images of pure matrix crystals and crystals with only dye, but illuminated with the frequency of the other dye demonstrated that autofluorescence from the crystal, or other sources of stray light were at least an order of magnitude less intense than the desired fluorescence from the labeled proteins. Even so, in the fluorescence images of the large crystals (where confocal scanning was not used), autofluorescence and internal reflection may be responsible for some diminished contrast in the images.

2.3 Results and Discussion

In order to comprehensively study the analyte distribution, the common matrices such as 2,5-DHB, α-HCCA, and sinapinic acid with typical preparations were firstly studied. Then large single crystals of 2,5-DHB and sinapinic acid were grown to examine the incorporation of analytes within the crystals. Fluorescence microscopy was also used to examine the analyte distribution with dye-labeled proteins in single 2,5-DHB crystals. Some effects of laser ablation were studied, which might be related to the morphology change of the matrix crystal surface due to laser ablation.

### 2.3.1 Analyte distribution in standard MALDI samples

The empirical distributions of MALDI crystals and analyte signal from different types of sample preparation in MALDI are quite well known, and have been previously mapped at modest resolution by imaging MALDI [20]. In the dried droplet preparation with DHB, larger crystals tend to form on the periphery of the spot, and the signal tends to be concentrated there in so-called hot spots. For sinapinic acid or α-HCCA, the crystals tend to be smaller and more uniformly distributed over the sample spot. The crushed-crystal and thin film methods of preparation both result in smaller average crystal sizes for all the matrices, and consequently a more uniform distribution of signal over the sample. In this

section, we examine these common sample preparation techniques at better than 10-μm resolution with different analyte species, mainly to demonstrate the imaging method.

Fig.2.8 shows the mass spectra of melittin or insulin from 2,5-DHB, α-HCCA, and sinapinic acid matrices using the dried droplet preparation and the corresponding images for the targets. Red represents the distribution of analyte molecules and green represents the background chemical noise as indicated, where no significant peaks are present. As expected, the three matrices give very different sample morphologies corresponding presumably to the way the crystals form during air drying, and are consistent with the description given above.

Fig.2.8a shows the results for the 2,5-DHB sample. The macrocrystals are typically about 500 μm in the longest dimension, but less than 100 μm in the other dimensions. It is clear that the analyte molecules (red color) are found mostly around the edge of the sample and located on the macrocrystals of the DHB matrix, consistent with observations of hot spots on the edge of dried droplet preparations. The results suggest incorporation of the analyte into the crystals. A zoomed image of some DHB macrocrystals is shown in the red inset. Although the analyte distribution over the whole sample (Fig.2.8a) is highly non-uniform, the inset suggests that the distribution within the crystals is relatively uniform, consistent with the recent mass spectral images of dried dried droplet samples reported by Bouschen and Spengler [33], but in contrast to some observations of sweet spots even within crystals. Our spatial resolution is quite coarse, however, with even the largest faces of the crystals only a few pixels in width, so it is difficult to draw definite conclusions about uniformity in these small crystals. The other faces are smaller still, and in general not exposed to the laser in dried droplet samples.

For comparison, we have also examined dried droplet preparations of bacitracin labeled with FITC in 2,5-DHB using confocal fluorescence microscopy. The image shown in the greed inset in Fig.2.8a seems reasonably consistent with the MALDI results, considering the much inferior spatial resolution and dynamic range of the MALDI image. The confocal image does show some non-uniformity, but the distribution is considerably more uniform
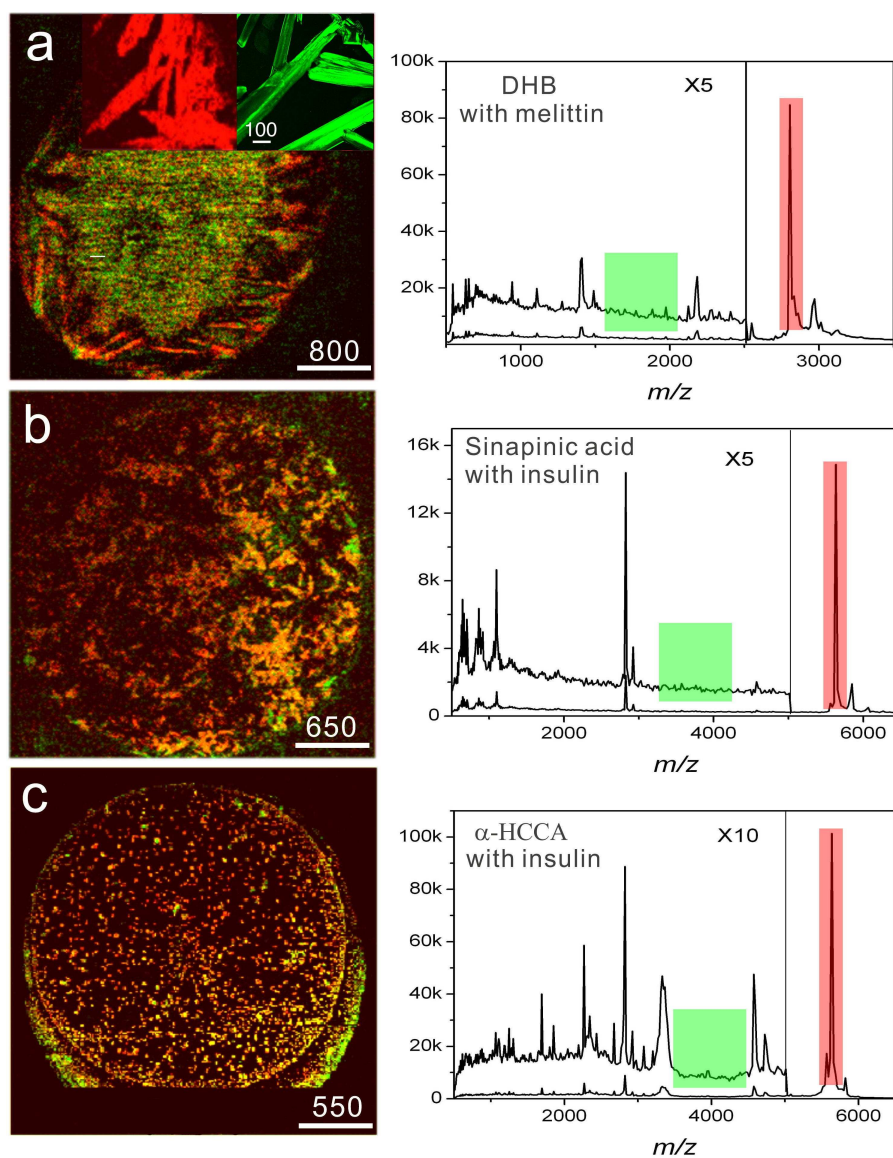
Figure 2.8: MALDI images of analyte distributions with dried-droplet sample preparation for different matrices and the corresponding integrated mass spectra. Red represents the distribution of analyte molecules and green represents the background chemical noise as indicated in the mass spectra. In panel(a), the inset in red is an expansion of the MALDI image showing crystals near the periphery of the target. The inset in green is a confocal scanning fluorescence image of bacitracin labeled with FITC in a dried droplet 2,5-DHB crystal, shownn here for comparison. The indicated scale is in μm.

than observed by Dai*et al.* using similar methods [15]. This may indicate that the incorporation of analyte in rapidly drying crystals is highly variable, and dependent on particular sample preparation conditions.

Fig.2.8b shows relatively small crystals formed from sinapinic acid matrix. The matrix crystals are much smaller than those of the DHB matrix, typically less than 50 μm. The analyte molecules are relatively uniformly distributed around the whole sample, and higher signal reproducibility was obtained from sinapinic matrix than that of the DHB matrix. Fig.2.8c shows the α-HCCA sample. The matrix crystal size is much smaller that the above two, typically less than 10 μm. The analyte molecules are more homogeneously distributed, giving the best signal reproducibility from spot to spot.

Fig.2.8 also shows the distribution of chemical noise for the three dried droplet preparations. In the case of 2,5-DHB, the chemical noise is distributed more uniformly throughout the sample suggesting their exclusion from the larger crystals, consistent with the high tolerance to impurities observed in MALDI [8, 44, 45]. It is not possible to examine the distribution of sodium in the sample directly in our instrument because of the low mass cutoff of the quadrupole ion guides, but Fig.2.9 shows the distribution of the sodium adducts, which is presumably correlated to the sodium distribution. The exclusion of sodium is striking in Fig.2.9a, where no signal from the sodium adducts is observed in the large peripheral crystals, consistent with measurements in ref. [33]. In Figs.2.8b & c, there is some evidence of segregation of the noise signal from the analyte signal in sinapinic acid and α-HCCA targets, with the noise more dominant at the edges of the dried droplet, in contrast to the DHB sample. Again, the distribution of the sodium adducts in the α-HCCA target shown in Fig.2.9b has the same characteristic. The exclusion from the much smaller crystals is much less obvious in this case compared to DHB, but the increased Na signal at the periphery is quite clear.

The segregation of the noise signal to the sample periphery is much more pronounced in the more complex sample shown in Fig.2.10, where two crude cell lysates from the K562 human arithro leukemia cell line were mixed with α-HCCA solution and deposited
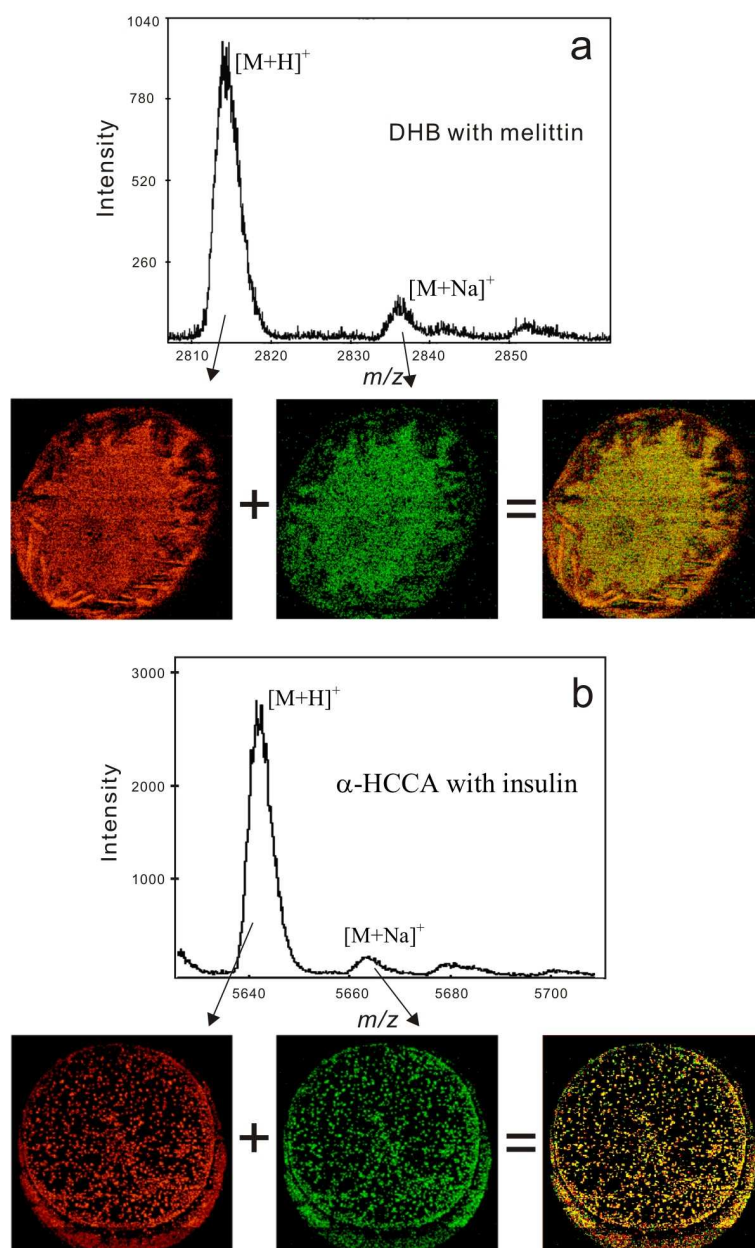
Figure 2.9: Distributions of the protonated and sodiated molecular ions in dried droplet preparations of (a) DHB with melittin (b) α-HCCA with insulin, and the corresponding mass spectra.

directly on the target without purification. Here the noise is much more pronounced at the edges, and a spectrum taken from the edge shows almost no analyte signal at all.

The observed segregation of the noise signal from the analyte signal may indicate that there is a relatively lower affinity of sodium ions with the matrix molecules compared to the protein ions. Therefore the sodium ions may still remain in the solvent solution during the matrix crystallization process instead of incorporating into the matrix crystal as the protein ions. This seems consistent with the distribution of noise signal mostly from the center or between 2,5-DHB matrix crystals shown in Fig.2.8a, and around the edge of the sample shown in Fig.2.9b and Fig.2.10. However, the absence of analyte signal in noisy regions does not necessary indicate the absence of analyte, since it is well known that salts or other impurities can suppress analyte signal in MALDI, and that signal can often be recovered by sample washing procedures. On the other hand, the absence of noise signal in the regions of strong analyte signal is strong evidence for the absence of impurities.

We also examined the analyte distributions in the thin layer [7] and crushed crystal [8] sample preparations. For sinapinic acid and α-HCCA, it is well-established that the resulting crystals are even smaller, and the signal distribution even more uniform, but the techniques are less commonly used with 2,5-DHB, which we examine here. As shown in Fig.2.11, it is clear that the crystals formed with both methods are smaller and produce a much more homogeneous analyte distribution. The crushed crystal method produces the smallest crystals, similar to those of the α-HCCA dried droplet in Fig.2.8c, while the thin layer produces intermediate size comparable to the sinapinic acid crystals formed from a dried droplet in Fig.2.8b.

In summary, the examination of different matrices and preparation methods using MALDI imaging gives a straightforward impression of the analyte distributions. The results show that smaller matrix crystals produced either from different matrices or different sample preparation methods mostly contribute to the uniformity of analyte distributions across the sample, resulting in better ion signal reproducibility from spot to spot. Experiments like this can be used to provide some guidance about how to choose the suitable matrix
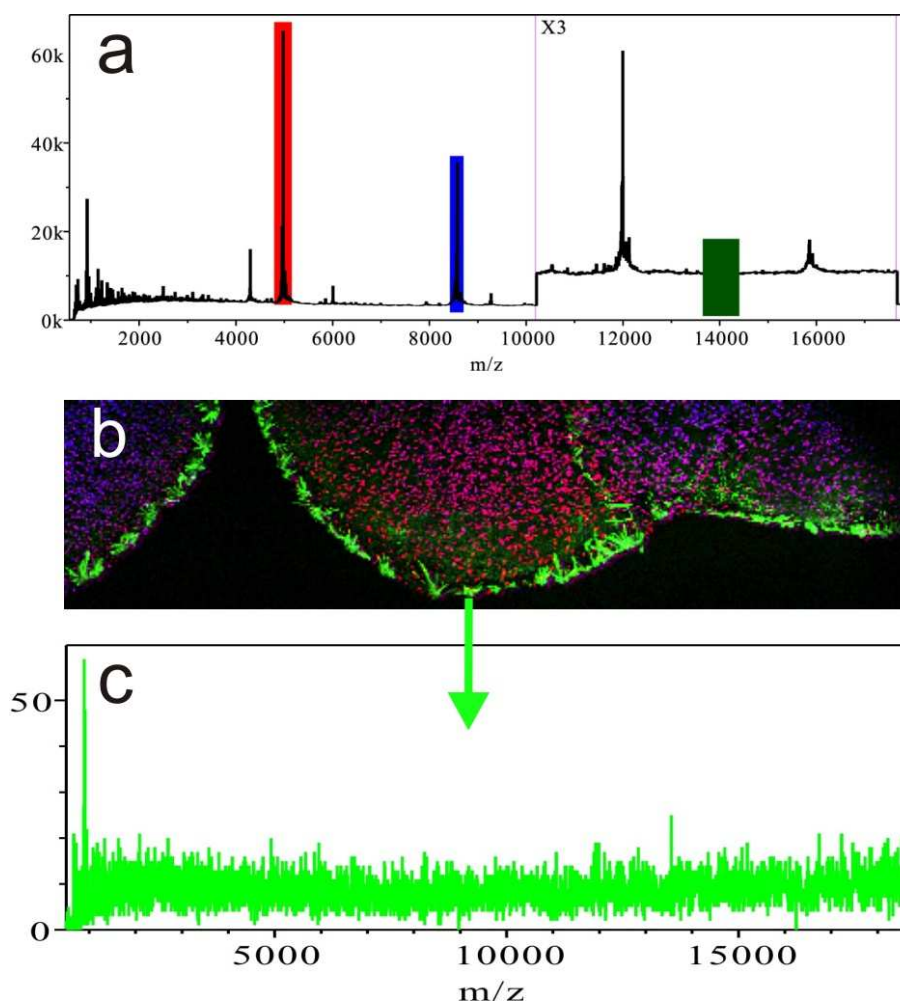
Figure 2.10: MALDI images and mass spectra of two cell mixtures prepared with the dried droplet method without purification. Clear segregation of chemical noise from the analyte signal is observed. (a) mass spectrum indicating imaged portions, (b) corresponding MALDI images, (c) mass spectrum generated from the edge of the sample.
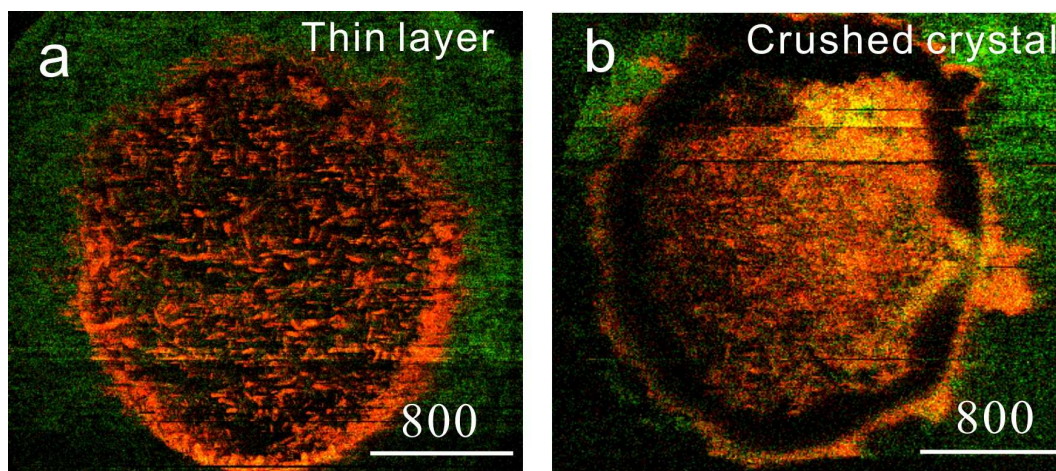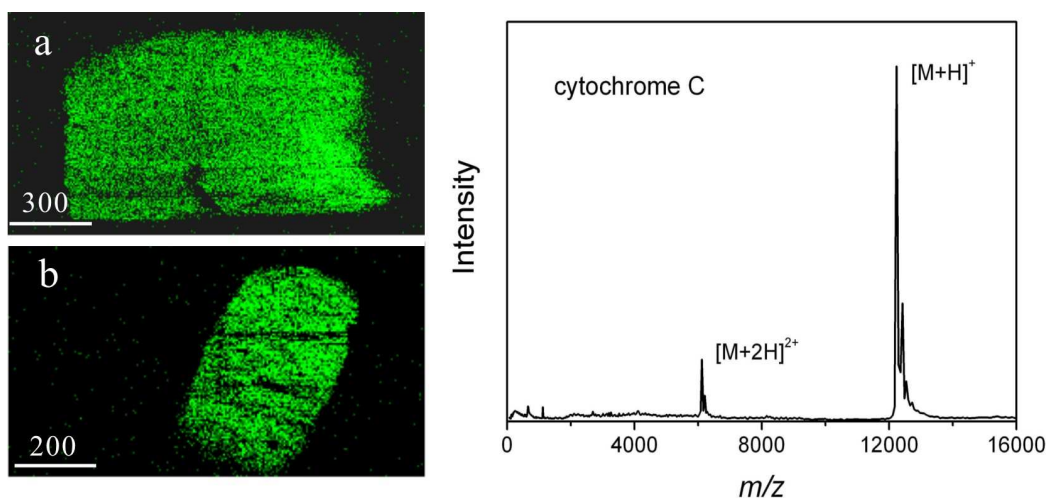
Figure 2.11: MALDI imaging of analyte distribution in 2,5-DHB matrix with different sample preparations. It is clear that thin layer and crushed crystal methods give a more homogeneous analyte distribution than that of dried droplet method. The analyte used is melittin. The indicated scale is in μm. (a) Thin layer preparation (b) Crushed crystal preparation.

and sample preparation methods for a particular application.

2.3.2 Distributions of purified analytes in single crystals

In the standard MALDI samples investigated above, the crystals are too small to determine the analyte distributions within the crystals by MALDI imaging. We have therefore grown single crystals of 2,5-DHB and sinapinic acid matrices to $\sim$ mm dimensions [43] with inclusion of cytochrome C as analyte.

The DHB crystals are mostly parallelepiped up to $1\times0.6\times0.4$ mm in size. We examined the largest face (100), believed to be the face most commonly exposed to the laser during MALDI [10], and the larger cross-section (010) from the same crystal. The distribution of cytochrome C in this crystal, shown in Figs.2.12 a & b, indicates homogeneous incorporation, which is also manifested by the low variation in the signal intensity from spot to spot when acquiring the mass spectrum. The small variations of the signal on the crystal face appear to be random or statistical in nature, whereas any influence of the crystal growth or crystal properties on incorporation might be expected to exhibit a pattern.
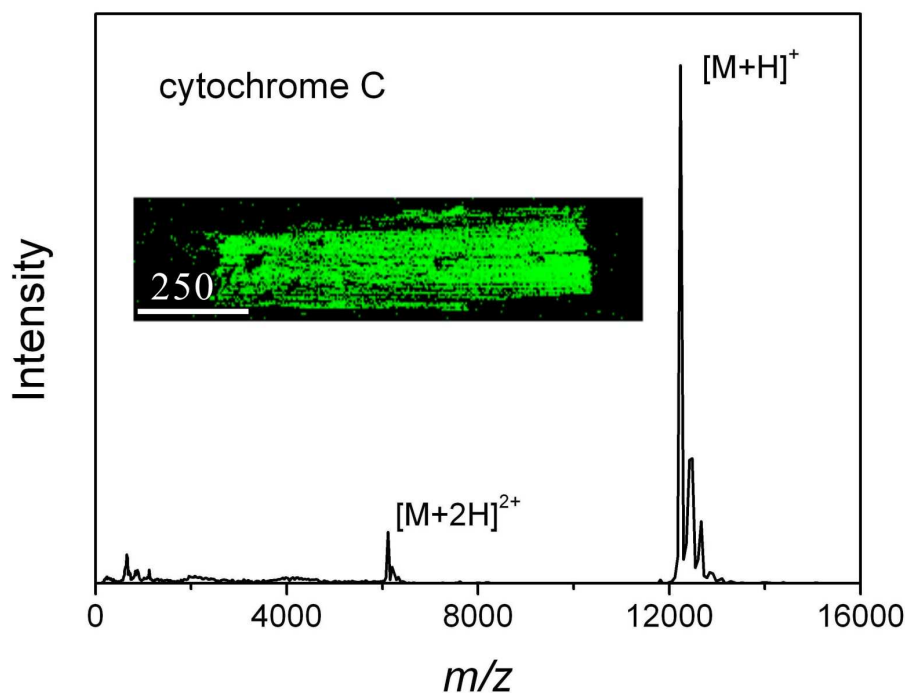
Figure 2.12: MALDI images of the distribution of cytochrome C on two faces of a single large DHB matrix crystal, and the corresponding integrated mass spectrum. Analyte molecules are homogeneously distributed on both (a) the largest face (100) and (b) the larger cross-section (010). The indicated scale is in μm.

Sinapinic acid forms long crystals along the [100] axis with a hexagonal cross-section $(10\bar{3})$ [46]; in our case about 1 mm long with a cross-section about 0.3 mm along a diagonal. The analyte distribution on the largest face of this crystal (010), shown in Fig.2.13, is again quite uniform, as with the 2,5-DHB crystal, consistent with the observation of a large sinapinic acid crystals by Dai *et al.* using confocal fluorescence microscopy [15].

In order to obtain crude depth profiles, all three crystal faces in Fig.2.12 and Fig.2.13, were scanned multiple times. Since each sample site is exposed to 40 laser shots, and the fluence with small spots is high compared to typical MALDI experiments [47], considerable material is removed during each scan. The laser was refocused between scans to optimize the signal, and from the distance the lenses were moved, the ablation depth is estimated to be a few tens of μm.

Fig.2.14 shows the first four scans. In each case, the intensity decreases, probably as a result of surface modification due to laser irradiation [46, 48], but the distributions remain quite homogeneous. This interpretation is consistent with a measurement of a cut crystal, which showed no difference in intensity from an uncut crystal. A small decrease in homogeneity is observed, but again, it appears to be random or statistical, and therefore is

Figure 2.13: MALDI images of the distribution of cytochrome C on the largest face (010) of sinapinic acid matrix crystal, and the corresponding integrated mass spectrum. The indicated scale is in μm. Analyte molecules are homogeneously distributed this face. No image was obtained from the cross-section ($10\bar{3}$) of sinapinic acid crystal due to its small dimension.

also likely to be associated with the lower signal intensity or uneven surface modification, and not inhomogeneous incorporation in the crystal.

The depth resolution in these profiles is rather coarse, and may obscure fine structure on the scale of 10 μm or less. However, the lateral images do not show structure on this scale on the faces examined. Moreover, experiments on the hysteresis effect in MALDI by Fournier *et al.* [46], in which a single spot on sinapinic acid crystal is examined repeatedly after much smaller irradiation cycles, also show a quite uniform distribution of signal as a function of radiation, and therefore of depth on a considerably finer scale.

To improve the generality of the above observations, we have also examined a much larger protein (BSA at $\sim$ 66 kDa) in 2,5-DHB. The results shown in Fig.2.15 again show a homogeneous inclusion of the analyte.
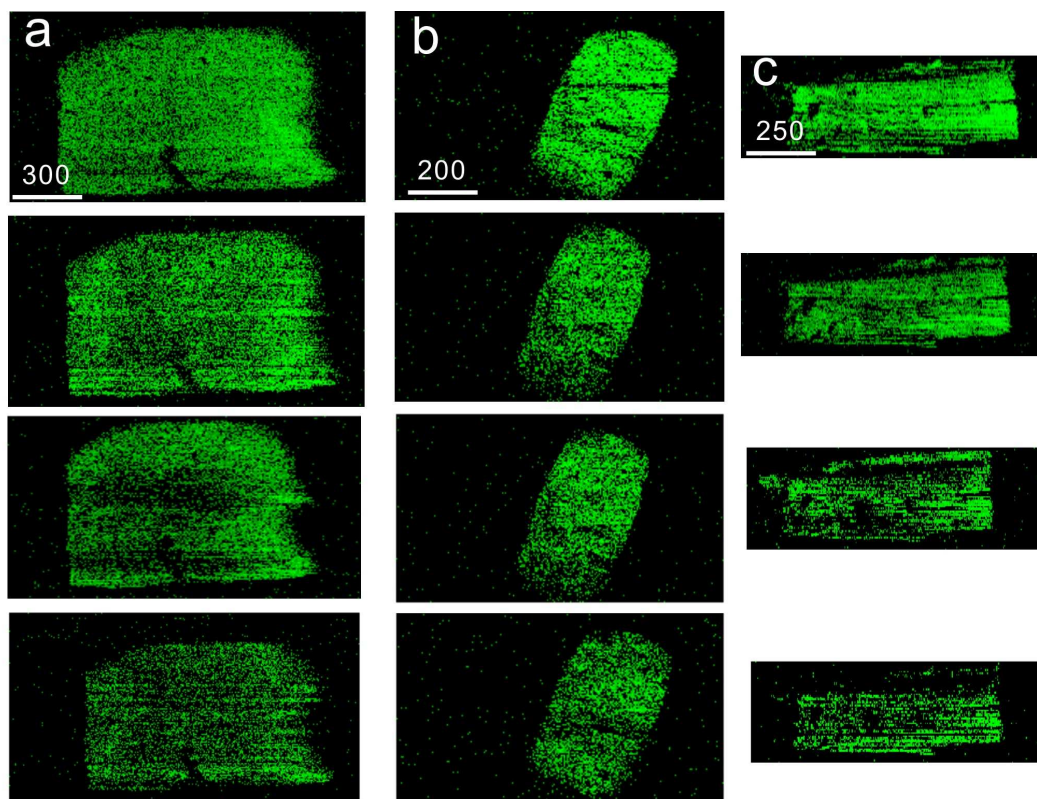
Figure 2.14: MALDI images of cytochrome C observed in consecutive scans of (a) the largest face (100) of 2,5-DHB single crystal, (b) larger cross-section face (010) of DHB single crystal, (c) largest face (010) of sinapinic acid single crystal. The consecutive scans provide a depth profile and demonstrate homogeneous incorporation. The variation of intensity is probably a result of surface modification due to laser irradiation (see text).

These results represent the first direct mass spectrometric measurement of the protein distribution within large single crystals of 2,5-DHB, and within crystals of sinapinic acid (of any size). They demonstrate clearly that purified protein analytes are distributed uniformly on the crystal surface, and also throughout the crystal. Although we were not able to examine the smaller faces of the crystals, such as the $(10\bar{3})$ face of sinapinic acid matrices, the depth profiles from repeated scans suggest that the distribution in other dimensions is also uniform.

Ejection dynamics are quite different for different MALDI matrices, and this has been correlated to different degrees of analyte incorporation [14, 49]. In particular, the initial velocities of analyte ions ejected from 2,5-DHB are considerably higher, and the ions
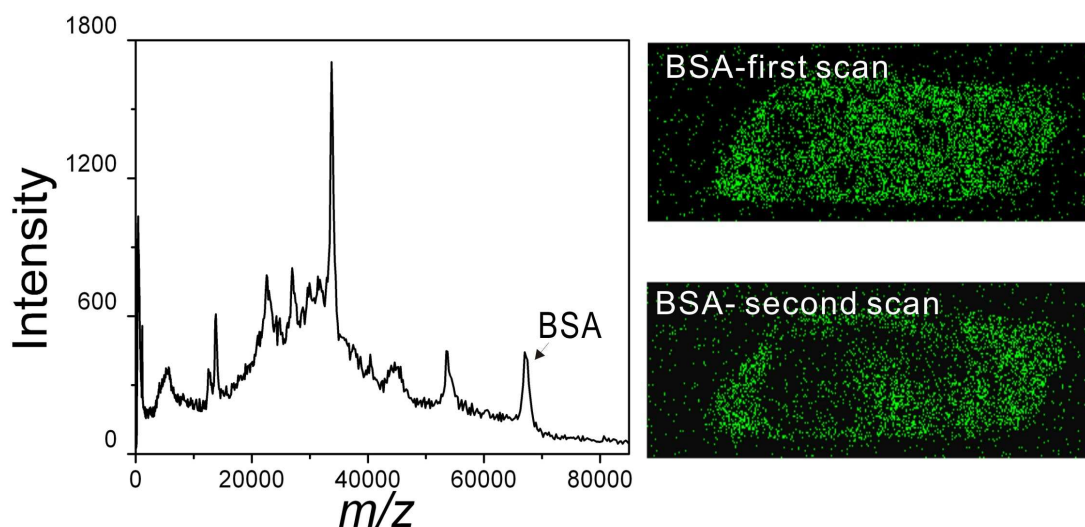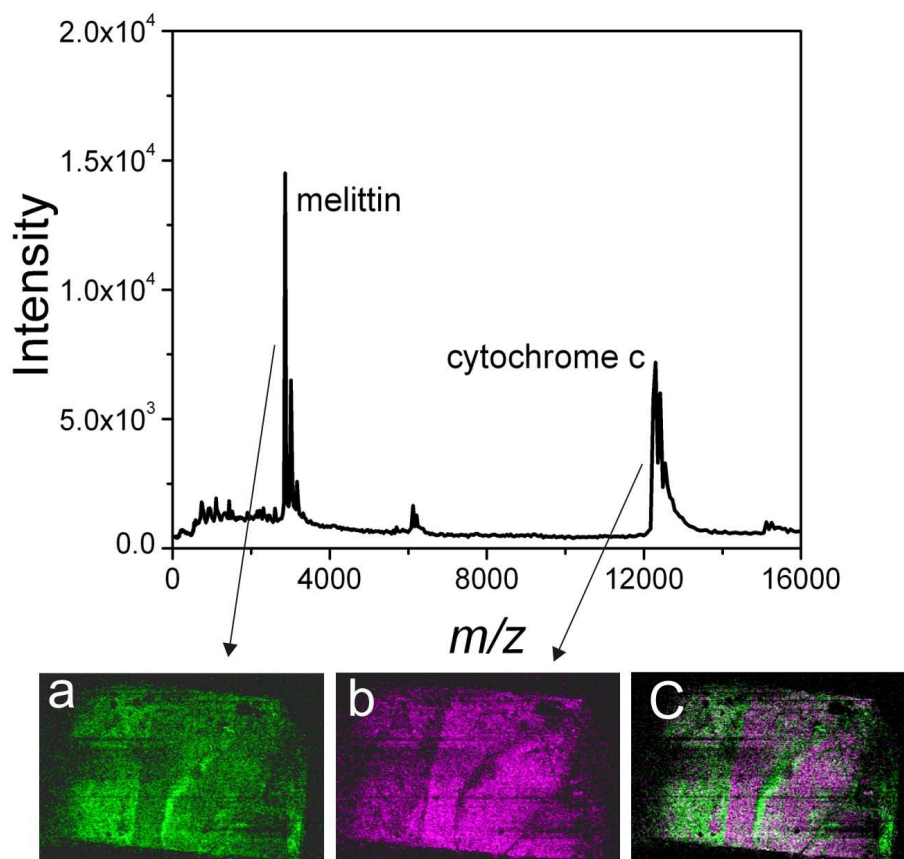
Figure 2.15: The analyte distributions of BSA in a 2,5-DHB single crystal, and the integrated mass spectrum. Two consecutive scans are shown.

more stable, than from 2,6-DHB, in which evidence suggests only surface adhesion of the analyte [14]. This led to speculation that other matrices with low initial analyte velocities like α-HCCA might also belong to a class of matrices which do not incorporate analytes. However, measurements using pH indicator molecular probes with redissolved crystals give evidence for incorporation of protein analytes in single crystals of α-HCCA [24]. Our results clearly show analyte incorporation in sinapinic acid, and the initial velocities of analyte ions from sinapinic acid are quite close to those ejected from α-HCCA and 2,6-DHB.

The results with DHB are consistent with the more indirect depth profiles and spectrophotometric measurements of redissolved crystals by Strupat *et al.* [10] and of the confocal microscope images of labeled proteins of Horneffer *et al.* [18]. In contrast to 2,5-DHB, the different faces of sinapinic acid have very different hydrophobicity [16], and incorporation of dye-labeled proteins has been reported to occur preferentially (or exclusively) on the hydrophobic face, resulting in an hourglass pattern of proteins on the (010) face. Our results show no evidence of preferential incorporation of pure proteins in sinapinic acid, consistent with the suggestion that the hourglass result may be an artifact from unbound dyes in the solution [22].

Figure 2.16: MALDI images of the analyte distributions of (a) melittin and (b) cytochrome C in a DHB single crystal, and the integrated mass spectrum. The composite image is shown in (c).

2.3.3 Distribution of multiple analytes in single crystals

Although purified protein analytes appear to be homogeneously distributed within single large matrix crystals, we have observed segregation between some analytes when the matrix crystal is doped with a mixture [31]. For example, Fig.2.16 shows the analyte distributions of melittin and cytochrome C. It is obvious that both of them are not homogeneously distributed in the single large crystal, but seem to segregate from each other.

Bouschen and Spengler have also observed segregation within crystals formed in the dried droplet preparation, and they have suggested some dependences of the effect on hydrophobicity, isoelectric point, analyte mass, and polarity [33]. We have not done systematic
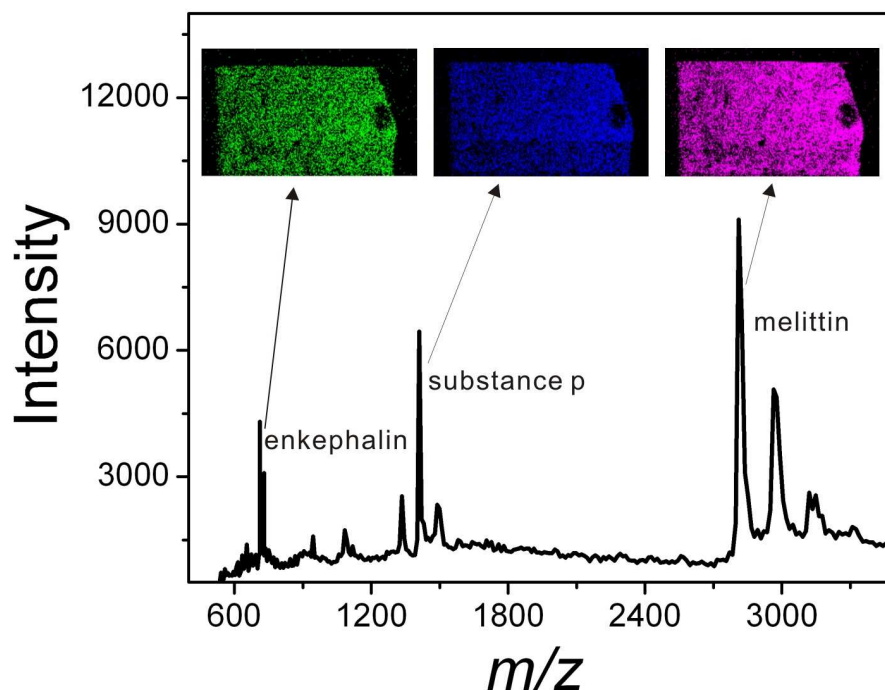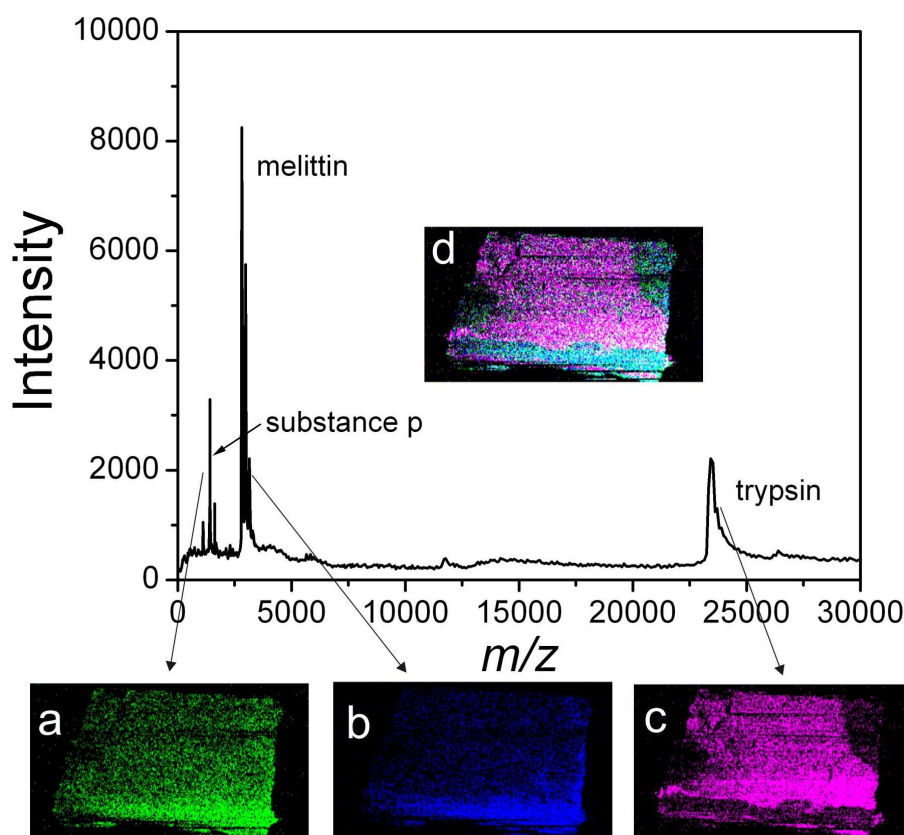
Figure 2.17: The analyte distributions of enkephalin, substance-p, and melittin in a single 2,5-DHB crystal. The three analytes have similar hydrophobicity, and no significant analyte segregation is observed.

measurements to quantify such dependences, but our results do show a strong correlation between segregation and hydrophobicity. The analytes shown in Fig.2.16 have very different hydrophobicity with melittin being hydrophobic and cytochrome C hydrophilic (see Table 2.1). Two three-component mixtures are shown in Fig.2.17 and Fig.2.18. In Fig.2.17, all three components have similar hydrophobicity, and no segregation is observed. In Fig.2.18, two components have are similarly hydrophobic, while the third is strongly hydrophilic and appears segregated from the first two.

The absence of segregation of substance P and melittin in Fig.2.17 and Fig.2.18 is in contrast to the results of ref. [33] for the same peptides in dried droplet crystals. The difference here may be related to the much more rapid formation of the crystals in a drying droplet, or the continuous diffusion of an equilibrium solution during the growing of a large crystal.

The mass difference between the analytes, and the resulting difference in mobility may

Figure 2.18: The analyte distributions of (a) substance P, (b) melittin, and (c) trypsin in a single DHB crystal. The two analytes with similar hydrophobicity (a,b) are segrated from the third (c), which has opposite hydrophobicity. The composite image is shown in (d).

also play a role in the segregation phenomenon, which is observed in Fig.2.16 and Fig.2.18 where the mass difference (and ratio) is significant. However, this correlation seems less compelling than the hydrophobicity correlation in our results. In Fig.2.17, the mass ratio between enkephalin and melittin is close to that of melittin and cytochrome C (Fig.2.16), but no obvious segregation is observed. Moreover, in Fig.2.19, the mass difference between cytochrome C and trypsin is similar to that between melittin and cytochrome C and again, no segregation is observed.
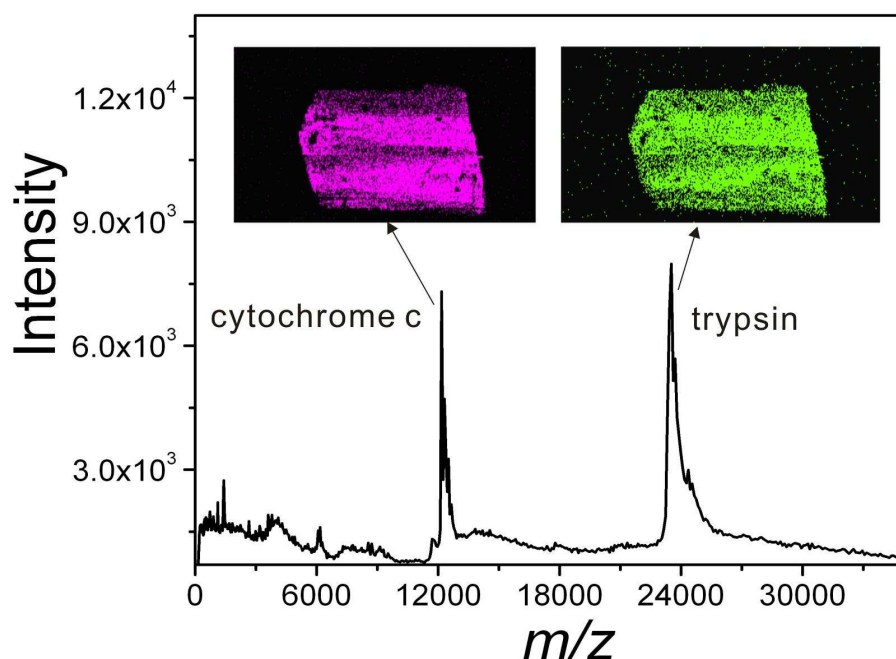
Figure 2.19: Analyte distributions of cytochrome C and trypsin in a single DHB crystal. Although the distributions are not perfectly homogeneous, no segregation is observed.

2.3.4 Fluorescence microscopy of a single crystal

In order to verify the observations of analytes distribution in MALDI imaging and to reduce the possibility of ionization artifacts in MALDI that might produce these kinds of results, we have also used fluorescence microscopy to examine single large crystals doped with same dye-labeled analytes. In this experiment, the fluorescence labeling process must be exactly followed regarding the ratio of dye and analyte, the pH value, and the removal of excess dyes. We examined the analyte distribution with both dried-droplet and single large crystal sample preparations.

Fig.2.20 shows simple fluorescence microscopy images of dried-droplet and single large crystals of 2,5-DHB matrix. The analyte is substance P labeled with FITC (green). Fig.2.20A shows the analyte distribution with dried-droplet preparation. It is clear that the analyte molecules are exclusively incorporated into the macrocrystals of the 2,5-DHB matrix. The analyte molecules distribute uniformly along these crystals, consistent with
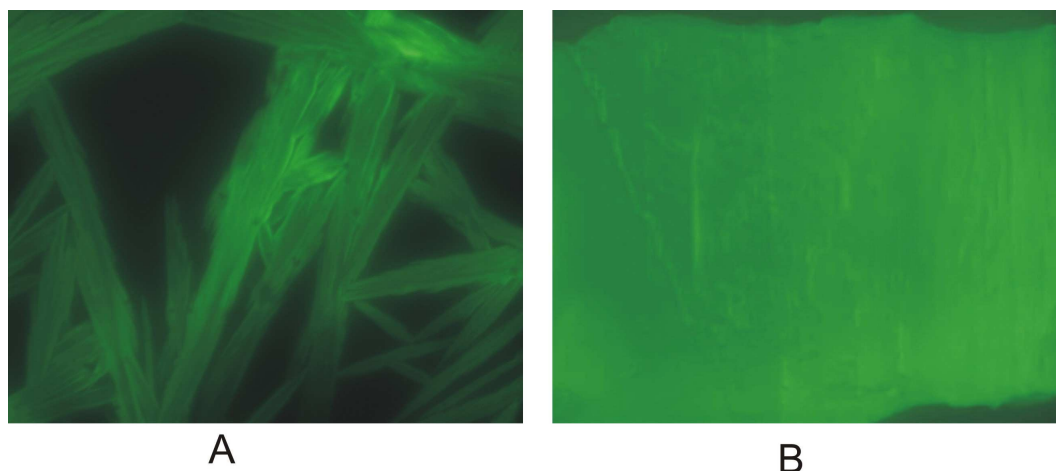
Figure 2.20: Fluorescence microscopy images of substance P labeled with FITC in 2,5-DHB crystals with A) dried droplet preparation and B) single large crystal preparation. The analyte molecules are uniformly distributed on both the macrocrystals and the single large crystal of the 2,5-DHB matrix.

the MALDI images. Fig.2.20B shows a single large crystal of 2,5-DHB matrix. This image clearly shows that the analyte molecules are very uniformly distributed, which is consistent with the MALDI images of 2,5-DHB doped with purified analytes shown in Fig.2.12.

The analyte segregations in single large 2,5-DHB crystals were also examined. Fig.2.21 shows simple fluorescence images of (a)melittin labeled with TRITC(red), (b)cytochrome C labeled with FITC (green), and (c) the superposed image of these two analytes. the contrast in this image is probably degraded by autofluorescence and internal reflection, but the pattern clearly shows segregation, consistent with the MALDI images of unlabeled proteins shown in Fig.2.16. Better images of small crystals formed in dried droplet samples (fast drying), obtained using confocal laser scanning microscopy, are shown in Fig.2.21 (d-e), and also show segregation of the analytes.

The mechanism of segregation is not understood, and is probably affected by many parameters including the concentration ratio of analyte solution, the pH value, and the temperature of the matrix solution in addition to the intrinsic properties of the analytes mentioned above. It is clear however that better reproducibility in MALDI (and subse-
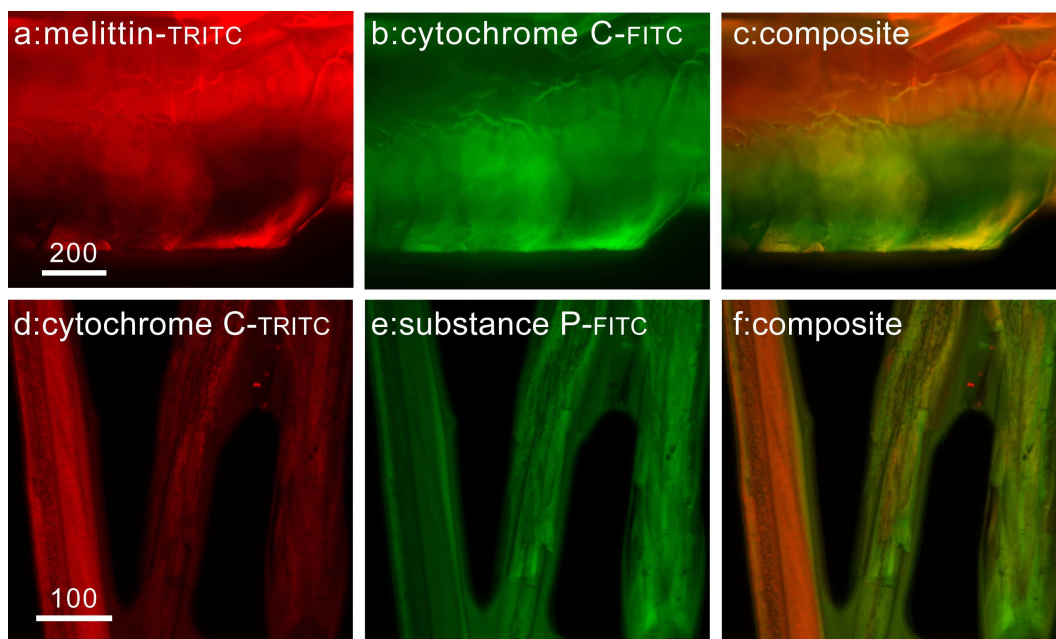
Figure 2.21: Fluorescence images of (a) melittin-TRITC, and (b) cytochrome C-FITC in a single large 2,5-DHB crystal, with the composite image in (c); and confocal scanning images of (d) cytochrome C-TRITC, and (e) substance P-FITC in crystals of 2,5-DHB formed in a dried droplet preparation, with the composite image in (f). Analyte segregation is clearly observed for the slowly grown single crystal using the same analytes as in Fig.2.16, and for smaller crystals formed in a dried droplet preparation.

quently better quantification) depends on gaining more control over the segregation and incorporation phenomena. Imaging experiments such as those studies here can play an important role in this type of investigation.

2.3.5 Ion signal variation versus laser scans

As is observed in the depth profiling of analyte distribution in single crystals of 2,5-DHB and sinapinic acid, the analyte intensity decreases for the consecutive scans on the single crystal: could this result from a variation of analyte concentration between different layers of the crystal? In fact this speculation is ruled out by scanning the surfaces of two small crystals cut from a single crystal. This comparison showed that there was no significant difference between the two surfaces in terms of analyte intensity shown in Fig.2.22, so there must be some other reasons accounting for the variation of analyte intensity over
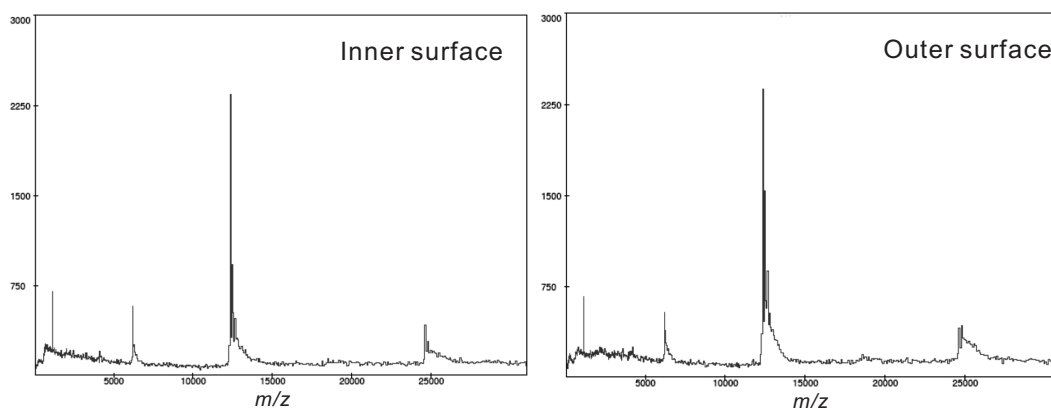
Figure 2.22: Examination of analyte intensity from the inner and outer surfaces of a single crystal by scanning two cut small crystals from the single one. No obvious difference in signal intensity is observed from inner and outer surfaces indicating a uniform analyte incorporation.

consecutive scans on the same crystal surface.

The variation of analyte intensity as a function of the laser scan times is shown in Fig.2.23; a gradual decay of the analyte intensity was observed. It was also found that an increase in laser energy would bring the analyte intensity back to some extent, but after that it decreased again. This variation of analyte intensity might be related to the morphology changes of crystal surface due to laser ablation, as reported previously [46]. When a laser beam irradiates the crystal surface continuously, crater morphology may be formed which can reflect and reduce the laser energy. An increased laser energy can remove the formed surface structure resulting in a fresh surface exposing to following laser irradiation. The ion signal intensity therefore increases. In Fig.2.23, the signal intensity after increasing the laser energy is still much lower than the first scan. This might be due to the fact that as the laser beam is now irradiating a crater or trough, ion emitted may have worse transmission.

2.3.6   Matrix adducts versus laser scans

Another interesting observation may be also related to the morphology change of the crystal surface, which is also consistent with the interpretation in the previous section.
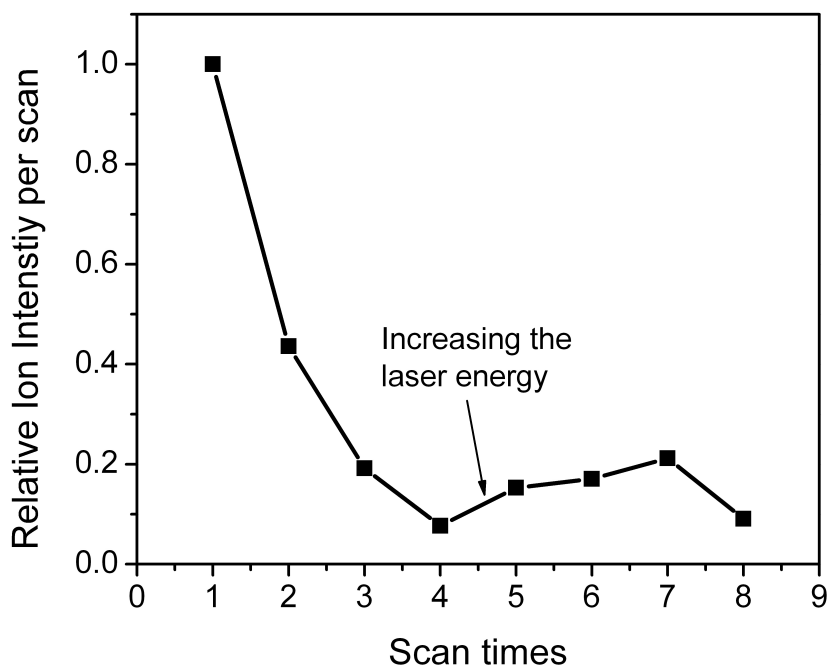
Figure 2.23: The analyte intensity variation as a function of the laser scan times. The ion signal decreases as the laser beam goes deeper in the single crystal. An increase in laser energy brings the ion signal back to some extent and it decreases again. This might be related to the morphology change of the crystal surface due to laser ablation.

We found that matrix cluster adducts of the molecular peaks increased with the increasing scan times on the 2,5-DHB single crystals shown in Fig.2.24A. However, this did not appear in single crystals of sinapinic acid under the same condition shown in Fig.2.25. This might be related to the different chemical reactions induced by the laser irradiation for these two matrices. However, it did not appeared in the dried-droplet preparation of 2,5-DHB matrix either. It is well known that the matrix cluster formation is related to the ion source pressure [50–52]. When the pressure in the ion source is elevated, the dense plume of matrix molecules will be cooled down resulting in the confinement of matrix molecules. This will give more exposure time for the analyte ions to interact with matrix molecules, and more matrix adducts will be formed. This was also verified by scanning a dried-droplet 2,5-DHB sample with varying the ion source pressure shown in

Fig.2.24B. Similar matrix cluster adduction was observed as the consecutive scans of 2,5-DHB single crystal. This may demonstrate that the increased matrix cluster of 2,5-DHB single crystal may result from the increase of local pressure when laser beam 'digs' deeper into the crystal. One can speculate that when the laser beam goes deeper by $\sim 50\mu m$ in each scan, this small region can produce a confinement of the dense plume of matrix and analyte ions. Then analyte ions will experience more collisions with the matrix molecules and form more matrix clusters.

This pressure-related matrix cluster adduction seems to give a reasonable explanation for what we have observed with the 2,5-DHB single crystals. The crystal sizes of the sinapinic acid single crystal and the macrocrystals in dried-droplet 2,5-DHB samples are much smaller compared to the 2,5-DHB single crystals. This may give some difference in the matrix cluster adduction probably because of the weaker confinement of ion plume. However, the burn mark of the laser beam is about 10 μm and the penetration depth is about 50 μm, i.e. even for the sinapinic acid single crystal and the macrocrystals in dried-droplet 2,5-DHB samples (~ 200 μm), enough ion plume confinement similar to the 2,5-DHB single crystals should have also been provided. So there might be some other factors affecting the matrix cluster adduction such as the difference in the shape of crater structure. Further study for this phenomenon is needed.

2.4 Conclusion

In this chapter, the high resolution MALDI imaging technique has been used to study the analyte distributions in the matrix crystal at different conditions. The results have provided more evidence that the analyte distribution is quite different for the normally used matrices with dried-droplet preparation, which may account for their difference in sensitivity and reproducibility from spot to spot. The direct evidence for exclusion of impurities in dried droplet samples was shown.

Purified proteins are incorporated uniformly throughout slowly-grown single crystals of
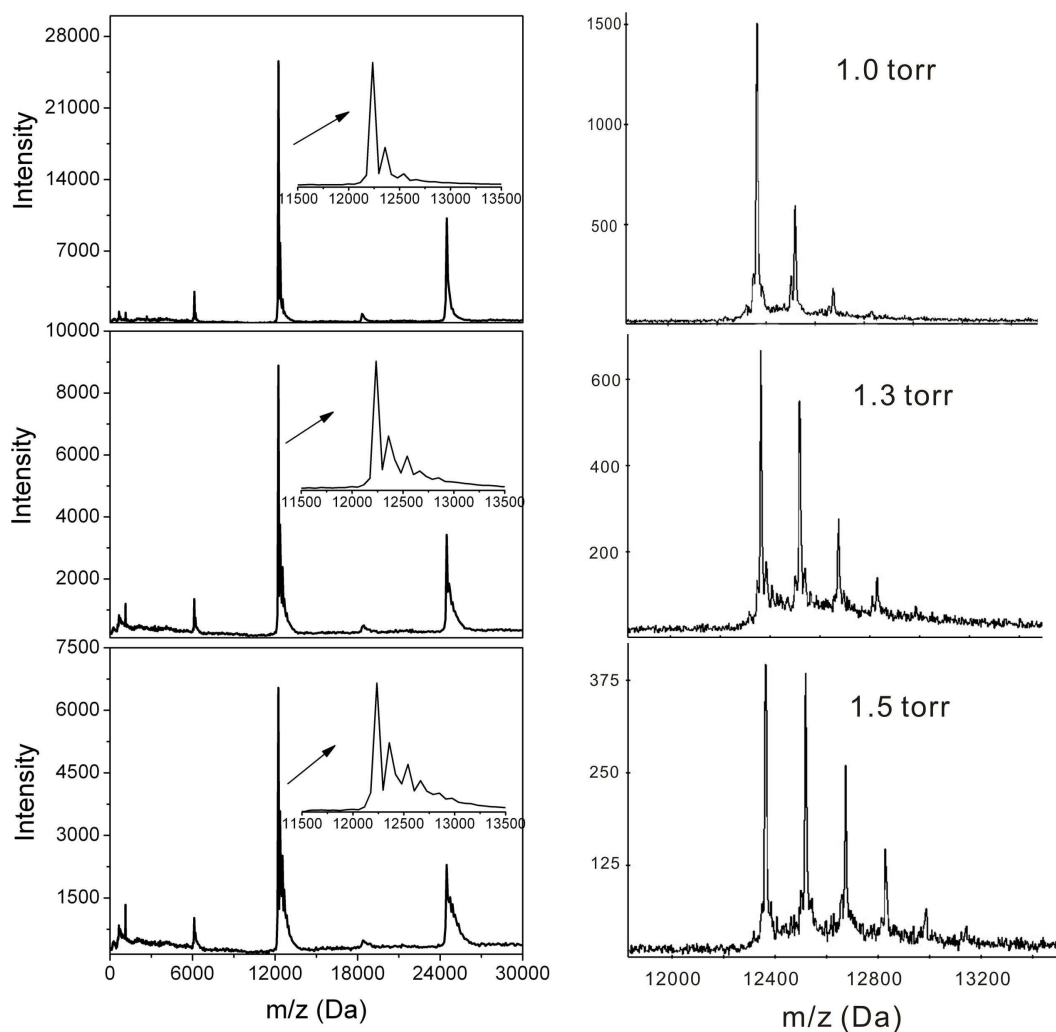
Figure 2.24: Studies on matrix cluster formation in DHB matrix. A) matrix clusters increase with consecutive laser scans on the DHB single crystal. B) matrix clusters increase with the increase of ion source pressure for the dried-droplet preparation of DHB matrix. Similar cluster adduction is found in both cases.
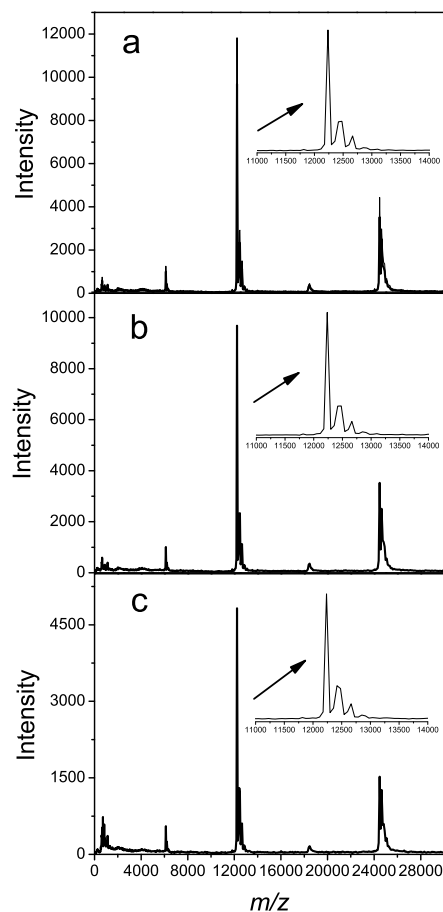
Figure 2.25: Study of matrix cluster adduction in sinapinic acid matrix. Matrix clusters don't increase with the consecutive laser scans on the sinapinic acid single crystal as observed in the 2,5-DHB single crystals.

2,5-DHB and sinapinic acid matrices, with no evidence for preferred crystal faces. In our preparation of dried droplet samples, the crystals formed by fast evaporation also show reasonably uniform distributions of purified protein analytes in the MALDI images, although higher resolution confocal scanning fluorescence images show some non-uniformity.

Mixtures of protein analytes incorporated in slowly grown 2,5-DHB crystals show analyte segregation, a phenomenon that appears to be correlated with analyte hydrophobicity.

A decrease of analyte signal intensity and an increase of matrix clusters are observed dur-

ing the consecutive scans of the laser beam on the crystal surface. These two phenomena might be related to a morphology change of the crystal surface due to laser irradiation.

References

[1] Karas, M.; Hillenkamp, F. *Anal. Chem.* **1988**, *60*, 2299–2301.

[2] Tanaka, K.; Waki, H.; Ido, Y.; Akita, S.; Yoshida, Y.; Yoshida, T. *Rapid. Commun. Mass Spectrom.* **1988**, *2*, 151.

[3] Hillenkamp, F.; Karas, M.; Beavis, R. C.; Chait, B. T. *Anal. Chem.* **1991**, *63*, 1193A–1203A.

[4] Beavis, R. C.; Chait, B. T. *Rapid Commu. Mass Spectrum.* **1989**, *3*, 432.

[5] Strupat, K.; Karas, M.; Hillenkamp, F. *Int. J. Mass Spectrom. Ion Processes* **1991**, *111*, 89–102.

[6] Beavis, R. C.; Chaudhary, T.; Chait, B. T. *Org. Mass Spectrom.* **1992**, *27*, 156.

[7] Vorm, O.; Mann, M. *J. Am. Soc. Mass Spectrom.* **1994**, *5*, 955–958.

[8] Xiang, F.; Beavis, R. C. *Rapid Commun. Mass Spectrom.* **1994**, *8*, 199–204.

[9] Krause, J.; Stoeckli, M.; Schlunegger, U. P. *Rapid Commun. Mass Spectrom.* **1996**, *10*, 1927.

[10] Strupat, K.; Kampmeier, J.; Horneffer, V. *Int. J. Mass Spectrom. Ion Processes* **1997**, *169/170*, 43–50.

[11] Gusev, A. I.; Wilkinson, W. R.; Proctor, A.; Hercules, D. M. *Anal, Chem.* **1995**, *67*, 1034–1041.

[12] Westman, A.; Huth-Fehre, T.; Demirev, P.; Sundqvist, B. U. R. *J. Mass Spectrom.* **1995**, *30*, 206–211.

[13] Hensel, R. R.; King, R. G.; Owens, K. G. *Rapid Commun. Mass Spectrom.* **1997**, *11*, 1785.

[14] Horneffer, V.; Reichelt, R.; Strupat, K. *Int. J. Mass Spectrom.* **2003**, *226*, 117–131.

[15] Dai, Y.; Whittal, R. M.; Li, L. *Anal. Chem.* **1996**, *68*, 2494–2500.

[16] Beavis, R. C.; Bridson; N., J. *J Phys. D: Appl. Phys.* **1993**, *26*, 442–447.

[17] Chan, T. W. D.; Colbrun, A. W.; Derrick, P. J.; Gardiner, D. J.; Bowden, M. *Org. Mass Spectrom.* **1992**, *27*, 188–194.

[18] Horneffer, V.; Forsmann, A.; Strupat, K.; Hillenkamp, F.; Kubitscheck, U. *Anal. Chem.* **2001**, *73*, 1016–1022.

[19] Spengler, B.; Hubert, M.; Kaufmann, R.; In *Proceedings of the 42nd ASMS Conference on Mass Spectrometry and Allied Topics*, May,1994.

[20] Garden, R. W.; Sweedler, J. V. *Anal. Chem.* **2000**, *72*, 30–36.

[21] Strupat, K.; Karas, M.; Hillenkamp, F.; In *Proceedings of the 12th International Mass Spectrometry Conference*, 1991.

[22] Mitchell, C. A.; Lovell, S.; Thomas, K.; Savickas, P.; Kahr, B. *Angew. Chem. Int. Ed. Engl.* **1996**, *35*, 1021.

[23] Gluckmann, M.; Pfenninger, A.; Kruger, R.; Thierolf, M.; Karas, M.; Horneffer, V.; Hillenkamp, F.; Strupat, K. *Int. J. Mass Spectrom.* **2001**, *210*, 121–132.

[24] Kruger, R.; Pfenninger, A.; Fournier, I.; Gluckmann, M.; Karas, M. *Anal. Chem.* **2001**, *73*, 5812–5821.

[25] Gusev, A. I.; Vasseur, O. J.; Proctor, A.; Sharkey, A. G.; Hercules, D. M. *Anal. Chem.* **1995**, *67*, 4565–4570.

[26] Figeys, D. *Anal. Chem.* **2003**, *75*, 2891–2905.

[27] Caprioli, R. M.; Farmer, T. B.; Gile, J. *Anal. Chem.* **1997**, *69*, 4751–4760.

[28] Stoeckli, M.; Farmer, T. B.; Caprioli, R. M. *J. Am. Soc. Mass Spectrom.* **1999**, *10*, 67–71.

[29] Piyadasa, G.; McNabb, J. R.; Spicer, V. L.; Standing, K. G.; Ens, W.; In *Proceedings of the 52nd ASMS conference on mass spectrometry and allied topics*, May, 2004.

[30] Ens, W.; Piyadasa, G.; Collado, V.; Krokhin, O.; Loboda, A.; McNabb, J. R.; Qiao, H.; Spicer, V. L.; Standing, K. G.; In *Proceedings of the 53rd ASMS conference on Mass Spectrometry and Allied Topics*, May,2005.

[31] Qiao, H.; Piyadasa, G.; Krokhin, O.; Spicer, V.; Standing, K. G.; Ens, W.; In *Proceedings of the 54th ASMS Conference on Mass Spectrometry and Allied Topics*, May, 2006.

[32] Spengler, B.; Hubert, M. *J. Am. Soc. Mass Spectrom.* **2002**, *13*, 735–748.

[33] Bouschen, W.; Spengler, B. *Int. J. Mass Spectrom.* **2007**, *266*, 129–137.

[34] Kozlovski, V. I.; Loboda, A. V.; Spicer, V.; McNabb, J. R.; Ens, W.; Standing, K. G.; In *Proceedings of the 50th ASMS conference on mass spectrometry and allied topics*, 2002.

[35] Krutchinsky, A. N.; Chernushevich, I. V.; Spicer, V. L.; Ens, W.; Standing, K. G. *J. Am. Soc. Mass Spectrom.* **1998**, *9*, 569–579.

[36] Chernushevich, I. V.; Ens, W.; Standing, K. G. *Anal. Chem.* **1999**, *71*, 452A–461A.

[37] Schriver, K.; Chaurand, P.; Caprioli, R. M.; In *Proceedings of the 51st ASMS conference on Mass Spectrometry and Allied Topics*, 2003.

[38] Chaurand, P.; Schwartz, S. A.; Billheime, D.; Xu, B. J.; Crecelius, A.; Caprioli, R. M. *Anal. Chem.* **2004**, *76*, 1145–1155.

[39] Hsieh, Y.; Reyzer, M. L.; Caprioli, R. M.; Zhao, J. Y.; Yang, M.; Ng, K.; Korfmacher, W.; In *Proceedings of the 51st ASMS conference on mass spectrometry and allied topics*, May, 2003.

[40] Bull, H. B.; Breese, K. *Arch. Biochem. Biophys.* **1974**, *16*, 665.

[41] Stone, K. J.; Strominger, J. L. *Proc. Nat. Acad. Sci.* **1971**, *68*, 3223.

[42] National Center for Biotechnology Information (NCBI) database, accessed Oct 2008 at http://www.ncbi.nlm.nih.gov/, 2008.

[43] Kampmeier, J.; Dreisewerd, K.; Schurenberg, M.; Strupat, K. *Int. J. Mass Spectrom. Ion Processes* **1997**, *169/170*, 31–41.

[44] Strupat, K.; Karas, M.; Hillenkamp, F. *Int. J. Mass Spectrom. Ion Processes* **1991**, *111*, 89–102.

[45] Yao, J.; Scott, J. R.; Young, M. K.; Wilkins, C. L. *J. Am. Soc. Mass Spectrom.* **1998**, *9*, 805–813.

[46] Fournier, I.; Beavis, R. C.; Blais, J. C.; Tabet, J. C.; Bolbach, G. *Int. J. Mass Spectrom. Ion Process.* **1997**, *169/170*, 19–29.

[47] Qiao, H.; Spicer, V.; Ens, W. *Rapid Commun. Mass Spctrom.* **2008**, *22*, 2779–2790.

[48] Fournier, I.; Marinach, C.; Tabet, J. C.; Bolbach, G. *J. Am. Soc. Mass Spectrom.* **2003**, *14*, 893–899.

[49] Matthias, G.; Karas, M. *J. Mass Spectrom.* **1999**, *34*, 467–479.

[50] Verentchikov, A. N.; Smirnov, I.; Vestal, M. L.; In *Proceedings of the 47th ASMS Conference on Mass Spectrometry and Allied Topics*, 1999.

[51] Karas, M.; Kruger, R. *Chem. Rev.* **2003**, *103*, 427–439.

[52] Loboda, A. V.; Chernushevich, I. V. *Int. J. Mass Spectrom.* **2005**, *240*, 101–105.

Chapter 3

The effect of the laser beam profile on the sensitivity in orthogonal-injection MALDI TOF mass spectrometry

3.1 Introduction

A successful MALDI TOF process involves several important steps: sample preparation, laser desorption/ionization, extraction and separation of ions based on the mass-to-charge ratio, and ion detection. The properties of each step have been studied not only to clarify the puzzling aspects of MALDI process, but also to improve the performance of this technique. Currently most of the investigations on the MALDI process have been done by varying one or more of the relevant parameters in each step. The research work related to laser properties has always been one of the most important topics since the introduction of MALDI [1, 2]. Many fundamental studies have been carried out on the roles of different laser parameters on the desorption/ionization of MALDI. These parameters include the laser wavelength, pulse duration, laser fluence (laser energy per pulse and unit area), laser spot size, the laser beam incident angle, and the laser beam profile. A brief introduction to these studies is given as follows.

1. Laser wavelength

Currently the laser wavelengths for the MALDI process are mainly working in two ranges: ultraviolet (UV) and infrared (IR). For UV lasers the wavelength typically ranges from 266 - 355 nm [1–4]. The N_2 laser, emitting at 337 nm and the Nd:YAG laser (frequency-quadrupled (266 nm) or frequency-tripled (355 nm)) are two of the most commonly used UV lasers. For IR lasers, preferred infrared radiation is in the mid-IR wavelength region from about 2.7 μm to about 10 μm [5–8]. Most commonly, erbium solid state lasers like the Erbium Yttrium-Aluminum-Garnet laser (Er:YAG) or Erbium Yttrium-Scandium-Gallium-Garnet laser (Er:YSGG) emitting at wavelengths of 2.94 μm [5, 9] and 2.79 μm [6] are widely used. In MALDI, the wavelength range first determines the selection of suitable matrices. As a rule of thumb for matrix selection, the matrix compounds must show sufficient optical absorption at the particular wavelength range.

In UV MALDI, the matrix molecules absorb the laser irradiation strongly via electronic transitions [1, 10]. There is no direct energy transfer to the analyte molecules from the laser beam. This can protect the analyte molecules from being directly dissociated, permitting the generation of intact macromolecular ions. The optical absorption spectra for some common UV matrices such as DHB, sinapinic acid (SA), and α-HCCA have been studied either from solid phase [11] or solution phase of the matrices [12]. All these matrices showed strong optical absorption peaks in the UV wavelength range. The absorption coefficient of α-HCCA is much higher than those of DHB and sinapinic acid (SA) matrices at the wavelength of 337 nm. This absorption difference seems to be consistent with the fact that the threshold laser fluence of α-HCCA is much lower compared to DHB and SA matrices due to its higher UV absorption.

However, in IR MALDI, the laser energy absorption is normally achieved by vibrational excitation of the matrix molecules instead of an electronic transition. This wavelength range is particularly close to the O-H stretch or N-H stretch vibrations ($\lambda \sim 3\mu$m). The molecules constituting the natural environment of proteins (especially water) have strong absorption at this wavelength range, leading to their possible use as IR MALDI matrices.

Some other commonly used matrices at IR wavelength range are glycerol, succinic acid, and urea. An important advantage of using IR lasers is the possibility to use matrices that do not alter the physiological condition of the sample under investigation, in contrast to the acidic matrices that are required for UV MALDI.

Although some studies showed that the spectra from both UV and IR MALDI for a given protein with the same matrix were strikingly similar [13], there are still some differences between them: (1) IR MALDI has a general tendency to form higher charge states compared to UV MALDI; (2) A dramatically reduced metastable fragmentation is observed in IR MALDI compared to UV MALDI. Although the IR-desorbed ions may have higher internal energy than the UV-excited ones because of the direct vibrational excitation of the IR laser, the decreased metastable decay of IR MALDI ions may suggest that the internal energy of the analyte ions, as they emerge from the ion plume, is strongly influenced by the ion cooling in the expanding plume. It has been suggested that this stronger cooling in IR MALDI is related to the desorbed sample volume which is typically 100 times larger in IR as compared to in UV MALDI. As a result of this, elevated pressure ion sources are expected to be much more effective in suppressing metastable fragmentation in UV as compared to IR MALDI; (3)Although about 100 - 1000 times more material is desorbed by IR as compared to the UV laser beam, comparable intensity is obtained for single laser shot in the IR and UV lasers. This might be due to the fact that the material desorbed by the IR-MALDI is either primarily removed as larger clusters and small particles, and/or the ion yield is smaller by two to three orders of magnitude [6].

2. Laser pulse duration

The influence of laser pulse duration on desorption/ionization of MALDI has also been studied. Demirev *et al.* [14] examined the MALDI performance with both an excimer pumped dye laser (wavelength 248 nm, pulse width 560 fs) and a N_2 laser (wavelength 337 nm, pulse width 3 ns). The experimental results showed that the threshold laser fluence for ion desorption/ionization was about the same order of magnitude for both lasers and did not obviously depend on the laser pulse duration. It seemed that the amount of laser

energy deposited onto the sample, rather than the laser power, was the most important parameter affecting the threshold fluence in the MALDI process. Dreisewerd *et al.* [15] compared two N_2 lasers (337 nm) with 0.55 and 3 ns pulse duration for the MALDI process, respectively. Similar results were also obtained and indicated that neither the threshold laser fluences nor the ion signal intensity changed too much with two different pulse widths. It was concluded that the desorption/ionization process was essentially determined by the energy supplied in the studied pulse width range, rather than by the rate of energy flow into the sample. In IR MALDI, a very similar threshold laser fluence was also observed for the Er:YAG laser (2.94 μm) for the pulse duration at 100 and 185 ns. And a weak tendency towards reduced threshold fluences with laser pulse length was found by going from the 75-100 ns long pulses of the Erbium lasers (2.94 μm) to the short 6 ns OPO laser (optical parametric oscillator)(2.79 μm) [16]. It is also reasonable to think that if the total energy of the pulse is insufficient to desorb/ionize the sample, merely increasing the rate at which the amount of energy is added would have no effect. It is the total energy deposited within a given area that determines the magnitude of that effect. Therefore, the laser fluence is the appropriate measure of laser intensity for MALDI not the irradiance.

In principle, different laser pulse widths should have produced some effects between the nanosecond and femtosecond lasers. In the case of the nanosecond laser, the ablation begins while the laser pulse is still irradiating the surface. The effect of laser irradiation on the expanding plume is not well understood, but some excitation of matrix and other molecules is generally presumed. Laser excitation and ionization of the plume is also an attractive hypothesis for nanosecond laser ionization because of the large neutral yield in MALDI [17]. For the femtosecond laser pulse, on the other hand, the energy is absorbed completely prior to any movement of the matrix. No more interaction between the laser pulse and the expanding ion plume will happen. So there should have been some difference between these two different time scale laser pulses. The reason for the weak influence of the pulse width in the MALDI process might be consistent with the idea that the secondary reactions (such as the proton transfer, electron transfer, and cationization) during the

expansion of ion plume which is in the time scale up to several microseconds may be so dominant that the primary ionization events (related to the pulse width) are not reflected in the final ion mass spectrum [18].

3. Laser incident angle

The influence of the incident angle of the laser beam was also studied [19]. The threshold energy and the ion yield have been determined for incident angles from 35° to 60° with respect to the target surface normal. The measurements with the sinapinic acid matrix demonstrated that neither the threshold energy nor the dependence of ion yield on the laser energy varied with the incident angle within the range studied. Hence the threshold fluence for protein ion production in MALDI was proportional to the cosine of the angle of incidence. The reduction in threshold fluence when changing from normal to glancing incidence was also observed for sinapinic acid and α-HCCA matrices [20]. However, it was also observed that there was only a minor influence of the angle of incidence for the DHB matrix. This dependence of the threshold fluence on the laser incident angle might be related to the crystallization of the matrices used. For the DHB matrix, which forms considerably larger crystal needles located around the rim of the droplet and exposes different crystal surfaces in all directions [4], the dependence on laser incident angle was not observed. However, for sinapinic acid and α-HCCA, which both form flat sheets lying preferentially flat on the metal substrate, the laser incident angle dependence becomes more prominent.

4. Laser fluence and beam spot size

Several experiments have reported that the ion yield measurements strongly depend on the laser fluence and the laser spot size [20–26]. Here the ion yield refers to the number ions desorbed per laser pulse. In these experiments, a steep increase of the ion yield was normally observed when the laser fluence just exceeded the threshold fluence. But the ion yield gradually reached saturation when the fluence went much higher. This saturation might result from the increased ion fragmentation or some other losses such as the insufficient cooling of the relatively large plume size. A power-law dependence of

the ion yield per shot on the laser fluence was found. The powers of fluence dependence ranging from 4 to 10 were determined [21, 24, 25]. The fluence dependence was also found to depend on the matrix used. All these results were mainly used to investigate the ion desorption process, and have not been used, at least explicitly, to optimize the experiments for best sensitivity.

Measurements of ion yield and threshold fluence as a function of spot size have indicated a very steep dependence (to the 3rd power of the area) and have given the impression that larger spot sizes therefore provide better sensitivity [24]. However, such analysis did not take account of saturation fluence, which is higher for smaller spot sizes, and did not consider the integrated sensitivity at all. We made a systematic study of the influence of laser fluence and beam spot size on the ion desorption. The results have been published [27] and will be elaborated in another chapter.

5. Laser beam profile

Both N_2 lasers and Nd:YAG lasers are commonly used in the UV-MALDI experiments. However N_2 lasers generally give much better sensitivity (total ion yield from a given sample spot) than Nd:YAG lasers at the same laser fluence. Recently the laser beam profiles of these two lasers were examined by Holle *et al.*, showing that the laser beam profile, rather than the wavelength and pulse width, played an important role in affecting their different MALDI performances [28]. The complex beam profile pattern of the N_2 laser was superior to that of the Nd:YAG laser (near-Gaussian distribution). It also demonstrated that a prominent enhancement in sensitivity of the Nd:YAG laser could be achieved by structuring its Gaussian beam profile into a beam profile similar to the N_2 laser. However, the reason for this improvement of the Nd:YAG laser was not clearly understood. In their experiment, the laser beam was directly introduced into the mass spectrometer using optical lenses.

Due to the convenience and compact set-up with the fiber optics, optical fibers have been widely used to transmit the laser energy onto the sample target in MALDI mass spectrometry [24, 25]. By using the optical fiber, the laser beam profile at the end of the

fiber will be affected by the fiber properties such as interference of the fiber modes and the mode-mixing. Although some studies on the fiber optics in MALDI have been carried out such as achieving a 'flat-top' beam profile [24, 29, 30] and studying the influence of fiber size on the MALDI mass spectrum [31], there is still not a systematic study of the influence of laser beam profile on the ion desorption/ionization in MALDI with fiber optics.

These fundamental studies have given a better understanding about the mechanisms of MALDI process, which helps to optimize the laser properties to achieve the best MALDI performance. Recently MALDI tissue imaging mass spectrometry has attracted much interest, starting with the pioneering work of Caprioli *et al.* [32–34]. This prompts the study of laser properties from more practical point of view to improve the performance of MALDI imaging experiments. Although the N_2 laser has been widely using for routine applications, this type of laser inherently has two significant limitations for MALDI imaging: the maximum repetition rate of current commercial N_2 lasers is limited to about 50 Hz, and the average life span is about 2×10^7 - 6×10^7 shots. In contrast, Nd:YAG lasers can easily achieve repetition rates of larger than 1000 Hz and have a life span of typically several 10^9 shots. It seems that the Nd:YAG laser is more attractive in MALDI imaging applications in terms of the data acquisition rate. However, as discussed above it has been realized that the ion desorption performance of Nd:YAG lasers is not as good as N_2 lasers in terms of sensitivity, which is particularly important in MALDI imaging mass spectrometry since it finally determines the spatial resolution. So it is important to improve the ion desorption performance of Nd:YAG lasers in order to make them a better choice for MALDI imaging.

In this chapter, the influence of laser beam profiles for both the N_2 laser and the Nd:YAG laser with fiber optics is systematically studied. Comparison is firstly made between these two lasers in the ion desorption/ionization of MALDI with fiber optics. In order to figure out their differences in the MALDI performance, the laser beam profiles are then examined with a series of optical fibers ranging from 10 to 200 μm in diameter. The effects of twisting the fiber during irradiation or using longer fiber on the laser beam profile and

ion yield are also discussed.

3.2 Experimental

3.2.1 Instrumentation

The beam profile experiments were performed on a modified AB-Sciex Qstar instrument [35], supplied by MDS Sciex (Concord, ON, Canada), in which the incident laser angle is 60° shown in Fig.3.1. The accelerating voltage is about 11 kV. The cone aperture is about 4 mm, and is about 5 mm away from the sample target. The ion source pressure is maintained about 1 Torr. However, the pressure was not accurately monitored in the source region, and may have been different by up to a factor of 2.

Two types of lasers were used: a N_2 laser at 337 nm with a pulse duration $\sim$4 ns, and pulse energy $\sim$250 μJ (model VSL-337ND, Laser Science Inc., Franklin, MA, USA), and a tripled Nd:YAG laser at 355 nm with a pulse duration $\sim$ 8 ns, and pulse energy $\sim$ 50 μJ (JDS Uniphase, model S3558-100Q; Manteca, CA, USA). The beam was coupled through a three-lens optical system (shown in Fig.3.1) into 2-m fused-silica fiber optic patch cords of various diameters from 10 to 200 μm (OZ Optics Ltd., Ottawa, ON, Canada). The fibers had a step-index profile with a numerical aperture $\sim$ 0.22. Alignment was performed with an attenuated beam by maximizing the transmitted intensity, and then backing the fiber off a short distance to avoid damaging the end with the unattenuated beam. The coupling efficiency was not accurately determined, but was about an order of magnitude lower for the 10-μm fiber than for the 200-μm fiber. Once aligned, the fiber patch cords could be interchanged quickly, with only minor adjustment necessary. Alignment of the larger fibers was quite easy, and they lasted almost indefinitely. The smaller fibers were often damaged during alignment or after some 10^4 or 10^5 shots with the N_2 laser at its highest fluence, but they typically lasted for more than 10^8 shots with the Nd:YAG laser near saturation fluence. The 2-m patch cords are relatively inexpensive and damaged
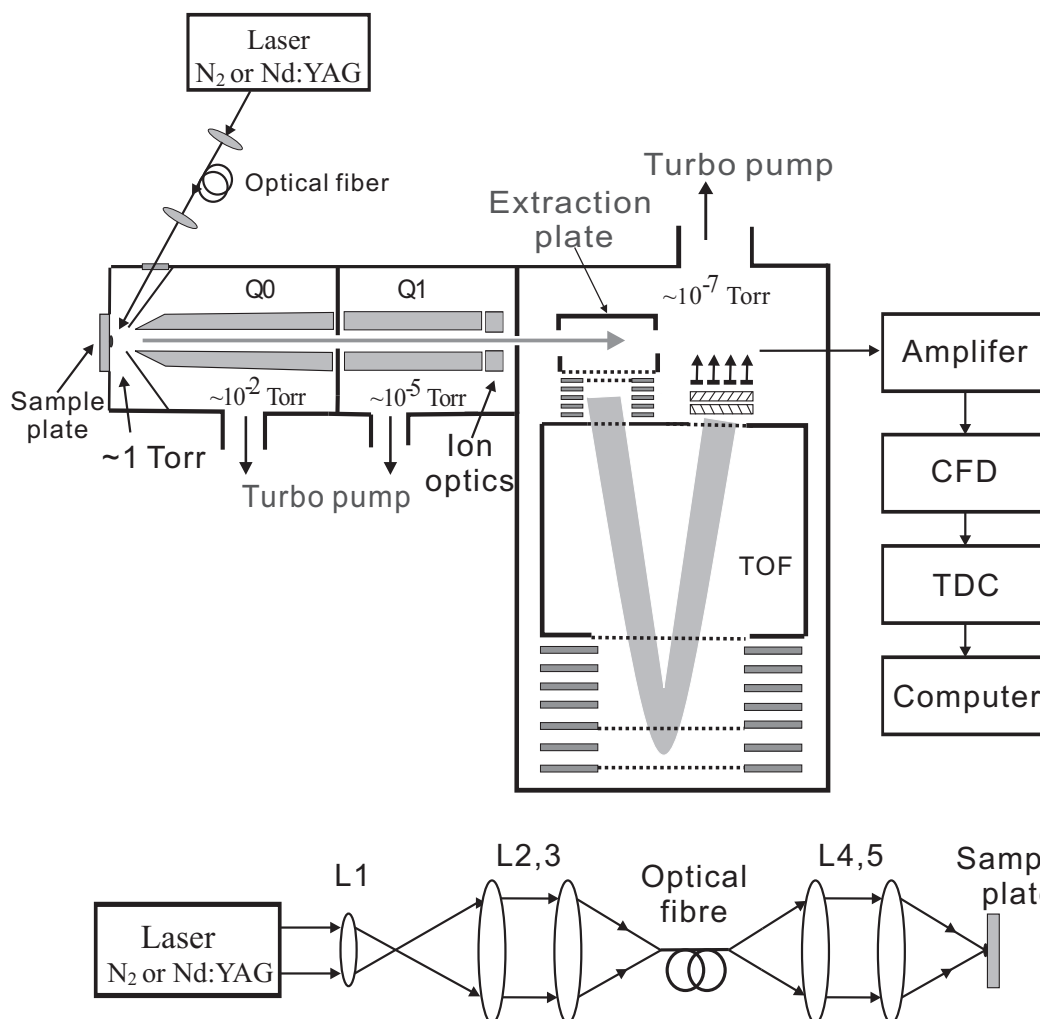
Figure 3.1: Schematic diagram of the orthogonal-injection MALDI TOF mass spectrometer. The laser incident angle were set at 60.. The laser beam was focused into the fiber by three lenses. L1: f = 5mm, L2,3: f2 = f3 = 10 cm. The fiber output was imaged onto the sample plate by two aspherical lenses L4,5: f4 = f5 =10 cm.
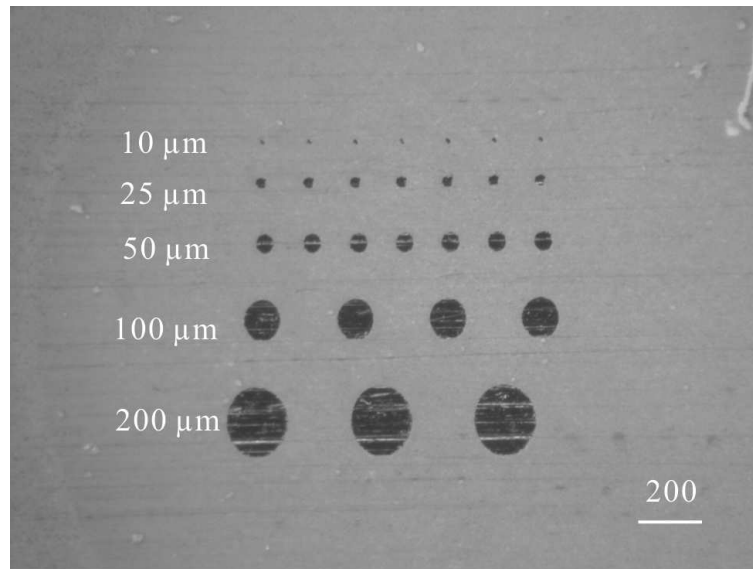
Figure 3.2: Burn marks of N2 laser obtained with fibers of 2-m long and different diameters. The sample was prepared by thin layer preparation with α-HCCA matrix. The laser fluence was set well above threshold.

fibers were simply replaced. Some measurements were also performed with a 30-m long fiber with a 10-μm diameter.

The fiber output was imaged 1:1 onto the target with two custom-made 10-cm focal length aspherical lenses (R. Mathews Optical Works Inc., Poulsbo, WA, USA) arranged in infinite conjugation shown in Fig.3.1. This arrangement allowed the image size to closely approximate the fiber diameters, as shown by the burn marks in Fig.3.2.

A J3 pyroelectric joulemeter (Molectron Detector Inc, Portland, OR. USA) has a flat spectral response over the two wavelengths used, and was used to measure the pulse energy. To estimate the absolute fluence, the energy was measured at the end of the fiber using the calibration supplied with the joulemeter, and the fluence was then calculated based on the size of the burn marks in Fig.3.2, without correcting for losses due to the focusing optics and the entrance window. The absolute fluence values should therefore be regarded as approximations, probably somewhat higher than the actual values.

The spatial profiles of the fiber output were obtained off-line using an optical system with an 80-mm double-convex lens and a 1.3$\times$ video lens system (infinitistix with 68 mm
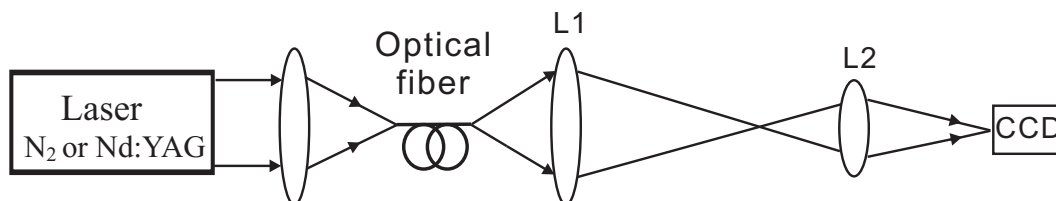
Figure 3.3: Schematic diagram of the optical setup for recording the beam profile using a CCD camera. The optics of focusing the laser beam into the fiber is the same as in Fig.3.1. Two lenses were used to image the output of the fiber with a CCD camera. L1: f1 = 80 mm, L2: 1.3× video lens system. CCD camera: 1.3 inch, 640×480 pixels.

working distance, 1.3× magnification; Infinity Optical, Co, USA) to image the fiber end onto a 1/3 inch CCD camera (640×480 pixels, KTC-110, Key Tech. Corp., Taiwan) shown in Fig.3.3. The fiber end was placed near the focal point of the 80-mm lens to get an additional ~ 15 times magnification. The CCD pixels spacing is 10.4 μm, corresponding to approximately 0.5 μm object distance per pixel. This probably exceeds the optical resolution limited by aberrations or diffraction, but, as seen in the Results section below, the system is capable of showing fairly subtle changes in profile features (between lasers, or due to fiber twisting), which are significantly smaller than the diameter of the 10-μm fiber. The image profiles were analyzed using OriginPro7.5 (OriginLab Corporation, Northampton, MA, USA).

3.2.2 Sample preparation

All the samples were purchased from the Sigma-Aldrich Company (Oakville, ON, Canada) and used as supplied commercially without further purification. In this experiment, samples were prepared with only one matrix, 4-hydroxy-α-cyanocinnamic acid (α-HCCA). The analyte used was substance P (1347 Da). Thin layer sample preparation [36] was used to improve the signal reproducibility from spot to spot. The α-HCCA matrix was first dissolved in ultrapure acetone to a saturated solution. A volume of 1 μL of this solution was applied onto the stainless steel target, forming a thin layer of matrix with crystal size in the range of 2 to 3 μm after fast evaporation of the solvent. The analyte was dissolved in bi-distilled water at a concentration of 50 pmol/μL, and mixed 1:1 with

another α-HCCA matrix solution saturated in aceonitrile/water (1:1, v/v) and 0.1% tri-fluoroacetic acid (TFA). A 1 μL aliquot of this premixed solution of matrix and analyte was deposited on top of the existing matrix layer and allowed to dry at the room temperature, forming a circular layer of mixture of matrix and analyte, resulting in a layer ~ 2 μg/mm^2 matrix, and about 3 pmol/mm^2 analyte.

3.2.3 Ion signal variation

Before performing the experiments, the ion signal fluctuation from spot to spot was checked for the sample preparation. Different sample spots were irradiated by the laser beam until the sample was completely desorbed. The total ion yield (sensitivity) from each sample spot was obtained by integrating the area of the molecular ion peaks. The relative deviation (the ratio of deviation from the mean over the mean) of the integrated ion yield from 50 sample spots was plotted in Fig.3.4a. From this graph, it showed that the fluctuation of integrated ion yield for all the sample spots was within the range of $\pm 25\%$. This total ion yield fluctuation was relatively large. One option of reducing the fluctuation was to use the average of more sample spots. The relative deviation was reduced to about $\pm 5\%$ by using the average of 10 sample spots shown in Fig.3.4b. This provided a better signal reproducibility for the measurement. In the following experiments, the ion yield measurements were averaged from 10 different sample spots. The error bars were considered based on this fluctuation.

3.3 Results and Discussion

3.3.1 Ion yield comparison between N$_2$ and Nd:YAG lasers

As mentioned in the introduction, experiments reported by Holle *et al.* indicate that the complex beam profile that they observed with a N$_2$ laser gives better integrated ion yield than the simple Gaussian beam profile with a Nd:YAG laser [28]. In their measurements,

a

b
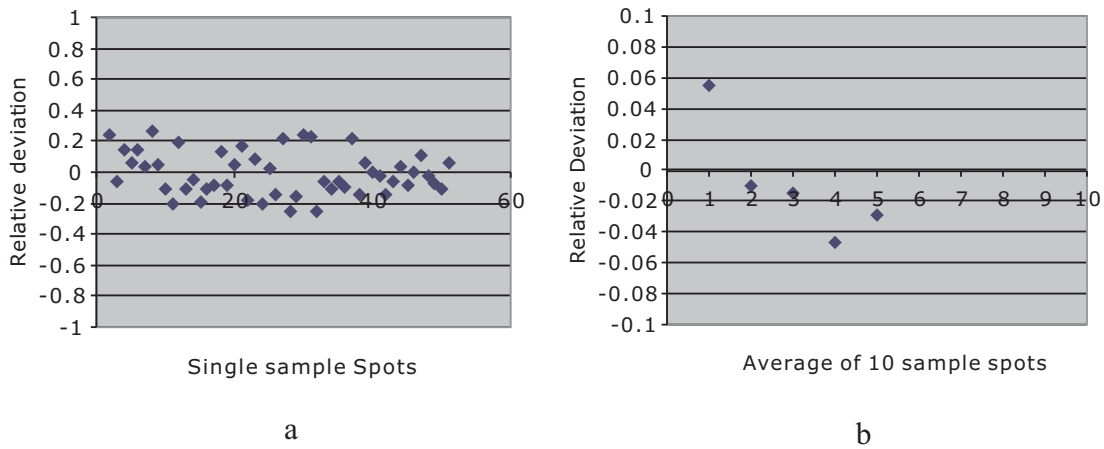
Figure 3.4: Statistics of signal fluctuation from sample spot to spot. (a) relative deviation of integrated ion yield of 50 sample spots. (b) relative deviation of the integrated ion yield with the average of 10 sample spots using the same data in (a). The ion yield fluctuation is reduced within $\pm 5\%$.

the laser beam was directly introduced through lenses to the mass spectrometer.

We have made a similar comparison using fiber optics. In this comparison, the same conditions: matrix (α-HCCA) and analyte (substance P), laser energy, and 2-m long fiber, were used. Similar results for both lasers were observed with a 25-μm fiber in previous studies [28] shown in Fig.3.5. The integrated intensity of substance P saturates after about 100 shots in the case of the Nd:YAG laser, but continues to increase for at least 500 shots with the N_2 laser, to a value about 2.5 times higher. The effect depends to some extent on the laser fluence (it increases), and the fiber diameter, but, in all cases, the N_2 laser gives higher sensitivity.

The dependence of integrated ion yield on laser fluence was also compared for these two lasers. Because the pulse energy of the Nd:YAG laser is much lower than the N_2 laser, only a limited range of laser fluences was studied. The results are shown in Fig.3.6. Fig.3.6A and B were obtained with 25 and 10 μm fibers, respectively. From these two graphs, it is clear that the integrated ion yield increases with laser fluence for both lasers. And the N_2 laser shows consistently higher sensitivity than the Nd:YAG laser for both fibers. For the 25 μm fiber, the integrated ion yield of the N_2 laser is an average 2.5 times higher
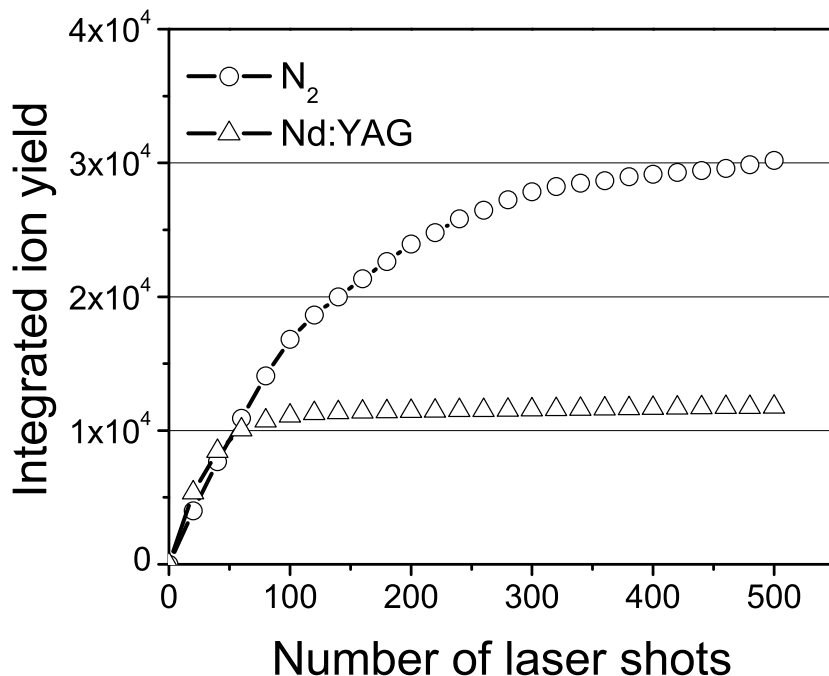
Figure 3.5: Comparison of the integrated ion yield for the N_2 laser and the Nd:YAG laser using 2-m long fibers with 25 μm diameter.Ions for protonated substance P desorbed from the α-HCCA matrix were analyzed.

than that of the Nd:YAG laser. Both lasers have nearly the same threshold fluence for the ion desorption/ionization. For the 10 μm fiber, the integrated ion yield of the N_2 laser is about 1.5 times higher than that of the Nd:YAG laser. The ratio in the integrated ion yield between these two lasers becomes smaller as the fiber size decreases.

3.3.2 Laser beam profile study

What could contribute to the difference in integrated ion yield between these two lasers? As mentioned, we used same experimental conditions for this study except for the inherent differences between these two lasers. The main differences between them are their wavelengths, pulse durations, and probably their beam profiles. Studies about the optical absorption showed that there was not a significant difference of the optical absorption
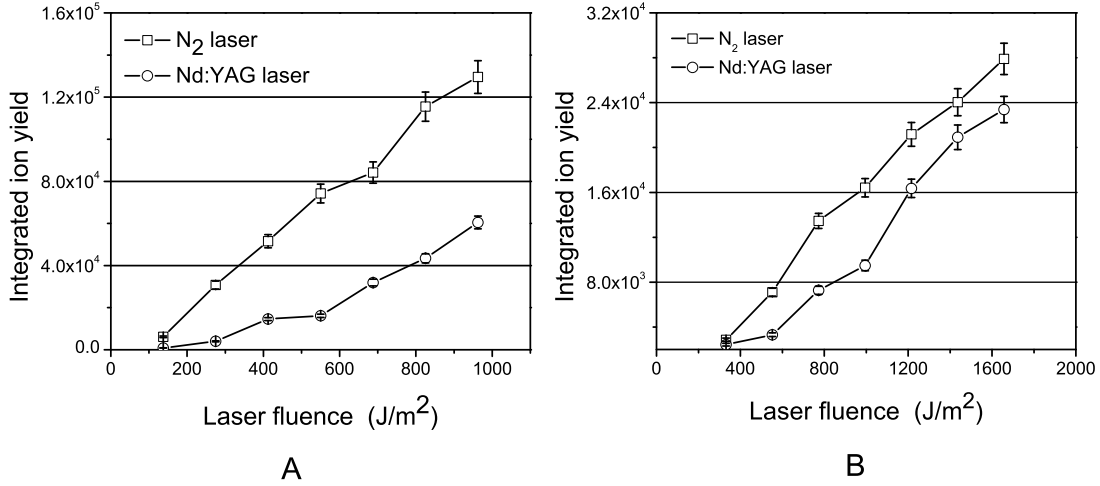
Figure 3.6: Dependence of integrated ion yield on the laser fluence for 25 μm fiber (A) and 10 μm fibers (B). The N2 laser shows consistently higher ion yield than the Nd:YAG laser for both fibers. The ratio in the integrated ion yield between these two lasers becomes smaller as the fiber size decreases.

coefficients of α-HCCA for both the N$_2$ (337 nm) laser and the Nd:YAG laser (355 nm), and in fact it showed a slightly higher absorption for the Nd:YAG laser at 355nm [11]. So the observed difference in integrated ion yield is therefore unlikely to be attributable to the difference in laser wavelength. Studies on the laser pulse duration also demonstrated that the ion desorption/ionization process was essentially determined by the total energy supplied in the pulse range from picosecond to nanosecond, rather than the rate of energy flowing into the sample [14, 15]. The previous study showed that the complex beam profile of the N$_2$ laser contributed to its better performance than Nd:YAG laser (Gaussian beam profile) [28]. Since we also observed similar difference in ion yield between these two lasers with fiber optics, we also studied the influence of laser beam profile on the integrated ion yield was also studied. One important thing is that the fiber optical properties should be taken into account when analyzing the laser beam profiles.

The laser beam profiles were recorded using the described off-line imaging system. The sizes of fibers range from 10, 25, 50, 100, and 200 μm in diameter. The length of the fiber is about 2 meters. The laser beam profiles are shown in Fig.3.7. The beam profiles

are actually speckle patterns. From these images, it is clear that the speckle patterns of the Nd:YAG laser are more defined than those of N_2 with all these fibers studied. The speckle pattern is relative smooth and becomes almost 'flat-top' profile for N_2 laser with 200 μm. With the reducing of fiber diameter, well-defined speckle patterns on the scale of a few μm for the 25 and 10 μm fibers are observed. These patterns are consistent with a superposition of excited fiber transmission modes [37]. The fiber modes are the solutions of the electromagnetic fields satisfying the Maxwell's equation and the boundary conditions of the optical fiber. Each fiber mode has its distinctive pattern of the electromagnetic fields as it propagates. This pattern actually shows the intensity distribution of electromagnetic field at the transverse plane of the fiber. Fig.3.8 shows some typical fiber mode patterns. In fact, light launched into a multimode fiber will excite a superposition of different modes, which have a rather complicated shape.

The number of modes transmissible within the fiber affects the beam profile. For a step-index fiber, the calculated number of fiber modes (M) is proportional to the V parameter [38] which can be expressed as follows:

$$V = \frac{2\pi a}{\lambda} N.A. \tag{3.1}$$

$$M = \frac{1}{2}V^2 \tag{3.2}$$

where a is the core radius of the fiber, λ is the wavelength, N.A.=$(n_1^2 - n_2^2)^{1/2}$ is the numerical aperture of the fiber. This equation shows the number of fiber modes decreases as the fiber size becomes smaller. For example, in the case of 10-μm fiber, it can transmit as many as about 200 higher order modes (N.A. $\sim$ 0.22, $\lambda \sim$ 337 nm). However, the number of modes is greatly affected by the launching condition of the laser, the interference of modes, and the mode-mixing property of fiber optics. It is clearly shown in Fig.3.7, for the 10 μm the two lobes are consistent with preferential excitation of the LP_{11} mode (where LP indicates linearly polarized) [37] shown in Fig.3.8.
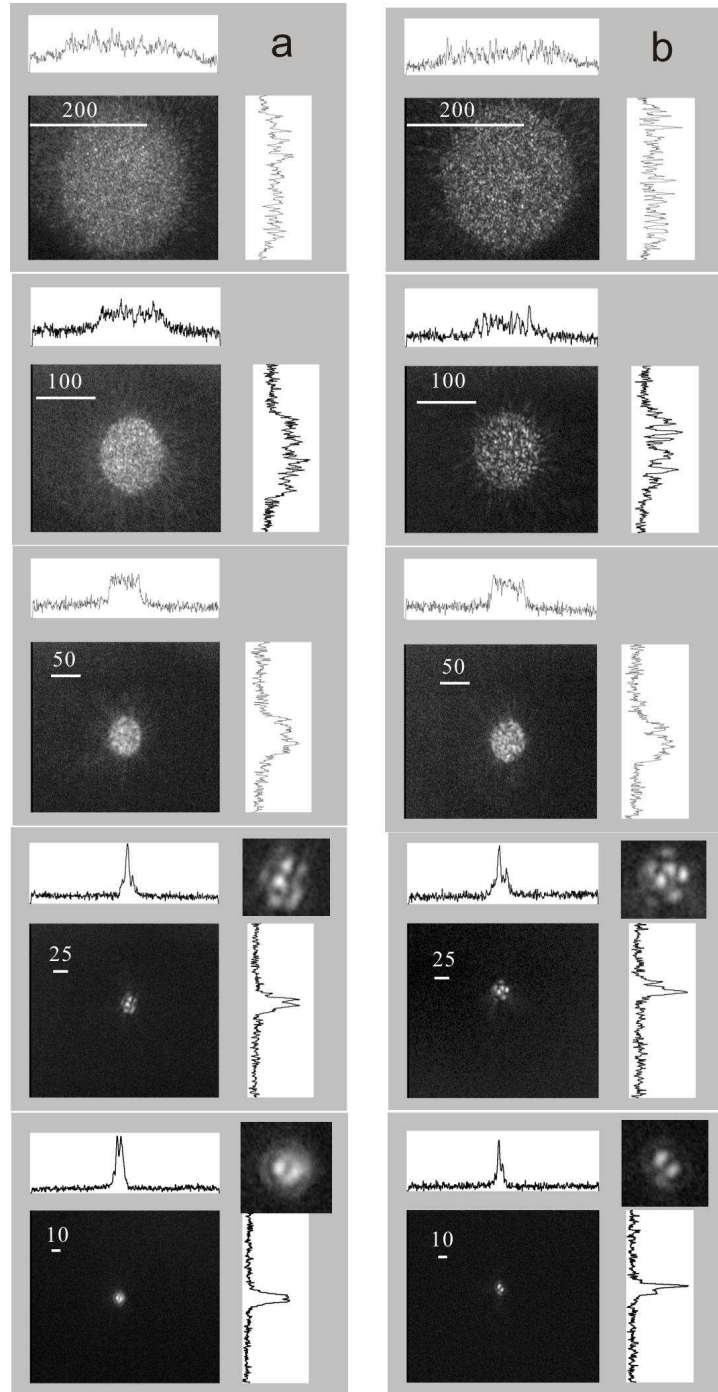
Figure 3.7: Profiles of the laser spots obtained using 2-m long optical fibers with (a) the N_2 laser and (b) the Nd:YAG laser. The indicated scales correspond to the fiber diameter in μm. Only single frame images are shown. The number of fiber modes decreases with reducing fiber diameters, and discrete modes seem to be evident with 10 μm fibers.
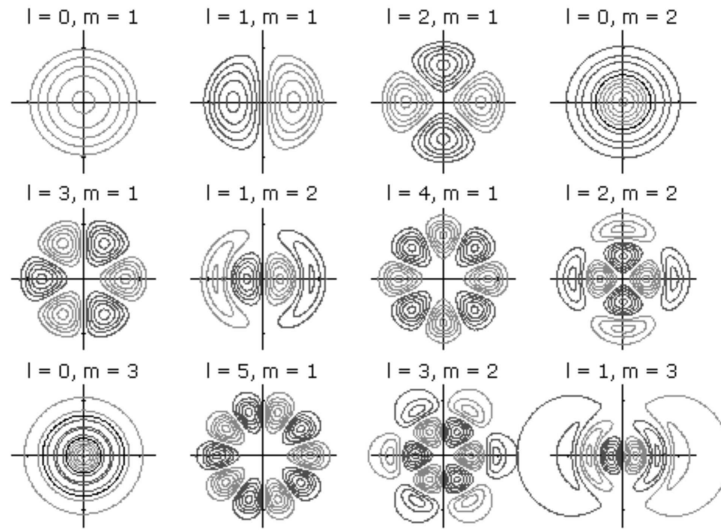
Figure 3.8: The intensity distribution on the transverse plane of the fiber for some typical guided modes.

It was also observed that the laser beam profile did not change from shot to shot for both lasers shown in Fig.3.9, which was different from the previous observation that the beam profile of N_2 varied from shot to shot [28]. This might be due to the fact that the beam profile is mainly affected by the launching condition of laser beam, the number of fiber modes transmitted, the mode coupling (mixing) effect, and the interference between modes. Once all these conditions are fixed, the beam profile at the end of the fiber is not going to change.

### 3.3.3 Detailed analysis of the beam profiles

The laser beam profiles from both lasers look quite similar with all fibers as shown in Fig.3.7. However, it is also visible that the beam profile of the Nd:YAG laser seems much sharper than that of the N_2 laser. In order to quantify this difference, the number of pixels covered by the laser beam profiles were analyzed. For simplicity, we mainly studied 10 and 25 μm fibers because of their distinctive and well-defined beam profiles. Since the absolute intensities of the recorded beam profile images were different, normalization with respect to the maximum intensity was made for each beam profile. Then the number
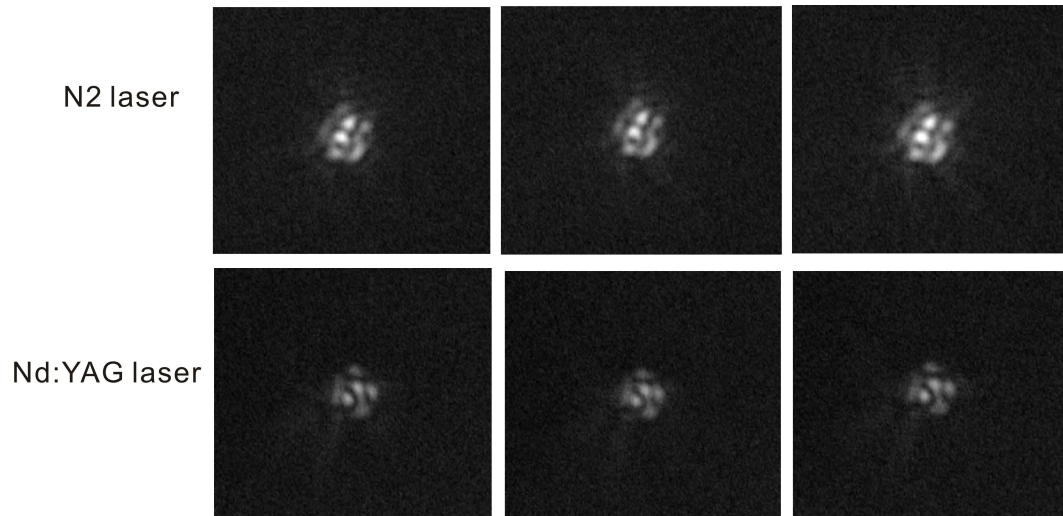
Figure 3.9: Examination of laser beam profiles from continuous laser shots for both the N_2 laser and the Nd:YAG laser. For both lasers, the beam profile does not change from shot to shot.

of pixels above relative thresholds (percentage of the maximum intensity) were counted. Fig.3.10 shows the average number of pixels at different thresholds for both lasers with 10 and 25 μm fibers.

Fig.3.10 shows that the N_2 laser has an average 2.5 times more pixels than the Nd:YAG laser for 25 μm fiber. More pixels mean more samples will be desorbed and higher ion yield therefore can be produced. These statistics are quite consistent with the comparison of integrated ion yields as shown in Fig.3.6A. For the 10 μm fiber, it shows that the number of pixels of the N_2 laser are an average 1.5 times more than that of the Nd:YAG laser. This result is consistent with the data as shown in Fig.3.6B. From the pixel statistics and a detailed examination of the beam profiles, it follows that the features of the Nd:YAG profiles are sharper; that is, the bright spots decrease more steeply to lower values. Given the steep near-threshold-like dependence of ion yield with laser fluence, this seems to offer a consistent explanation for better sensitivity with N_2 laser. The pattern observed with the Nd:YAG laser simply desorbs ions from a smaller fraction of the irradiated spot.
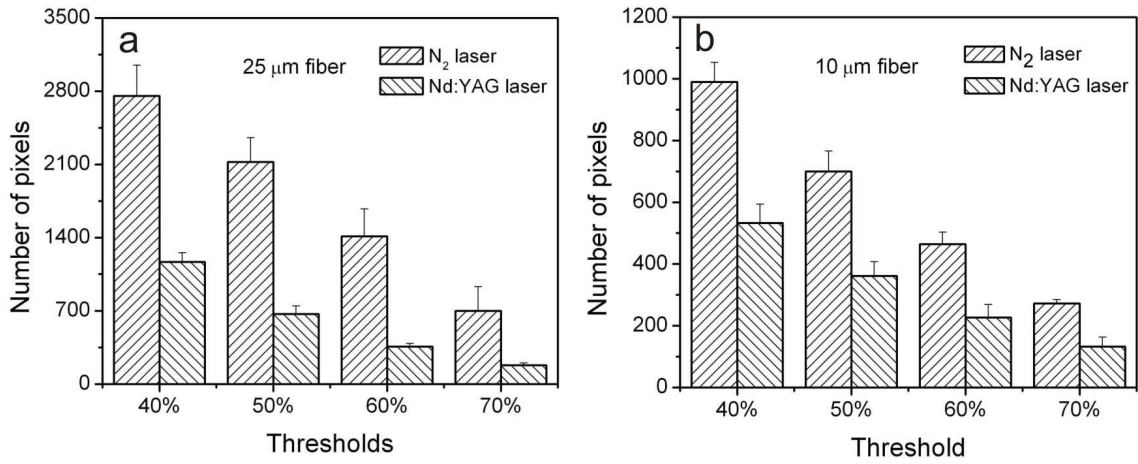
Figure 3.10: Statistical analysis of the number of pixels of the laser beam profiles for 25 μm fiber(a) and 10 μm fiber (b). It is obvious that the N2 laser produces more pixels than the Nd:YAG laser for both fibers.

3.3.4 Improving the ion yield with a uniform beam profile

Studies of the beam profiles show the possibility that more samples would be desorbed and higher ion yield could be obtained if the laser energy becomes homogeneously distributed on the sample. As inspired by the variation of beam profile from shot to shot in the case of the N_2 laser [28], which may contribute to a time-averaged uniform energy distribution during the irradiation, we found that twisting or bending the fiber during irradiation could also achieve a time-averaged spatial uniformity of laser energy. This is because the beam profile pattern is highly sensitive to the particular shape of the fiber [37], and moves around in response to continuous fiber motion. The twisting procedure simply involved grasping the fiber at two places about 20 cm apart, and moving them in circles of 10-cm diameter about 1 Hz, with the two circles π out of phase.

After twisting the fiber, it was found that the integrated ion yield increased for both lasers, especially for the Nd:YAG laser, shown in Fig.3.11. The variations of the integrated ion yield as a function of laser fluence for both twisting and without twisting the fiber were also studied shown in Fig.3.12. It clearly shows that the integrated ion yields of the Nd:YAG laser are obviously improved for different fluences. There are about 2 and 1.5 times increments for 25 μm fiber and 10 μm fiber, respectively. However the ion yield
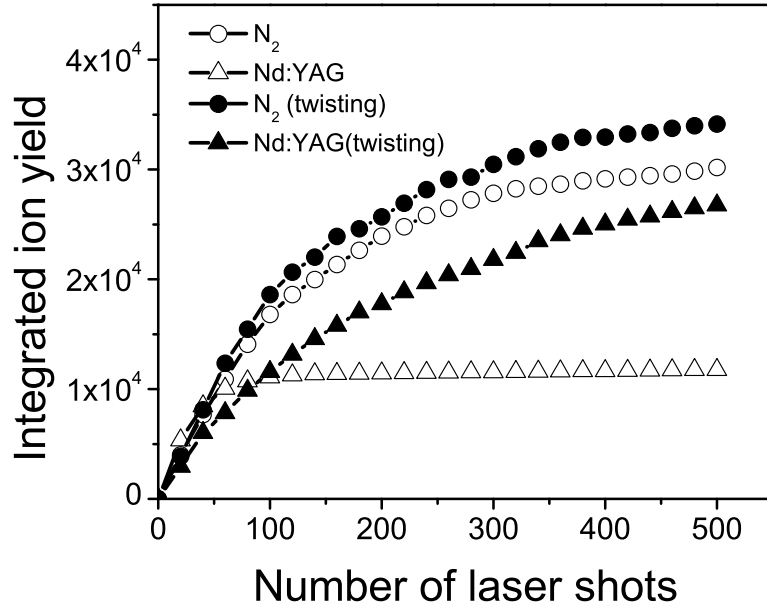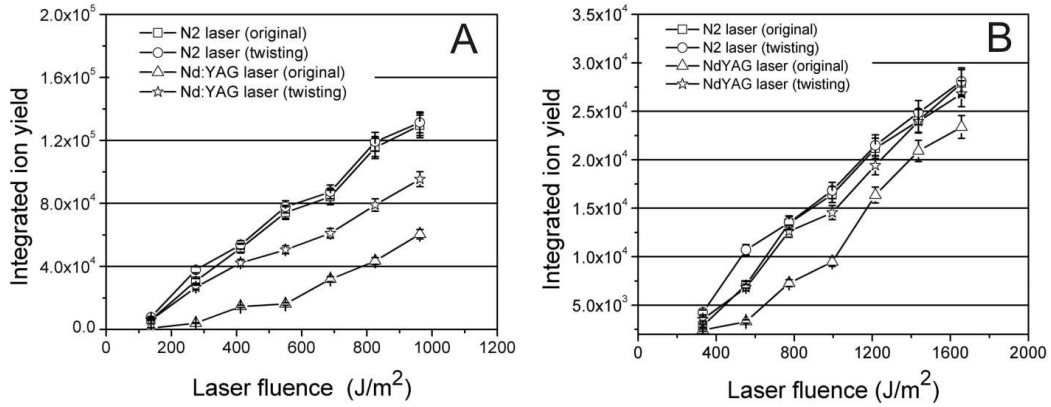
Figure 3.11: The integrated ion yield as a function of laser shots. The open symbols show the data acquired without twisting the fiber. The closed data were acquired by twisting the fiber during irradiation. The fiber used is 25 μm.

improvement for the N_2 laser is not as prominent as for the Nd:YAG laser.

The time-averaged beam distribution after twisting the fiber is shown in Fig.3.13. It shows that the laser beam profiles become much smoother. Similarly we made pixel-analysis with these more uniform beam profiles, which is shown in Fig.3.14 and Fig.3.15 for N_2 laser and Nd:YAG laser, respectively. Through the comparisons of the number of pixels, it is clear that the Nd:YAG laser has an obvious increase in the number of pixels than the N_2 laser for both fibers, consistent with the larger enhancement of the integrated ion yield of the Nd:YAG laser shown in Fig.3.12. The number of pixels becomes almost equal for these two lasers after twisting the fiber, shown in Fig.3.16, consistent with the reduced difference between these two lasers shown in Fig.3.12.

A more uniform laser profile can also be produced by using longer fibers to allow effective mode-mixing caused by microscopic imperfections in the fiber [38], and to avoid

Figure 3.12: Variations of integrated ion yield as a function of laser fluence for both twisting and without twisting the fibers. (A) 25 μm fiber, (B) 10 mum fiber. The ion yield difference of these two lasers existing prior to the fiber twisting is almost removed after the twisting effect especially for 10 μm fiber.
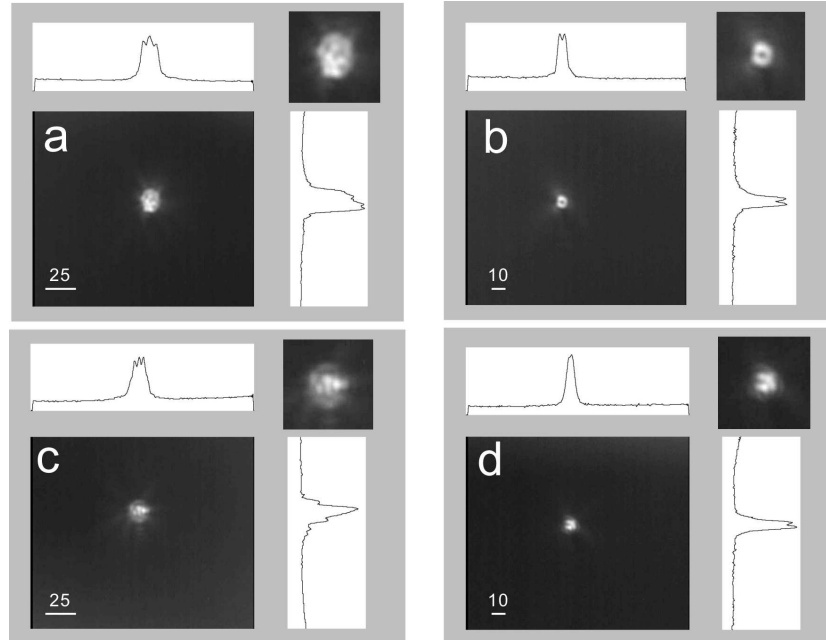
Figure 3.13: Laser beam profiles obtained from the superposition of consecutive laser shots. (a) N2 laser with 25 μm fiber,(b) N2 with 10 μm fiber, (c) Nd:YAG laser with 25 μ fiber (d) Nd:YAG laser with 10 μm fiber. The fibers were continuously twisted during recording the profiles. The indicated scales correspond to the fiber diameters. Twisting the fiber during irradiation results in a more uniform profile.
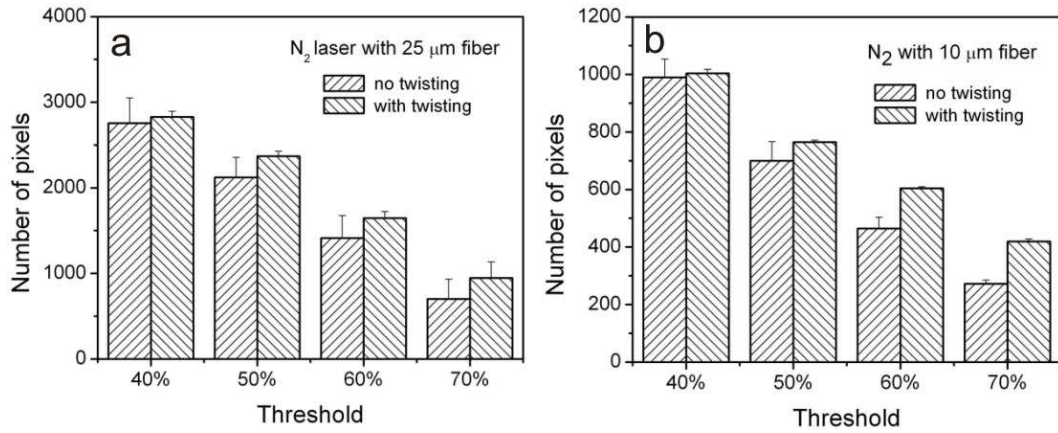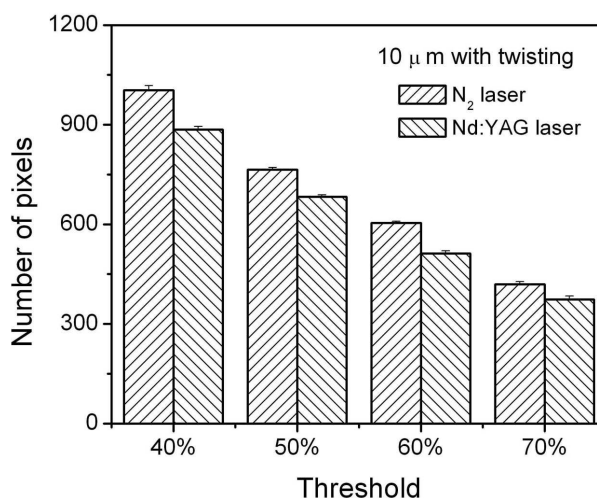
Figure 3.14: Comparison of the number of pixels with and without twisting the fibers for the N_2 laser. (a) 25 μm fiber, (b) 10 μm fiber.
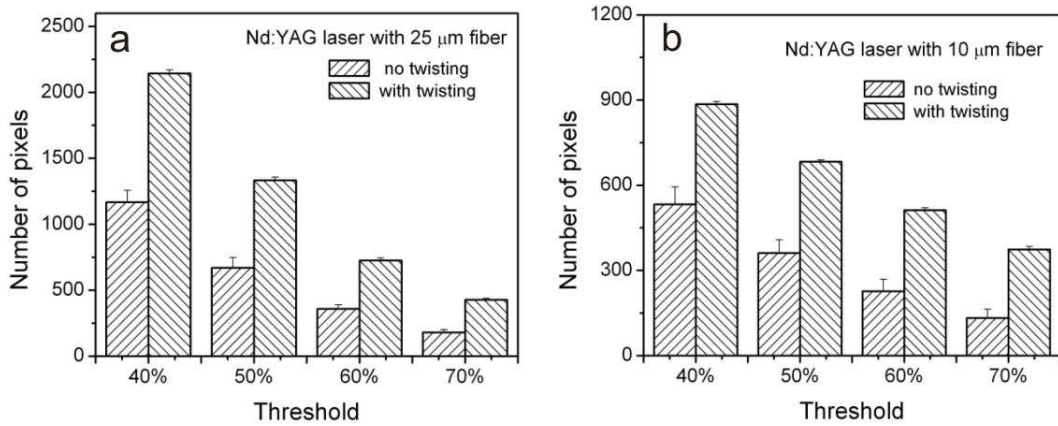
Figure 3.15: Comparison of the number of pixels with and without twisting the fibers for the Nd:YAG laser. (a) 25 μm fiber, (b) 10 μm fiber.

interference patterns between the modes by increasing the effective path differences between the modes beyond their coherence length [39]. A steady-state power distribution among the bound fiber modes occurs after an equilibrium length of the order of 1 km [38], although significant improvement in spatial uniformity occur at considerably shorter lengths. Fig.3.17a,b show the profiles for a 30-m long fiber with a 10-μm diameter core for both the N_2 and the Nd:YAG lasers. Some features are still observed, but the pattern is more uniform, and the differences between the lasers are largely absent. Fig.3.18 shows the integrated ion yield dependence on fluence for the Nd:YAG laser for the short fiber with and without twisting, and for the 30-m long fiber. The integrated ion yield for the N_2 laser are essentially the same for all three cases, so only the data for

Figure 3.16: Comparison of the number of pixels after twisting the fibers for the N_2 laser and the Nd:YAG laser with 10 μm fiber.

the short fiber (not twisted) are shown. The results are consistent with a simple measure of uniformity, as shown in Fig.3.19, where the number of pixels above 50% of maximum intensity is plotted for each case.

In summary the effects of twisting the fiber or using a longer fiber on the integrated ion yields are quite similar: in both cases, the differences between the N_2 and the Nd:YAG lasers are essentially eliminated. This suggests that the improved sensitivity observed using the N_2 laser compared with the Nd:YAG laser with the 2-m fiber is simply a result of a more complete (uniform) irradiation of the target area, and not due to the greater complexity of the pattern as previously suggested [28]. In MALDI imaging experiments where the beam is rastered across the sample continuously instead of irradiating discrete spots, an averaging effect similar to twisting the fiber is achieved.

3.4 Conclusions

In this chapter, the ion desorption properties of the N_2 laser and the Nd:YAG laser with fiber optics have been compared. The N_2 laser shows generally much higher ion sensitivity than the Nd:YAG laser for α-HCCA matrix with fiber optics, consistent with
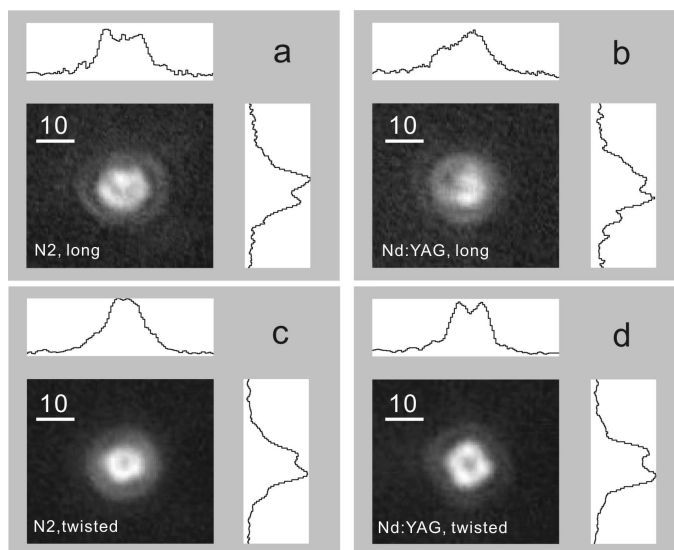
Figure 3.17: (a,b) Laser spot profiles obtained with the 30-m long fiber. (c,d) Superposition of multiple laser spot profiles acquired with 2-m long fiber, which was continuously twisted. The images on the left (a,c) were obtained with the N2 laser, while the images on the right (c,d) with the Nd:YAG laser. The fibers were all 10 μm in diameter. Both longer fibers and twisting during irradiation result in a more uniform,flat-top profile (time-averaged for the twisted fiber).
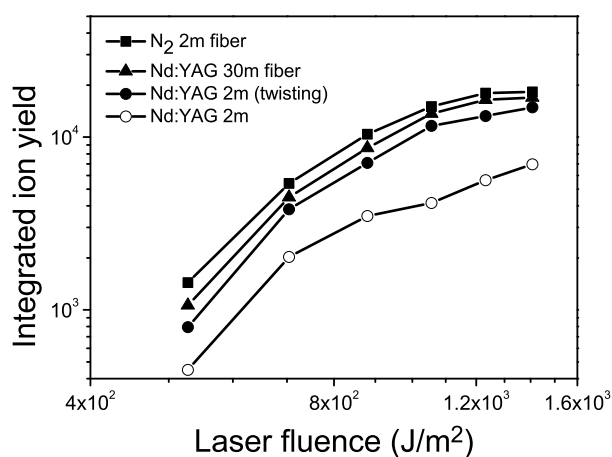
Figure 3.18: Comparison of the integrated ion yield dependence on fluence for the Nd:YAG laser for the 2-m long fiber with and without twisting, and for the 30-m long fiber without twisting. The integrated ion yields for the N2 laser are essentially the same for all three cases, so only the data for the 2-m long fiber (not twisted) are shown. The data were obtained for protonated substance p ions desorbed from α-HCCA.
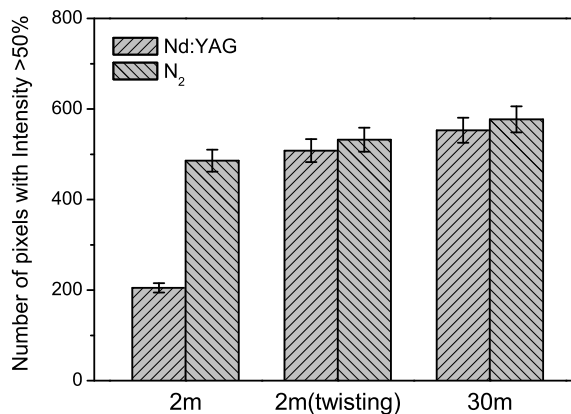
Figure 3.19: Comparison of the profile uniformity, represented by the number of pixels above 50% of maximum, for the N_2 laser and the Nd:YAG laser with a 2-m long fiber with and without twisting, and with a 30-m long fiber.

the observation of directly using lenses. The detailed laser beam profile study shows that the features of Nd:YAG laser are much sharper than N_2 laser. And the detailed study of the number of pixels also clearly shows that there are more pixels in the N_2 beam profile than the Nd:YAG laser, which seems to offer a consistent explanation for the better performance of the N_2. A more uniform beam profile obtained by twisting the fiber during irradiation or using a longer fiber greatly improves the sensitivity and essentially eliminates the differences between the N_2 and the Nd:YAG lasers. It may be concluded that the uniformity of the laser beam profile plays a more important role in the difference between the N_2 laser and Nd:YAG laser rather than the wavelength and pulse duration. This study also indicates that in MALDI imaging experiments where the beam is rastered across the sample continuously instead of irradiating discrete spots, an averaging effect similar to twisting the fiber is achieved.

References

[1] Karas, M.; Hillenkamp, F. *Anal. Chem.* **1988**, *60*, 2299–2301.

[2] Tanaka, K.; Waki, H.; Ido, Y.; Akita, S.; Yoshida, Y.; Yoshida, T. *Rapid. Commun. Mass Spectrom.* **1988**, *2*, 151.

[3] Beavis, R. C.; Chait, B. T.; Fales, H. *Rapid Commu. Mass Spectrum.* **1989**, *3*, 432.

[4] Strupat, K.; Karas, M.; Hillenkamp, F. *Int. J. Mass Spectrom. Ion Processes* **1991**, *111*, 89–102.

[5] Overberg, A.; Karas, M.; Bahr, U.; Kaufmannn, R.; Hillenkamp, F. *Rapid Commun. Mass Spectrom.* **1990**, *4*, 293–296.

[6] Berkenkamp, S.; Menzel, C.; Karas, M.; Hillenkamp, F. *Rapid Commun. Mass Spectrom.* **1997**, *1*, 1399–1406.

[7] Overberg, A.; Karas, M.; Hillenkamp, F. *Rapid Communications in Mass Spectrometry* **1991**, *5*, 128–131.

[8] Menzel, C.; Berkenkamp, S.; Hillenkamp, F. *Rapid Communications in Mass Spectrometry* **1999**, *13*, 26–32.

[9] Berkenkamp, S.; Kirpekar, F.; Hillenkamp, F. *Science* **1998**, *281*, 260–262.

[10] Ehring, H.; Karas, M.; Hillenkamp, F. *Org. Mass Spectrom.* **1992**, *27*, 472–480.

[11] Allwood, D. A.; Dreyfus, R. W.; Perera, I. K.; Dyer, P. E. *Rapid Commun. Mass Spectrom.* **1996**, *10*, 1575–1578.

[12] Horneffer, V.; Dreisewerd, K.; Ludemann, H. C.; Hillenkamp, F.; Lage, M.; Strupat, K. *Int. J. Mass Spectrom.* **1999**, *185*, 859–870.

[13] Niu, S.; Zhang, W.; Chait, B. T. *J. AM. Soc. Mass Spectrom.* **1998**, *9*, 1–7.

[14] Demirev, P.; Westman, A.; Reimann, C. T.; Hakansson, P.; Barofsky, D.; Sundqvist, B. U. R. *Rapid Commun. Mass Spectrom.* **1992**, *6*, 187–191.

[15] Dreisewerd, K.; Schurenberg, M.; Karas, M.; Hillenkamp, F. *Int. J. Mass Spetrom. Ion Processes* **1996**, *154*, 171–178.

[16] Zhigilei, L. V.; Garrison, B. J. *J. Appl. Phys.* **2000**, *88*, 1281–1298.

[17] Mowry, C. D.; Johnston, M. V. *Rapid Commun. Mass Spectrom.* **1993**, *7*, 569–575.

[18] Knochenmuss, R.; Stortelder, A.; Breuker, K.; Zenobi, R. *J. Mass Spectrom.* **2000**, *35*, 1237–1245.

[19] Westman, A.; Huth-Fehre, T.; Demirev, P.; Bielawski, J.; Medina, N.; Sundqvist, B. U. R. *Rapid Commun. Mass Spectrom.* **1994**, *8*, 388–393.

[20] Ingendoh, A.; Karas, M.; Hillenkamp, F.; Giessmann, U. *Int. J. Mass Spectrom. Ion Processes* **1994**, *131*, 345–354.

[21] Ens, W.; Mao, Y.; Mayer, F.; Standing, K. G. *Rapid Commun. Mass Spectrom.* **1991**, *5*, 117–123.

[22] Eckerskorn, C.; Strupat, K.; Karas, M.; Hillenkamp, F.; Lottspeich, F. *Electrophoresis* **1992**, *13*, 664.

[23] Strupat, K.; Karas, M.; Hillenkamp, F.; Eckerskorn, C.; Lottspeich, F. *Anal. Chem.* **1994**, *44*, 464.

[24] Dreisewerd, K.; Schurenberg, M.; Karas, M.; Hillenkamp, F. *Int. J. Mass Spectrom. Ion Processes* **1995**, *141*, 127–148.

[25] Westmacott, G.; Ens, W.; Hillenkamp, F.; Dreisewerd, K.; Schurenberg, M. *Int. J. Mass Spectrom.* **2002**, *221*, 67–81.

[26] Feldhaus, D.; Menzel, C.; Berkenkamp, S.; Hillenkamp, F.; Dreisewerd, K. *J. Mass Spectrom.* **2000**, *35*, 1320–1328.

[27] Qiao, H.; Spicer, V.; Ens, W. *Rapid Commun. Mass Spctrom.* **2008**, *22*, 2779–2790.

[28] Holle, A.; Haase, A.; Kayser, M.; Hohndorf, F. *J. Mass Spectrom.* **2006**, *41*, 705–716.

[29] Wenzel, R. J.; Prather, K. A. *Rapid Commun. Mass Spectrom.* **2004**, *18*, 1525–1533.

[30] Steele, P. T.; Srivastava, A.; Pitesky, M. E.; Fergenson, D. P.; Tobias, H. J.; Gard, E. E.; Frank, M. *Anal. Chem.* **2005**, *77*, 7448–7454.

[31] Bromirski, M.; Loboda, A.; Ens, W.; Standing, K. G.; In *Proceedings of the 48th ASMS conference on mass spectrometry and allied topics*, 2000.

[32] Caprioli, R. M.; Farmer, T. B.; Gile, J. *Anal. Chem.* **1997**, *69*, 4751–4760.

[33] Stoeckli, M.; Farmer, T. B.; Caprioli, R. M. *J. Am. Soc. Mass Spectrom.* **1999**, *10*, 67–71.

[34] McDonnell, L. A.; Heeren, R. M. A. *Mass spectrom. rev.* **2007**, *26*, 606–643.

[35] Kozlovski, V. I.; Loboda, A. V.; Spicer, V.; McNabb, J. R.; Ens, W.; Standing, K. G.; In *Proceedings of the 50th ASMS conference on mass spectrometry and allied topics*, 2002.

[36] Vorm, O.; Roepstorff, P.; Mann, M. *Anal. Chem.* **1994**, *66*, 3281–3287.

[37] Mickelson, A. R. *Guided Wave Optics*; Van Nostrand Reinhold: New York, 1993.

[38] Snyder, A. W.; Love, J. D. *Optical waveguide theory*: London: Chapman and Hall, 1983.

[39] Buettner, L.; Czarske, J. *Meas. Sci. Technol.* **2001**, *12*, 1891.

Chapter 4

The effect of laser fluence and spot size on sensitivity in orthogonal-injection MALDI TOF mass spectrometry

4.1 Introduction

MALDI tissue imaging mass spectrometry has attracted much recent interest [1–3]. Most of the development work has been with axial MALDI TOF instruments [1, 4, 5], but in the past few years, a number of other instruments have been used with more decoupled ion sources [6–8].

In an axial MALDI instrument, the degrees of freedom for optimizing the laser exposure conditions are constrained to some extent by the performance of the instrument. In general, performance is optimum when the fluence is kept near the practical threshold, i.e. the minimum fluence for which transients appear significantly above the noise. The introduction of delayed extraction [9, 10] has made the fluence much less critical, but performance is still weakly dependent on fluence and, in particular, it remains important that the fluence (or signal strength) remains reasonably constant throughout an experiment.

In instruments with decoupled MALDI sources, such as orthogonal-injection TOF instru-

ments, or MALDI ion traps, the mass accuracy and mass resolution are not affected by the laser fluence or the plume density. The mass spectrum of course depends on differential fragmentation and instrument transmission, but these parameters also seem to be fairly insensitive to laser fluence [11].

In this chapter, we examine the effect of the laser fluence and spot size on sensitivity, a critical figure-of-merit in MALDI imaging. A useful measure of sensitivity is the total number of ions that can be detected from a given sample area, by irradiating until the signal is completely exhausted. Reducing the spot size has obvious advantages for improved spatial resolution, and different instrumental designs have been reported to achieve reduced laser spot size [5, 12], or stigmatic focusing [13]. However, at present, spatial resolution in MALDI imaging is limited mainly by sample preparation [14, 15], so these experiments are focused on the question of sensitivity, which determines the range of protein abundance that is amenable to imaging experiments. The effects of fluence and spot size also have implications important for understanding the fundamentals of laser desorption, and for data rate,another important figure of merit in imaging.

Several experiments have reported ion yield measurements as a function of laser fluence and, to a lesser extent, as a function of the laser spot size [16–22]. In these studies, the ion yield refers to the number ions desorbed per laser pulse. The results show a steep power law increase followed by saturation of the yield at higher fluence. These results have been mainly interpreted in the context of the ion desorption process, and have not been used, at least explicitly, to optimize the experiments for best sensitivity. In fact, the connection between yield per shot and sensitivity, has not been directly expressed. The usual assumption appears to be that sensitivity is not strongly dependent on fluence; i.e. that lower yields can be compensated by more laser shots. However, integrated sensitivity depends on the charge-to-neutral ratios of the desorbed ions, and on the desorption/damage ratios, both of which may depend on the laser fluence. In fact, after the signal from a given sample spot is depleted at low fluence, it can usually be at least partially restored by irradiating briefly at higher fluence [23]. Thus, when operating MALDI in a manual mode, better sensitivity can be achieved on an axial

TOF instrument operating at low fluence if high fluence irradiation is occasionally used. This kind of tailoring of the fluence could be applied in MALDI imaging, but is more difficult to automate, and to our knowledge such attempts have not been reported. The question of how total sensitivity depends on fluence (held constant for the duration of one measurement) has not been adequately addressed.

Measurements of yield and threshold fluence as a function of spot size have indicated a cubic dependence on area [20, 21] and have given the impression that larger spot sizes therefore provide better sensitivity [3, 24]. However, such analysis does not take account of saturation fluence (higher for smaller spot sizes), and does not consider the integrated sensitivity at all.

In the previous laser fluence and spot size measurements, a variable telescope optical setup had been used to achieve different beam spot sizes ranging from 10 to 280 μm [16]. In this experiment the laser beam were all with Gaussian profiles. Another experimental setup used a 200-μm optical fiber to generate a flat-top laser beam profile. Different size pinholes were placed directly at the end of the fiber to produce different size spots which were imaged onto the target [20, 22]. One limitation with this setup is that the laser fluence range is limited because only a small fraction of the total laser energy was taken through the pinhole. This can be avoided in our experiment by focusing the laser energy onto different size fibers, giving a much broader laser fluence range for study.

From the laser beam profile studies in the last chapter, we found that uniform beam profile improved the sensitivity. In fact, the uniform irradiation can also simplify the interpretation of fluence dependence compared to that of a Gaussian profile. The comparison of ion sensitivity between the N_2 laser and the Nd:YAG laser also show that, although the beam profiles are not perfectly flat-top, all the profiles from the N_2 laser and those from the Nd:YAG laser with long or twisted fiber are uniform enough that further improvement does not affect the yield or the yield vs. fluence dependence. For this reason, the detailed measurements in this chapter were all performed with the N_2 laser using 2-m optical fiber patch cords. It is less practical to use 30-m (or longer) fibers for all the diameters, since

the long patch cords are expensive, and bare fibers make the alignment and fiber swapping much more difficult. Moreover, the losses in the long fibers reduce the range of accessible fluence, and, in some experiments, the saturation fluence was already out of range.

In this chapter, a series of fibers of 10, 25, 50, 100, and 200μm in diameter were used to study the influence of laser fluence and spot size on ion yield and sensitivity with N_2 laser. For each fiber, different laser fluences were used. The dependence of ion yield and sensitivity on laser fluence were studied. Then the spot size dependence was discussed at different laser fluence regimes. Different matrices and molecular ions were also examined for the fluence and spot size dependence. Scanning modes correlated to the spot size dependence in MALDI imaging were discussed for better sensitivity and spatial resolution.
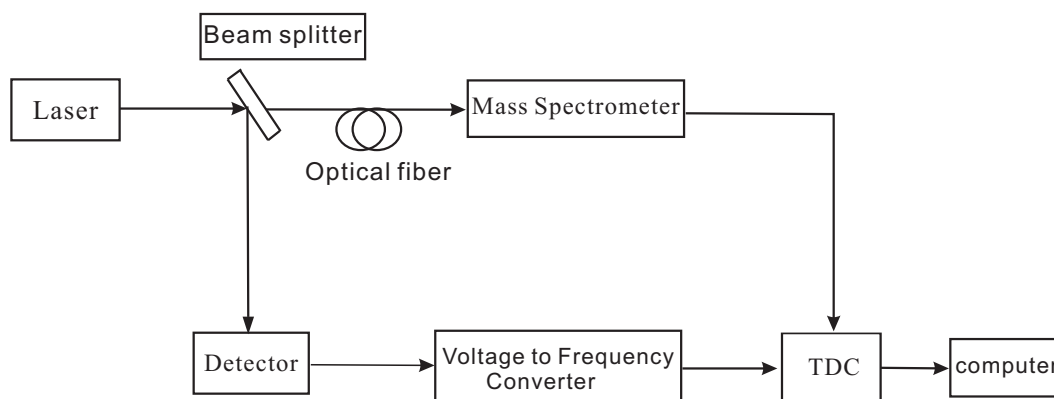
4.2 Experimental

4.2.1 Instrumentation

All the fluence and spot-size dependence measurements were made with a Manitoba-Sciex prototype orthogonal-injection QqOF instrument [25], with a 30° incident laser angle, illustrated schematically in Fig.4.1. Some of the fluence and spot-size measurements were repeated on a commercial PE-Sciex proTOF instrument (Perkin Elmer, Waltham MA, USA), with the same laser angle [26]. All the other parameters related to the orthogonal-injection TOF mass spectrometer are similar to those described in Chapter 3.

The same N_2 laser was used as the one used for laser beam profile study in Chapter 3. A J3 pyroelectric joulemeter (Molectron Detector Inc, Portland, Oregon.) was used to measure the pulse energy. To estimate the absolute fluence, the energy was measured at the end of the fiber using the calibration supplied with the joulemeter, and the fluence was then calculated based on the size of the burn marks which is also the same as the burn mark shown in Chapter 3, without correcting for losses due to the focusing optics and the entrance window. The absolute fluence values should therefore be regarded as
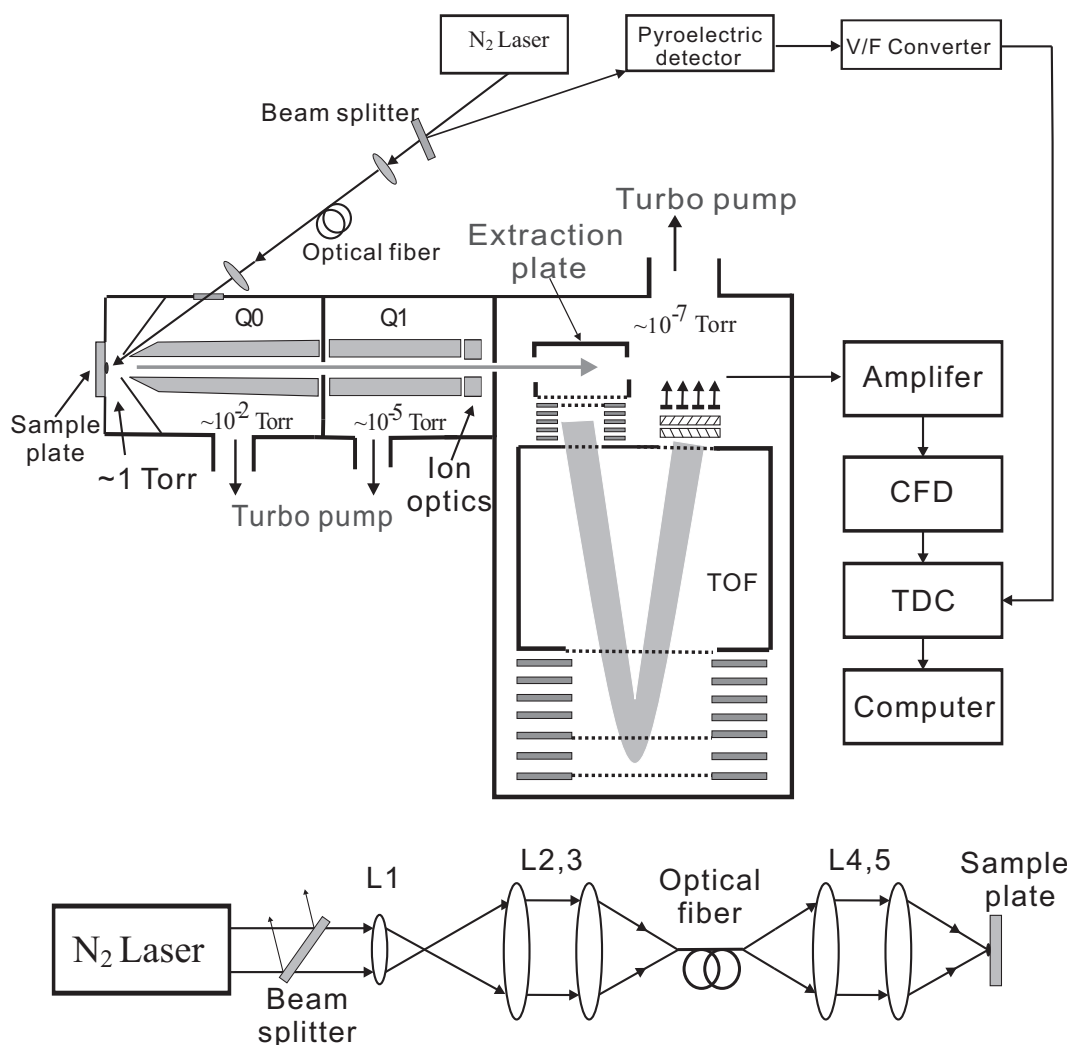
Figure 4.1: Schematic diagram of an orthogonal MALDI TOF mass spectrometer, the optics, and the data collection arrangement. The laser beam was focused into the fiber by three lenses. L1: f = 5 mm, L2,3: f2 = f3 = 10 cm. The fiber output was imaged onto the sample plate by two aspherical lenses L4,5: f4 = f5 = 10 cm. The collision cell Q3 in one of the instruments [25] was operated in RF-only mode, and is not shown in the figure. About 10% of the laser energy is reflected by the beam splitter and detected by a pyroelectric detector. The fluctuation of the laser pulse energy is monitored by the voltage-to-frequency converter and recorded by the TDC for every laser shot.(To estimate fluence, the pulse energy was measured after the fiber, as described in the text.)

Figure 4.2: The block diagram of the experimental setup.

approximations, probably somewhat higher than the actual values.

However, the relative values relevant to these experiments were carefully monitored, by measuring the energy of each laser pulse using a beam splitter before the optical fiber. The output of the joulemeter was used to drive a home-built voltage-to-frequency converter giving a train of NIM pulses (Nuclear Instrument Module, -800 mV) at a frequency proportional to the laser shot energy. This signal was coupled into one of the TDC (time to digital converter) input channels, allowing us to record laser energy and the corresponding MALDI mass spectrum simultaneously. All incoming time-of-flight data was 'spooled' into a large RAM file, allowing us to re-analyze the complete experiment as a function of elapsed experiment time. These spools were then pre-processed using custom Perl code; detailed statistical analysis was performed using MatLab (The Mathworks Inc., Natick, MA, USA) on the resulting files. Only the data within the laser energy fluctuation window($\pm$ 5%) were selected. The experimental block diagram is shown in Fig.4.2.

4.2.2 Sample preparation

All the samples were purchased from Sigma-Aldrich Company. Samples were used as supplied commercially without further purification. The samples were prepared with matrices 4 - hydroxy - α - cyanocinnamic acid (α-HCCA), trans -3,5-dimethoxy - 4 -hydroxy - cinnamic acid (sinapinic), and 2,5 - dihydroxybenzonic acid (2,5-DHB). The analytes

used were substance P (1347 Da), mellitin (2847 Da), insulin (5734 Da), cytochrome C (12,327 kDa), myoglobin (16,951 kDa), and trypsin (23,460 kDa). The samples were also prepared using thin layer sample preparation method [27]. The sample preparation procedure is the same as described in Chapter 3.

For the detection limitation experiment, small sample droplets were deposited using a capillary 10 μm in diameter. The flow rate of syringe pump was set as slow as about $\sim$0.3 μL/hour. By counting the flow time, the total amount of sample deposited on the target can be determined.

4.3 Design of voltage-to-frequency converter

As described in the experimental section, the absolute laser pulse energy can be measured at the end of the fiber. When studying the influence of laser fluence on the ion yield per laser shot in MALDI, it is very important to carefully monitor the fluctuation of the laser pulse energy. Both Fig.4.1 and Fig.4.2 show that a small portion of the laser pulse energy (about 10%) is reflected by a beam splitter and recorded by a joulemeter as a detector. The output of the joulemeter is then processed by a home-made voltage-to-frequency converter circuit and recorded by one of the TDC channels. Only the mass spectral data desorbed by laser pulses with energy between $\pm$5% of the mean are selected for analysis. This can improve the accuracy of the measurements. In this section, the design of the voltage-to-frequency converter circuit will be given in detail.

4.3.1 The working principle

The working principle of the voltage-to-frequency circuit is shown in Fig.4.3a as a block diagram and in Fig.4.3b as a detailed schematic diagram. Just as shown in Fig.4.2, the laser pulse energy is split into two parts by the beam splitter, so that about 10% of the laser beam energy is reflected and recorded by a joulemeter detector. Because the

amplitude of the output pulse from the detector is relatively low, it has to be amplified using an operational amplifier (CA3140). The amplified signal is then divided and fed into two branches of circuits, named 'Branch 1' and 'Branch 2' in the circuit diagram.

In Branch 1, the first component is a sample-and-hold circuit. Its output is an approximate square pulse with amplitude corresponding to that of the input pulse. The output pulse width of the sample-and-hold circuit is about 10 ms and decays exponentially. To use only the flat portion of the pulse for conversion to frequency, the output pulse of the sample-and-hold circuit is gated by a pulse from Branch 2. The output pulse is then fed into a voltage-to-frequency converter module, which converts the laser pulse amplitude into a train of TTL pulses (Transistor-transistor logic, 800mV). The frequency of this pulse train is proportional to the laser pulse energy. This TTL pulse train can be easily converted into a train of negative timing pulses by connecting a 100pF capacitor. Finally the pulse train is recorded by one of the TDC channels. The pulse gate mentioned above serves to limit the length of this pulse train to less than the extraction period, so it appears after only one extraction pulse (see below).

Branch 2 is designed to generate the gate pulse with a defined pulse width which is synchronized with the signal in Branch 1. This gate pulse will control the time period of the TTL pulse train in Branch 1. Branch 2 basically consists of another amplifier and a 555 timer. The 555 timer will generate the pulse gate using the rising edge of the input pulse. It has nothing to do with the pulse amplitude. The output pulse width of the 555 timer can be easily tuned by adjusting the corresponding resistor and capacitor in the circuit. The output of the 555 timer is then inverted to control a MOSFET switch. This switch is connected to both ground and the input of the voltage-to-frequency converter module in Branch 1. So the input pulse width of the voltage-to-frequency converter module will be controlled by the output pulse width of the 555 timer. With these two branches, a train of NIM pulses with a defined time period entraining the laser pulse energy information will be recorded by the TDC.
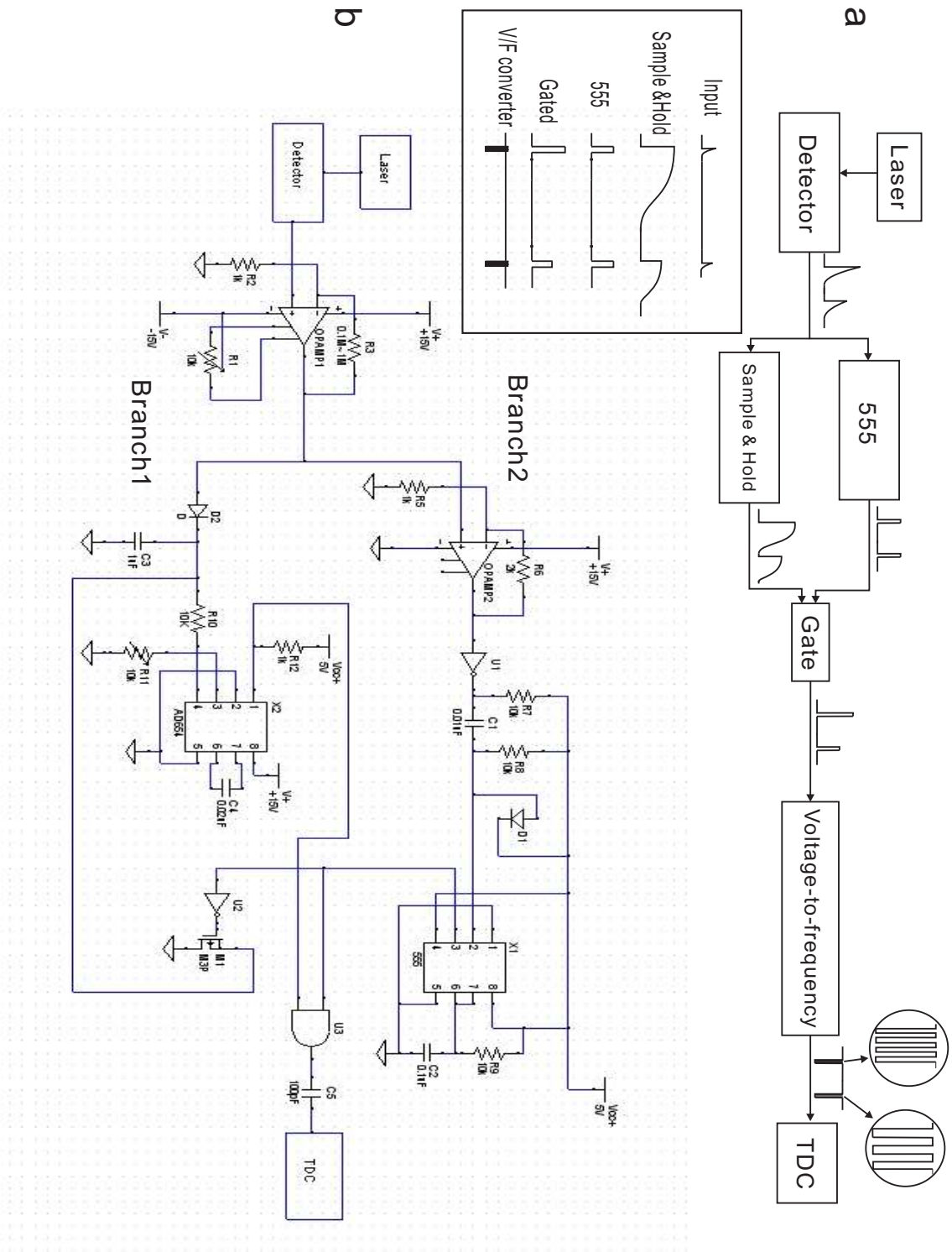
Figure 4.3: The block diagram and the detailed schematic diagram of the laser pulse energy recording circuit
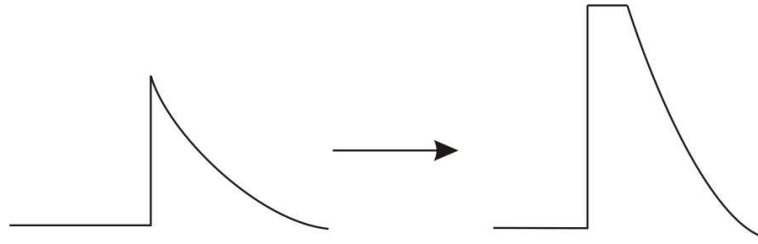
Figure 4.4: Pulse saturation due to the over-amplification of Amplifier 1. In this case, the fluctuation of laser pulse energy will be lost.

4.3.2 Electronic components

1. Operational amplifier 1

This amplifier is a CA3140. It has high input impedance, low input current, and high speed performance. The amplification is determined by the ratio of resistance between R3 and R2 shown in Fig.4.3. R3 is a potentiometer that gives the flexibility of changing the amplification for the input signal. The input offset voltage is nulled by connecting a 10 kΩ resistor. The power supply voltage is 15 V, which limits the maximum amplitude of the output at 15 V. The amplification should therefore be adjusted carefully to keep the output voltage lower than 15 V. Otherwise it may result in a saturation of the output shown in Fig.4.4. In this case, the fluctuation information of the laser pulse energy will be lost.

2. Sample-and-hold circuit

This circuit simply consists of a diode and a capacitor. The diode is used to prevent the capacitor from discharging. The capacitor is quickly charged and holds the amplitude of the input signal. Ideally the output should be a perfectly straight line which is proportional to the amplitude of the input pulse. In fact, the capacitor still discharges gradually with a discharge period about 10 ms. In order to precisely record the amplitude of the input pulse, only the front-most portion of this decayed curve about 300 μs is taken to represent the laser pulse energy, shown in Fig.4.5. Then it can be safely used to represent the amplitude of the input pulse. This pulse width is controlled by the 555 timer and the
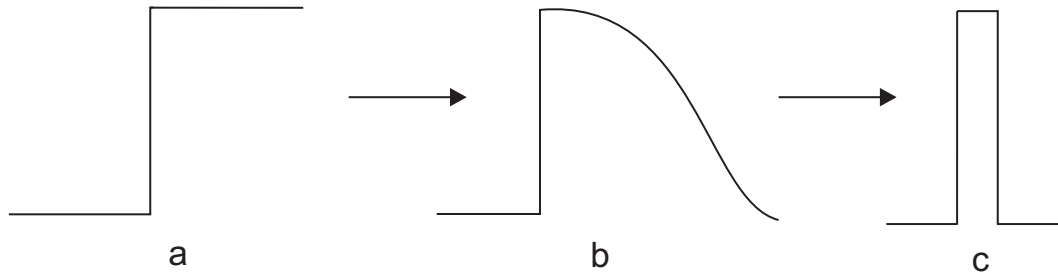
Figure 4.5: The output pulse of the sample-and-hold circuit in the ideal output (a) and the experimental output (b). The experimental output pulse with pulse width gated ($\sim 300~\mu$s) is shown in (c)

MOSFET switch.

3. 555 timer

The output pulses from the joulemeter detector are amplified through OpAmp1 and OpAmp2 before they are fed into the 555 timer. In principle the 555 timer can only be triggered by the falling edge of the input pulse. However in our experiment the input pulse is positive and the only useful information is its rising edge which corresponds the start of the laser pulse. This rising edge has to be inverted to a falling edge in order to trigger the 555 timer, so an NAND gate is then used after the OpAmp2. The output pulse width of OpAmp2 is about 10 ms. When this pulse is inverted, the negative pulse width is also about 10 ms. According to the working principle of the 555 timer for monostable output, the output stays high when the input is low, so the minimum pulse width of the output of 555 timer will be about 10 ms no matter what we tune the RC timing constant.

In order to reduce the output pulse width of the 555 timer, a trigger network is then used after the NAND shown in Fig.4.6. It can detect the falling edge of the input pulse and produce a short negative spike ($\sim$50 μs) which will trigger the 555 timer at an appropriate time. The monostable pulse can be adjusted to be about 300 μs by tuning the resistor R9 and capacitor C2. The monostable output of 555 timer will be inverted by a NAND and then used to control the MOSFET switch. Only when the monostable output is high, the sample-and-hold circuit will generate a pulse with a defined pulse width from 555 timer.
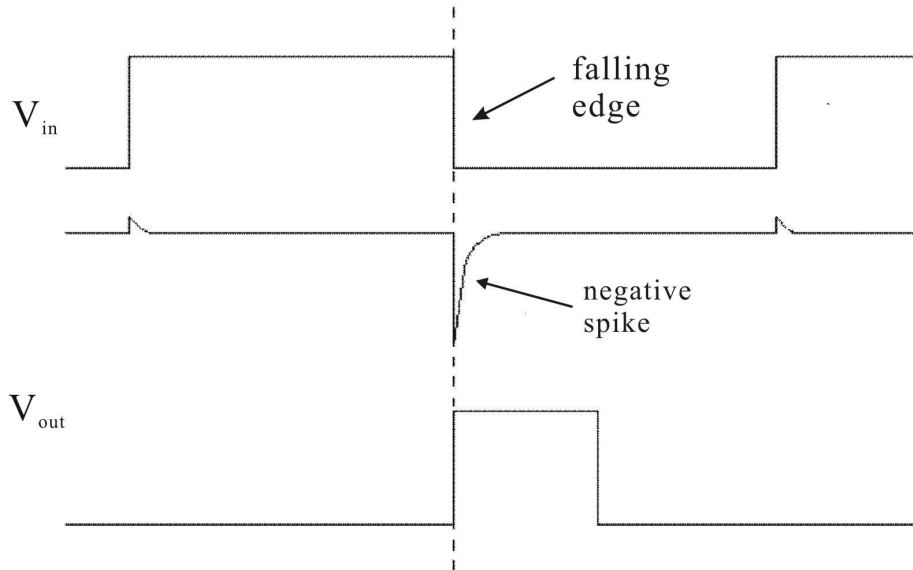
Figure 4.6: A short negative pulse is generated by a trigger network. This provides the possibility of controlling the output pulse width of the monostable with a much wider range from 50 μs to 1 ms.

There are two reasons for gating the input pulse width for the voltage-to-frequency converter module: First, as mentioned, only the front-most portion of the sample-and-hold output is approximately constant. Second, the pulse width must be shorter than the time between ion extraction pulses, which correspond to start pulse for the TDC. Since there is no synchronization between the laser pulse and the extraction pulse, if the input pulse width of the voltage-to-frequency converter is longer than the duration between two extraction pulses of the mass spectrometer, the negative timing pulse train from the voltage-to-frequency circuit will be recorded after at least two extraction pulses and will therefore produce multiple peaks at almost random positions in a summed spectrum shown in Fig.4.7. Therefore the input pulse width of the voltage-to-frequency converter module must be shorter than the extraction pulse duration of the mass spectrometer.

For example, normally the extraction frequency of the TOF mass spectrometer is set about 7500 Hz. The pulse duration of the extraction pulses is about 133 μs. When a 300 μs negative timing pulse train is fed into the TDC, it will be registered by at least two extraction pulses. The negative timing pulses registered from these two extraction pulses
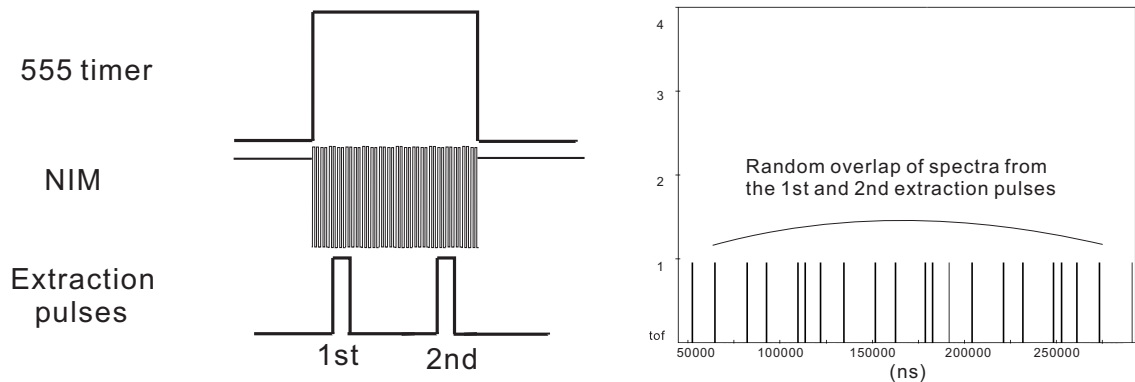
Figure 4.7: Output pulse duration of the negative timing pulse train is longer than the extraction frequency of mass spectrometer. The unsynchronization between the extraction pulses and the negative timing pulse pulses results in a random add-up for the laser energy spectrum.

will be added up randomly shown in Fig.4.7. In order to keep enough pulses within the duration for better statistics of calculating the negative timing pulse frequency, we reduce the extraction frequency to about 3000 Hz (333μs) and keep the duration of the negative timing pulses about 300 μs.

The unsynchronization between the laser pulse and the extraction pulse results in two different situations of the recorded spectrum for the laser pulse energy, which depends on the relative positions of the extraction pulses with respect to the negative timing pulses.

1. If the negative timing pulses fall exactly in between two extraction pulses, shown in Fig.4.8, all the negative timing pulses will be recorded after the first extraction pulse. The second extraction pulse records nothing because there is no any event happened after it. This will give the maximum pulse amplitude of the 'laser energy peaks'.

2. If the negative timing pulses partially fall after the first and the second extraction pulses, they will be recorded by these two extraction pulses. The relative position between the extraction pulse and the negative timing pulses determines their positions recorded in the spectrum. This is shown in Fig.4.9. In the spectrum the front portion of negative timing pulses is recorded from the second extraction pulse and the rear portion of negative timing pulses is recorded from the first extraction pulse.
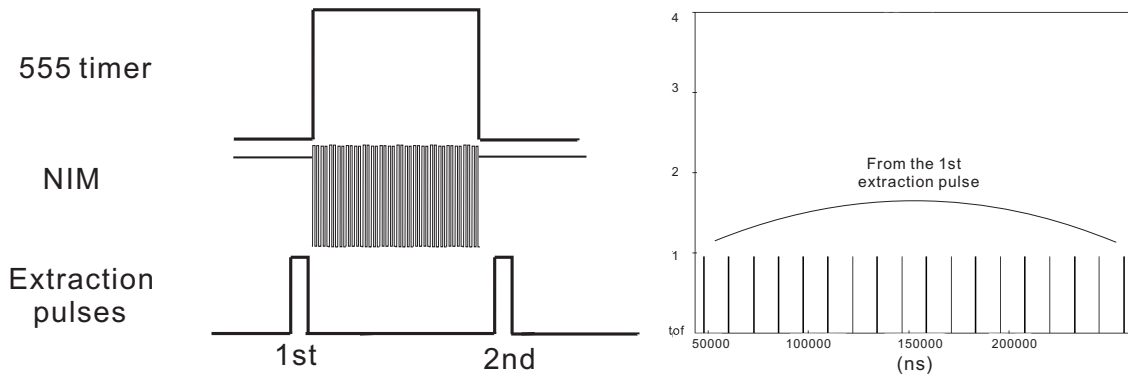
Figure 4.8: The negative timing pulses fall exactly between two extraction pulses. The spectrum is recorded only by the first extraction pulse. The second extraction pulse record nothing.
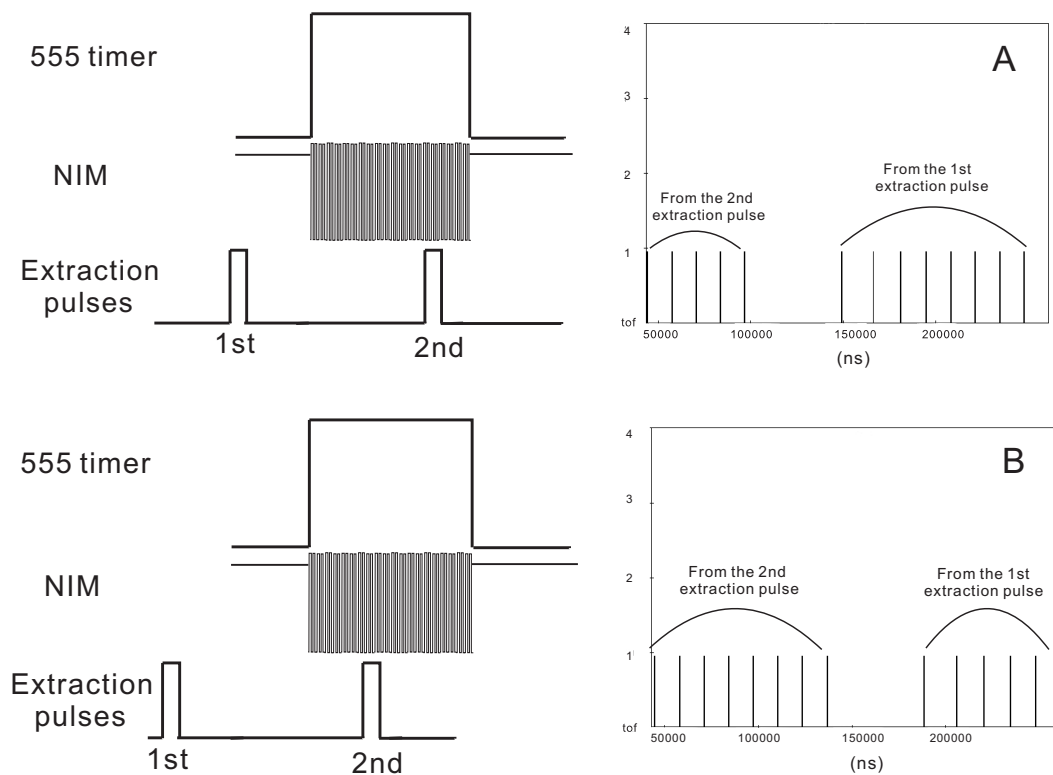
Figure 4.9: The negative timing pulses fall partially in each of two extraction pulses. In this case, the relative position with respect to the extraction pulses (start signal) determines the relative position of the negative timing pulses in the recorded spectrum. (A) most of the negative timing pulses are recorded by the first extraction pulse (B) most of the negative timing pulses are recorded by the second extraction pulse.
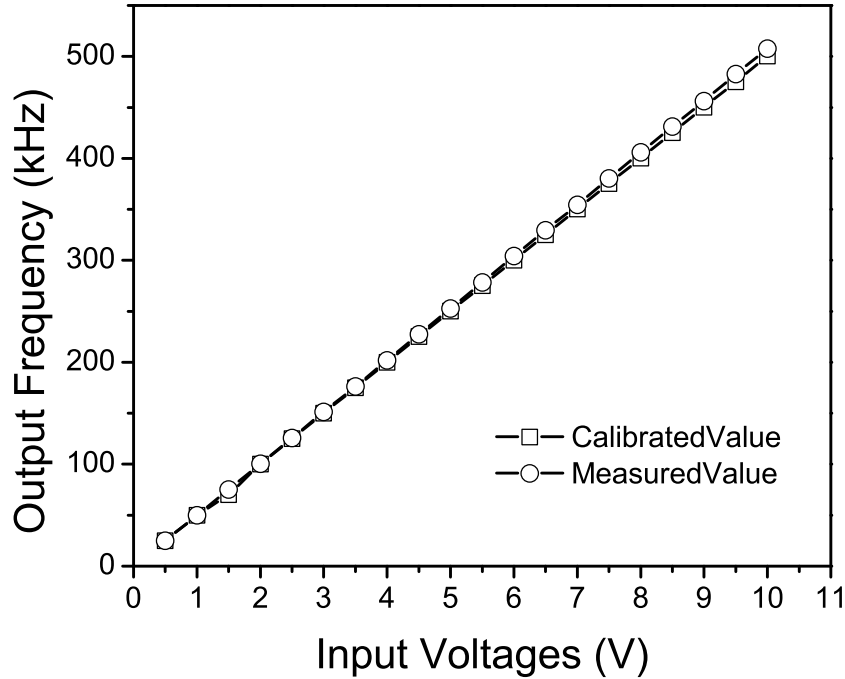
4. Voltage to frequency converter module

The voltage to frequency converter module is a AD654. The full-scale output frequency is determined by the timing network of R11 and C4 shown in Fig.4.3. It can be calculated by equ.(4.1)

$$f = \frac{V}{10RC} \qquad (4.1)$$

where V is the full scale input voltage. By setting the resistor R11 as 10 kΩ and the capacitor C4 as $0.02\mu F$, the input voltage ranges from 0 to 10 V and the full scale output frequency is then set as 500 kHz. Thus 1 V input will produce pulses with frequency of 50 kHz, which is called the frequency constant. The output is TTL pulses, whose frequency is proportional to the amplitude of the input pulses. The pulse duration of the TTL pluses is controlled by the output of the 555 timer. Once the frequency constant is set for this circuit, the linearity of the circuit has been checked for the full scale input voltage from 0 to 10V. The graph is shown in Fig.4.10. In this graph, the ideal curve is plotted theoretically based on the calculated frequency constant. The measured curve is plotted by measuring the output frequency for each input voltage. As can be seen from this curve, the linearity becomes worse as the increasing of the input voltage. According to the calculation, the nonlinearity is less than 1% when the input voltage is less than 6 volts. At 10 volts, the nonlinearity goes up to about 1.5%. So in order to reduce the nonlinearity of the circuit, the amplification of OpAmp1 is tuned to keep the input voltage below 6 V.

4.3.3 Data analysis

As described, the laser pulse energy information is recorded in the data spool through one of TDC channels, so it can extracted during the analysis. Fig.4.11 shows an example of

Figure 4.10: The comparison of the linearity of the voltage-to-frequency converter between the ideal and the practical measurements.

the full recorded spool file. The large 'ion peak' show the ion count distribution for each laser shot in which the number of ions detected is plotted as a function of the elapsed time. Fig.4.12 is an example of the mass spectrum generated from one of these ion peaks, where the measured TOF from the TDC is histogrammed from all extraction pulses within the related elapsed time window. The total mass spectrum can be generated by adding up all the mass spectra from these ion peaks. The narrow peaks in front of those ion peaks come from the negative timing pulses produced from the voltage-to-frequency converter, containing the laser pulse energy information labeled 'laser energy peaks'. These peaks are synchronized with the laser shots. The time difference between the laser energy peaks and the ion peaks is about 2 ms, which corresponds to the ion transmission time from its generation to its detection.

The laser pulse energy information can be extracted by analyzing the details of the 'laser
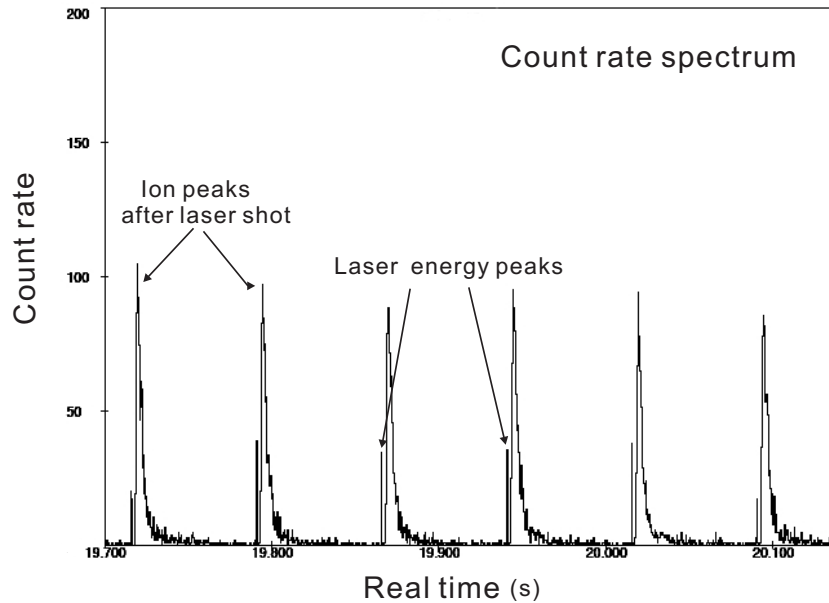
Figure 4.11: The recorded count rate as a function of elapsed time containing the ion peaks after each laser shot and the corresponding laser pulse energy peaks.

energy peaks'. The laser energy pulses can be isolated by selecting only one TDC channel, as shown in Fig.4.13a, where the pulse separation corresponds to the laser repetition frequency. To determine the laser pulse energy, we generate a 'TOF' spectrum from each laser energy peak and extract the frequency of the voltage-to-frequency converter. Using the frequency constant of the voltage-to-frequency converter circuit, the laser pulse energy can be calculated. It should be mentioned that the amplitude of the 'laser energy peaks' corresponds to the number of negative timing pulses recorded, but this is not always proportional to the laser pulse energy because the laser pulse and the extraction pulse are not synchronized (see above). The only useful information is the frequency of the negative timing pulses, which is directly correlated to the laser pulse energy.

4.3.4 Laser pulse energy distribution measurement

Because of the steep dependence of ion yield on laser fluence (power law dependence with powers ranging from 4 to 10) [17, 20, 21], significant fluctuation of laser pulse energy can strongly affect ion yield measurement. For example, assuming the power of the ion yield
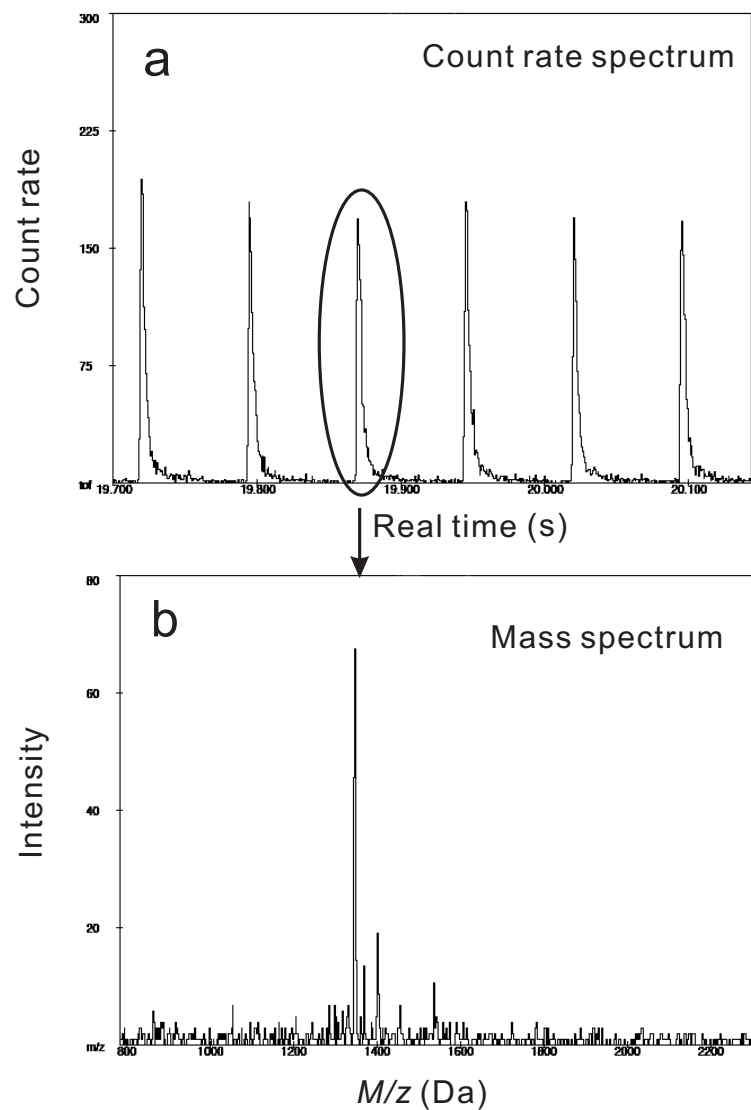
Figure 4.12: An example of showing the generation of mass spectrum from the recorded ion peaks. (a) ion peaks corresponding to each laser shot (b) mass spectrum generated from the ion peak.
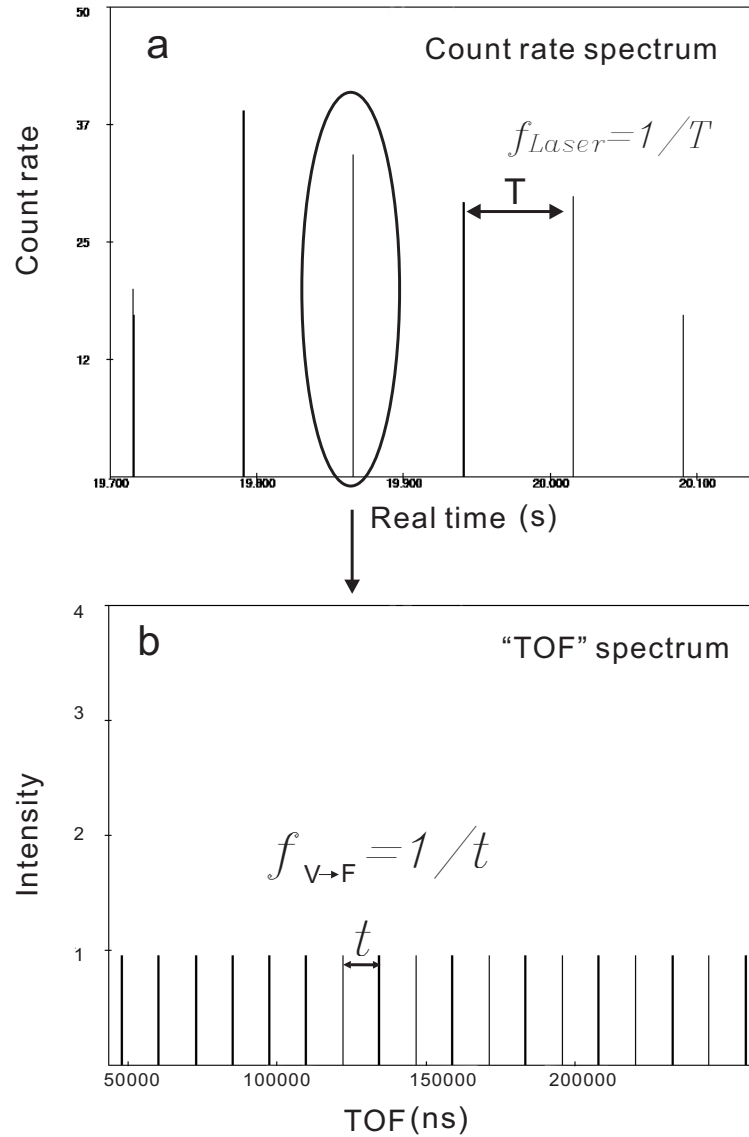
Figure 4.13: An example showing the generation of the 'TOF' spectrum from the recorded 'laser energy peaks'. This 'TOF' spectrum shows the recorded negative timing pulses generated from the voltage-to-frequency converter. (a) the recorded 'laser energy peaks' where the pulse separation is equal to the laser frequency, (b)the generated 'TOF' spectrum from one 'laser energy peak'. The pulse frequency is proportional to the laser pulse energy.

dependence on fluence is 7, i.e. $y = F^7$, if there is a $\pm 5\%$ fluctuation of laser fluence, then ion yields can be calculated as follows:

$$y_+ = [F(1 + 0.05)]^7 = F^7(1.4) \tag{4.2}$$

$$y_- = [F(1 - 0.05)]^7 = F^7(0.69) \tag{4.3}$$

The ion yield variations are approximately $(y_+ - y)/y = 40\%$ and $(y - y_-)/y = 30\%$. It will become more severe if the laser pulse energy fluctuation is larger than $\pm 5\%$. Therefore we have chosen to use those data with laser pulse energy between $\pm 5\%$ of the mean for analysis.

By analyzing the 'TOF' spectrum of the laser pulse energy, the average frequency of the negative timing pulse train was calculated and converted into the laser pulse energy according to the frequency constant of the voltage-to-frequency converter. The laser pulse energy distribution was studied for about 1000 laser pulses shown in Fig.4.14. The $\pm 5\%$ energy range used for analysis is labeled on the graph. And the $\pm 10\%$ is also labeled just for a comparison. It clearly shows that the laser pulse energy fluctuation is even larger than $\pm 10\%$ for some laser pulses. It is therefore necessary to monitor the fluctuation of laser pulse energy with a voltage-to-frequency converter. The reliability of the voltage-to-frequency converter for the measurement of laser pulse energy distribution was also verified with a multichannel pulse analyzer. Consistent measurement was obtained.

4.4 Results and Discussion

From the study of the influence of laser beam profile on the ion desorption/ionization of the N_2 laser and the Nd:YAG laser in last chapter, it shows that the N_2 laser gives much better performance than the Nd:YAG laser due to the uniform laser beam profile. Their desorption performance becomes almost equal with similar beam profile. In this
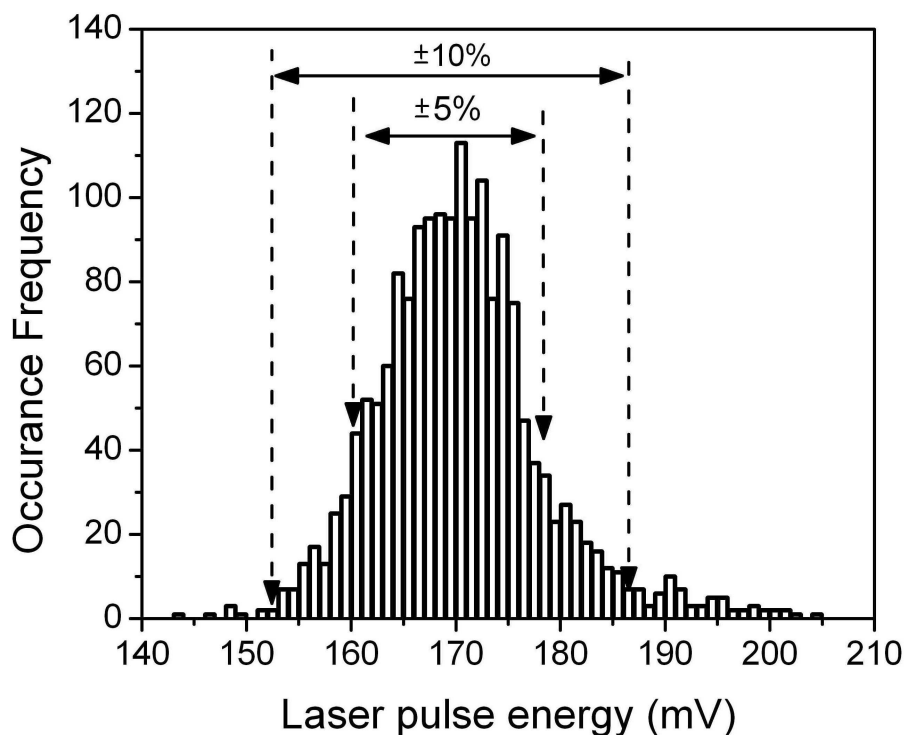
Figure 4.14: Measurement of the laser pulse energy distribution with the voltage-to-frequency converter for about 1000 laser pulses. It is a typical Gaussian distribution. The $\pm 5\%$ energy range used for analysis is labeled.

chapter, the measurements were made only by the N_2 laser with 2-m long fibers. In order to comprehensively study the influence of laser fluence and spot size on the ion desorption/ionization properties of the N_2 laser, the fibers ranging from 10, 25, 50, 100, and 200 μm in diameter were used. For each of five fibers and for a series of laser fluences values, the ion yield for protonated substance P desorbed from α-HCCA were measured and recorded from every laser pulse until the signal was exhausted. The ion yield was obtained by integrating the spectrum to include all the isotopes of the $[M+H]^+$ peak. The fluence was also monitored and recorded to ensure that it did not fluctuate by more than $\pm 5\%$ during the experiment.

First we studied the irradiation dependence of the ion yield per laser shot from single sample spots which were irradiated up to hundreds of laser shots (typically after 500 shots or less). The raw data for the 200 μm fiber are shown in Fig.4.15. Fig.4.15A shows that the ion yield per laser shot increases for the first few laser shots to the maximum and
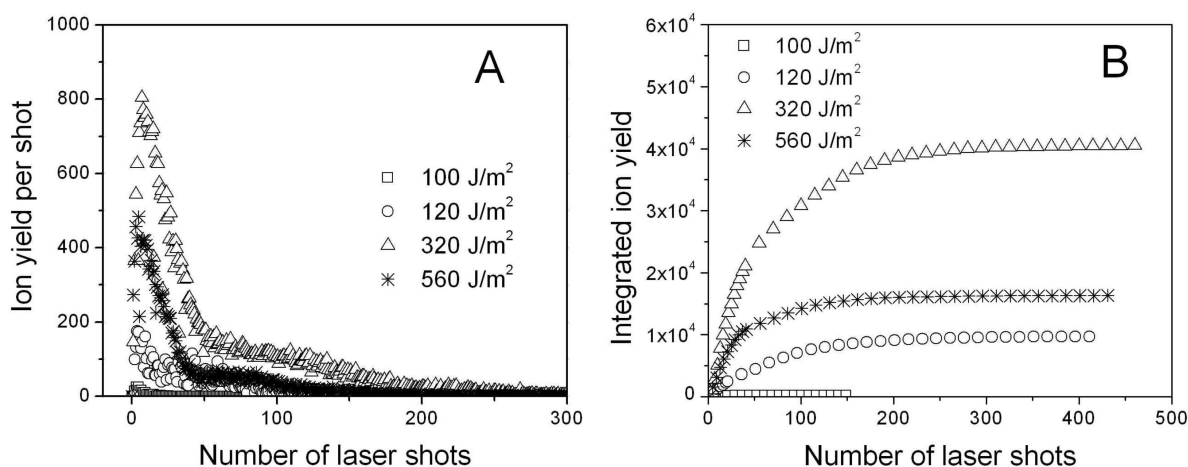
Figure 4.15: Dependence of (A) the ion yield per shot, and (B) the integrated ion yield on sample irradiation for different fluence values. The data were obtained for molecular ions of substance P desorbed from α-HCCA with the N2 laser and a 2-m long 200 μm fiber.

then decays to near zero over the next several hundred shots for each laser fluence. The decay of the signal is quite similar for different fluence values, indicating that the fluence that produces the maximum yield per shot also produces the maximum integrated yield. Fig.4.15B shows the variation of the integrated yield as a function of laser shots. It is clear that the integrated yield increases much faster for the first about 100 laser shots, then it reaches to saturation which corresponds to the zero ion yield per shot. The saturation of integrated yield may come from two situations: at the higher fluence, the saturation of the integrated ion yield corresponds to visible depletion of the sample on the surface, but, at lower fluence, this is clearly not the case; presumably some kind of surface modification inhibits futher desorption [23, 28, 29]. As mentioned in the introduction, after the signal decays at low fluence, it can usually be at least partially restored by brief irradiation at higher fluence.
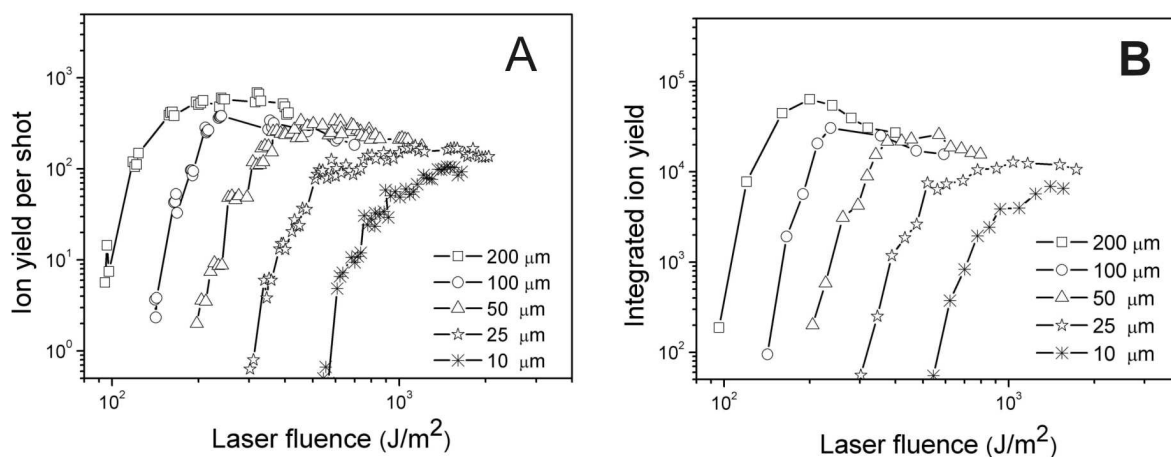
The fluence dependence of the ion yield is plotted for varying the number of laser shots used for integration shown in Fig.4.16. It is clear that the shape of the fluence dependence is quite independent of the number of laser shots used for integration, suggesting clearly that using the optimum fluence for yield per shot is an advantage from the point of view of sensitivity.
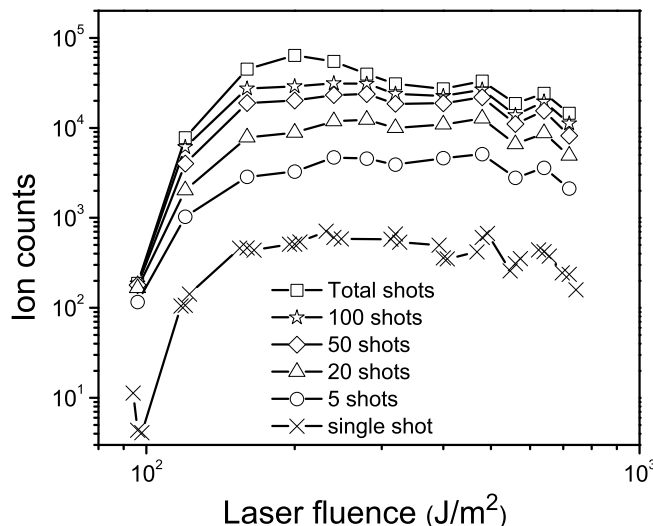
Figure 4.16: Dependence of the ion yield on laser fluence. The ion yield is integrated for different numbers of shots as indicated. The shape of the dependence is largely independent of the number of laser shots.The data were obtained for substance p desrobed from α-HCCA matrix.

Since a higher fluence can be used in an orthogonal TOF instrument without sacrifice in performance, improved sensitivity at fluence well above threshold can compensate for the reduced duty cycle inherent in an orthogonal geometry, and probably accounts for the similar overall sensitivity observed in the two types of instrument [25].

In the following illustrations and discussion, the 'ion yield per shot' at a given fluence is taken as the average of the counts from the first 20 laser shots (within the 5% fluence window), and the 'integrated ion yield', which represents a measure of the sensitivity, is taken as the sum of the counts in the first 500 shots. Fig.4.17 shows these two quantities plotted as a function of fluence for different fiber diameters. The ion yield per shot and the integrated ion yield are plotted in log-log scale. In both cases, they increase rapidly with fluence and then nearly saturate or in some cases decrease slowly at higher fluence. The saturation at high fluence is likely due to fragmentation and possible reduced transmission as a result of interactions in the dense plume. The results for the ion yield per laser shot (Fig.4.17A) are qualitatively consistent with results reported previously [20, 21].

Figure 4.17: Dependence of (A) ion yield per laser shot and (B) total integrated ion yield as a function of the laser fluence for different fiber diameters. The ion yield per laser shot (A) is the average of the first 20 laser shots on a new sample spot. The integrated yield (B) is the total ion yield integrated over 500 laser shots. The laser fluence from different fibers are normalized based on the area ratio of the burn marks shown in Chapter 3.

It is clear from Fig.4.17 that for fluence near threshold, there is a strong area dependence, as previously observed [20, 22]. For example, for fluence below 150 J/m^2, the ion yield for the 200 μm fiber is close to two orders of magnitude higher than the ion yield for the 100 μm fiber, although the spot area is only about 4 times larger. Dreisewerd *et al.* reported an approximate cubic dependence on area [20], and this seems to be consistent with our data, as shown in Fig.4.18a,b, where the yields are divided by the cube of the spot areas. In these plots, the steep portions of both the yield per shot curves (a) and the integrated yield curves (b) fall more or less on the same trend.

This strong area dependence has suggested to some that spot sizes smaller than $\sim$100 μm are not practical in MALDI, and limit the spatial resolution in imaging experiments [3, 24]. However, the data also indicate that for smaller beam spots, the yield saturates at higher fluence, and this can more than compensate for the smaller area. In order to compare the quantity relevant to sensitivity - the integrated yield per unit area - we have plotted in Fig.4.18e,f the yields normalized to the spot size. From these plots it is clear that the best sensitivity is obtained with the smallest fiber, and moreover, that for fluence above
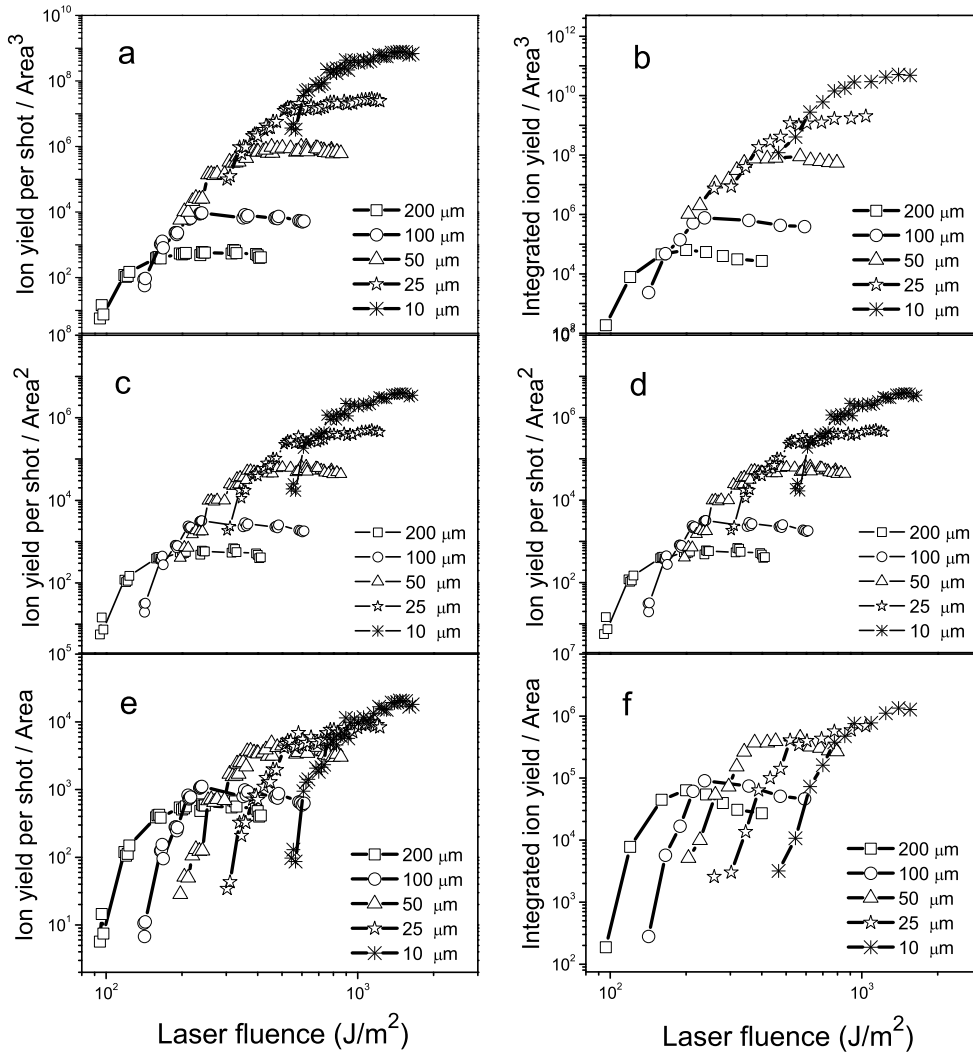
Figure 4.18: Illustration of the area dependence of the ion yield per shot (a,c) and the integrated ion yield (b,d). In the top panels (a,b), the yields are divided by the cube of the spot area, and indicate that yields measured at near-threshold fluence follow a cubic dependence on area. In the middle panels (c,d), the yields are divided by the square of the area, which shows the intermediate between the linear and cubic dependence. In the bottom panels (e,f), the yields are divided by the area, and indicate that yields measured above saturation fluence have an approximately linear dependence on area.

saturation (for a given fiber), the area dependence is better described as approximately linear. Since high fluence above saturation is typical in orthogonal TOF instruments, for practical purposes using such an instrument, a linear area dependence is an appropriate working assumption [30]. The dependence on the square of the area is also plotted in Fig.4.18c,d. This shows the intermediate situation between the linear and cubic area dependence.

Similar results were obtained using DHB and sinapinic acid as matrices, as shown in Fig.4.19. A higher fluence is needed to get the same yield using these matrices, and for many of the fibers, in particular the 10 μm fiber, the yield did not saturate at the highest fluence accessible with our optics. For this reason, the yield per unit area for the smaller fibers does not exceed that of the larger fibers in every case. However, the trends are similar to the trends in Fig.4.18, and it appears likely that more laser power, or better coupling optics would result in higher sensitivity with the smaller fibers.

Yield measurements were also made with a number of other analytes over a range of masses (substance P (1347 Da), melittin (2847 Da), bovine insulin (5734 Da), cytochrome C (12.3 kDa), myoglobin (16.7 kDa), and trypsin (23.8 kDa)) with two fiber diameters (200 μm and 25 μm) to test the generality of the above results. Sinapinic acid was used as the matrix for these measurements. Fig.4.20A shows the ion yield per shot dependence on fluence for difference analytes with 200 μm fiber. The absolute ion yields for different analytes have been scaled up for clarity. It shows the dependence of ion yield on fluence is essentially the same for all analytes. The earlier onset of saturation for substance P reflects the known high rate of metastable dissociation of this compound. The slight shift towards higher threshold fluence with increasing mass can be understood as a consequence of the increasing peak widths which results in a reduced signal-to-noise ratio. Fig.4.20B shows the comparison of ion yield per shot normalized to area for three of the samples. From all these different analytes, they all show quite similar fluence dependence. The integrated ion yield per unit area with the 25 μm fiber is higher than the yield per unit area with the 200 μm fiber.
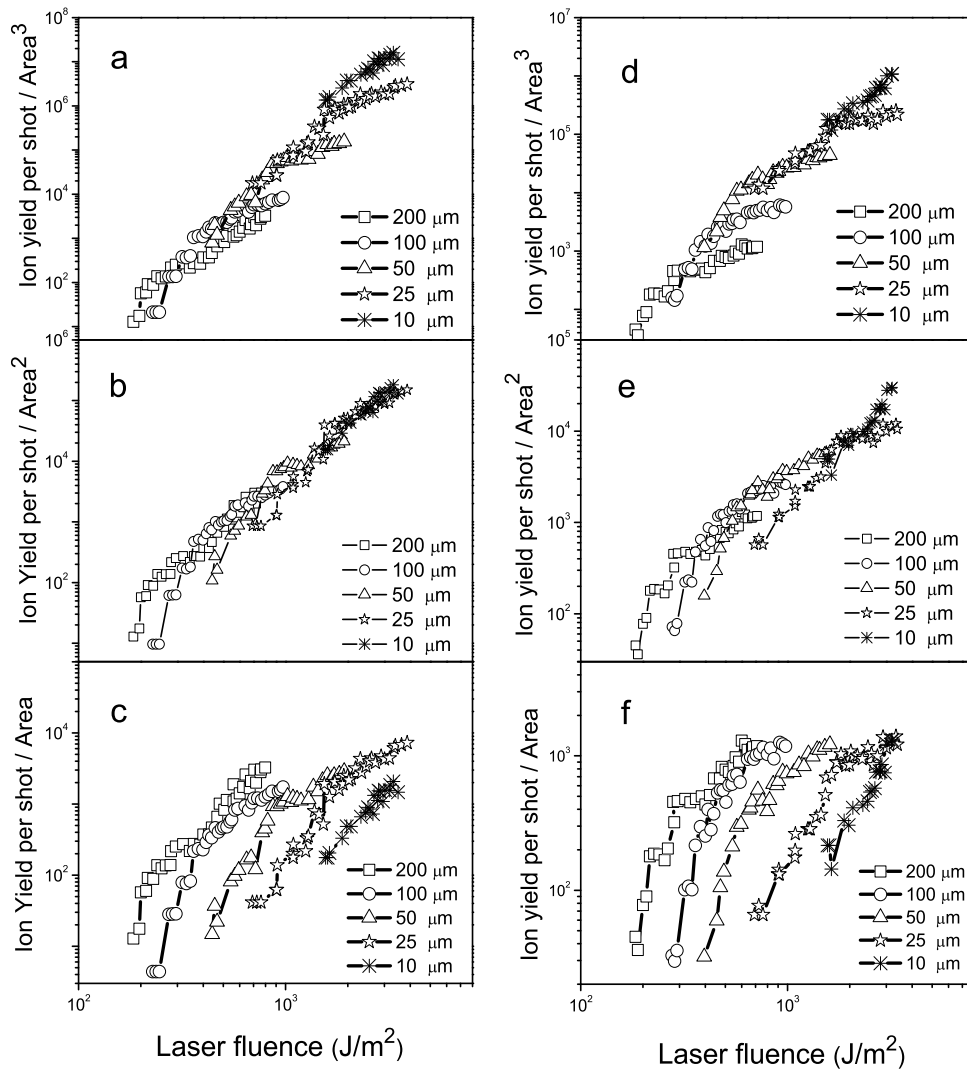
Figure 4.19: Fluence and area dependence for DHB (a,b,c) and sinapinic acid (d,e,f) matrices. The yields in top panels (a,d) are normalized to the cube of the area illustrating a cubic dependence for low fluence yields. The yields in the bottom panels (c,f) are normalized to the area. The limited data above saturation for these matrices are consistent with a linear area dependence for yields measured above saturation. The middle panels (b,e) are normalized to the square of the area showing the intermediate between the cubic and linear area dependence.
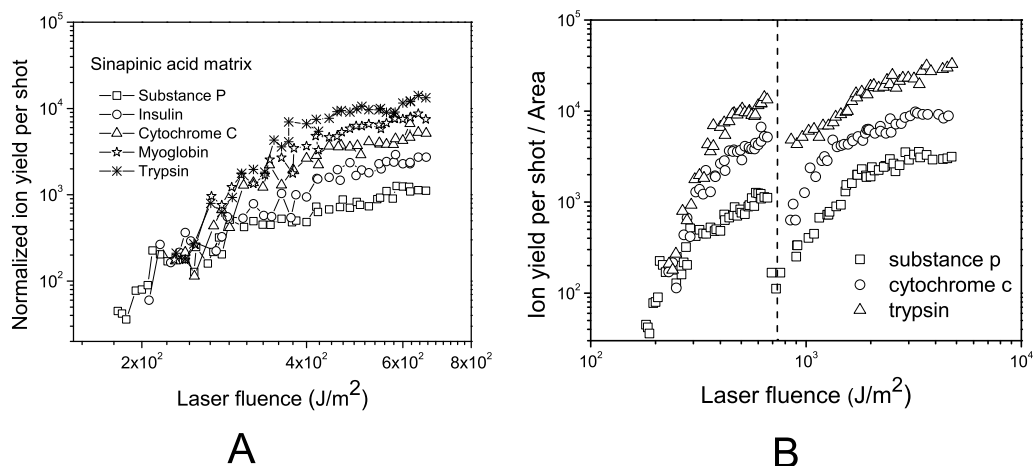
Figure 4.20: Fluence dependence of yield for different analytes. (A) The absolute yields for different analytes are scaled up for clarity. The fiber used is 200 μm. The fluence dependence is steeper for higher mass analytes. (B) The data to the left of the dashed line were obtained with a 200 μm fiber; the data to the right with a 25 μm fiber. The yields for both fiber were scaled up with the same factor. For each analyte the highest yield per unit area was obtained with the smaller fiber.

Since much higher fluence is used with smaller spot size, it might be reasonable to expect increased fragmentation. However, as shown in Fig.4.21, the fragmentation of insulin is only weakly affected by different irradiation conditions, and hardly at all by different fiber diameters at the respective saturation fluence.

The steeper than linear dependence of the yield on area at low fluence may be a result of increased collisional cooling as the plume size increases. On the other hand, in the fluence regime where the yield has already saturated due to fragmentation in the plume, a larger plume from a larger spot size would not realize an additional benefit from additional cooling, so a linear dependence on area seems consistent. A linear dependence on area (at high fluence) and a higher saturation fluence for smaller spot sizes, indicates that better sensitivity is obtainable with smaller spot sizes. This has implications for MALDI imaging applications where increased sensitivity allows less abundant analytes to be imaged, and the smaller spot size indicates potential for improved spatial resolution, if better sample
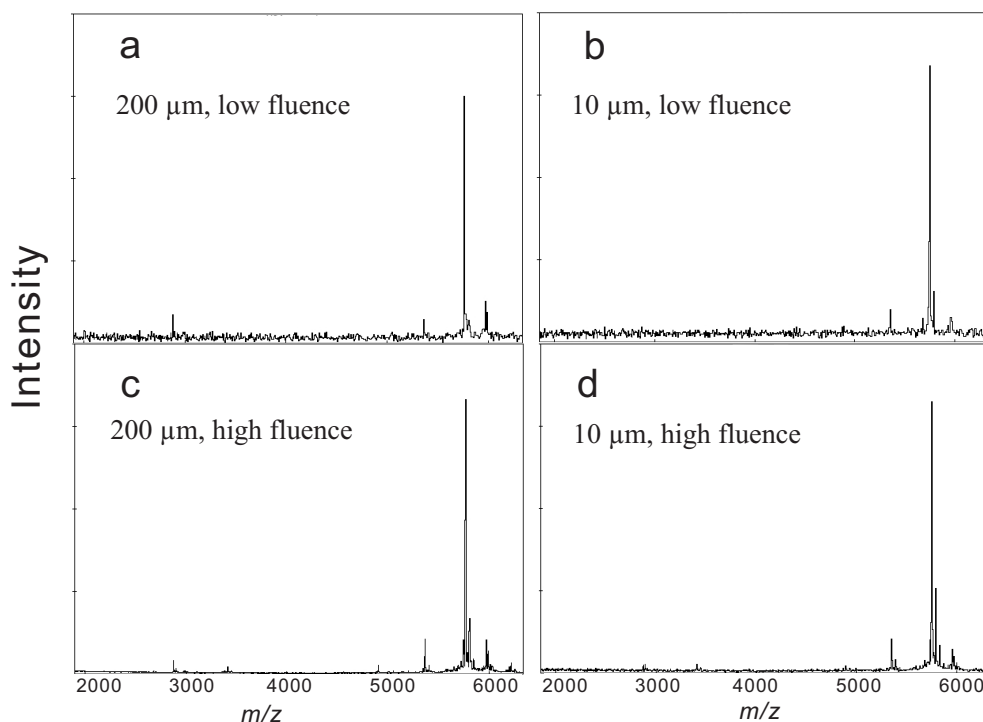
Figure 4.21: Spectra of insulin from SA with different irradiation conditions using the N2 laser with 2-m fibers: the left panels (a,c) with the 200 μm fiber, and the right (b,d) with the 10 μm fiber; the top panels (a,b) at the lowest fluence, and the bottom (c,d) at the saturation fluence.

preparation methods are developed.

From the data of Fig.4.17, we have observed the linear and cubic area dependence of ion yield per shot and integrated ion yield at different fluence regimes by replotting them in Fig.4.18. This is actually just part of information reflected from this graph which is obtained by drawing a line parallel to the 'Y' axis. But what if we draw a line parallel to the 'X' axis in this graph? It is also found that there is a strong detection 'threshold fluence' dependence on area along the horizontal line. The 'threshold fluences' are taken for each fiber with the matrices of HCCA, DHB, and SA. The threshold fluence dependence on the size of fiber is shown in Fig.4.22. There is a steep rise of threshold fluence with decreasing spot size. It is assumed that a minimum absolute number of ions must be generated for a signal to be detected; this number of ions will depend on the size of the area as well as the laser fluence. For small spot sizes the smaller available area for ion generation must be compensated by a correspondingly higher laser fluence. It is also clear
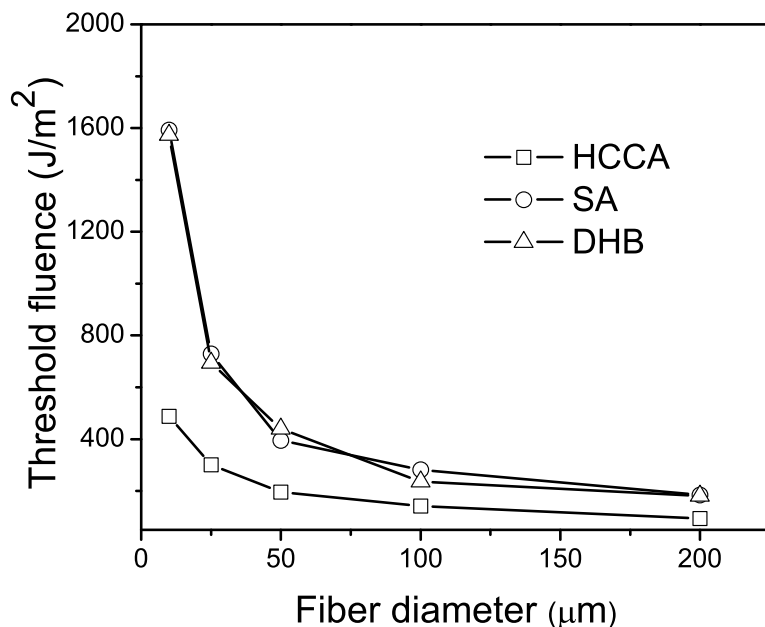
Figure 4.22: The threshold fluence dependence on the spot size. The threshold fluence goes up as the spot size decreases for all these matrices. Both DHB and SA matrices have similar threshold fluences and are higher than HCCA matrix.

that DHB and SA have similar threshold fluences which are much higher than that of the HCCA matrix, especially for the smaller spot sizes. Besides the inherent differences in the optical absorption coefficients between these matrices, more inhomogeneity of the sample and relatively larger crystal sizes for DHB and SA than HCCA matrix may also contribute to their larger difference in the threshold fluence although thin layer preparation method was used.

A demonstration of improved sensitivity with a smaller fiber is shown in Fig.4.23 for melittin. In this measurement, we scanned the same defined area using 25 μm and 200 μm diameter fibers. The approximate order of magnitude improvement using the 25 μm fiber is consistent with Fig.4.18, but some caution should be exercised in such a comparison, because the effective spot size for desorption is expected to be dependent on the rastering pattern. The effective spot size of the fiber is defined as follows:
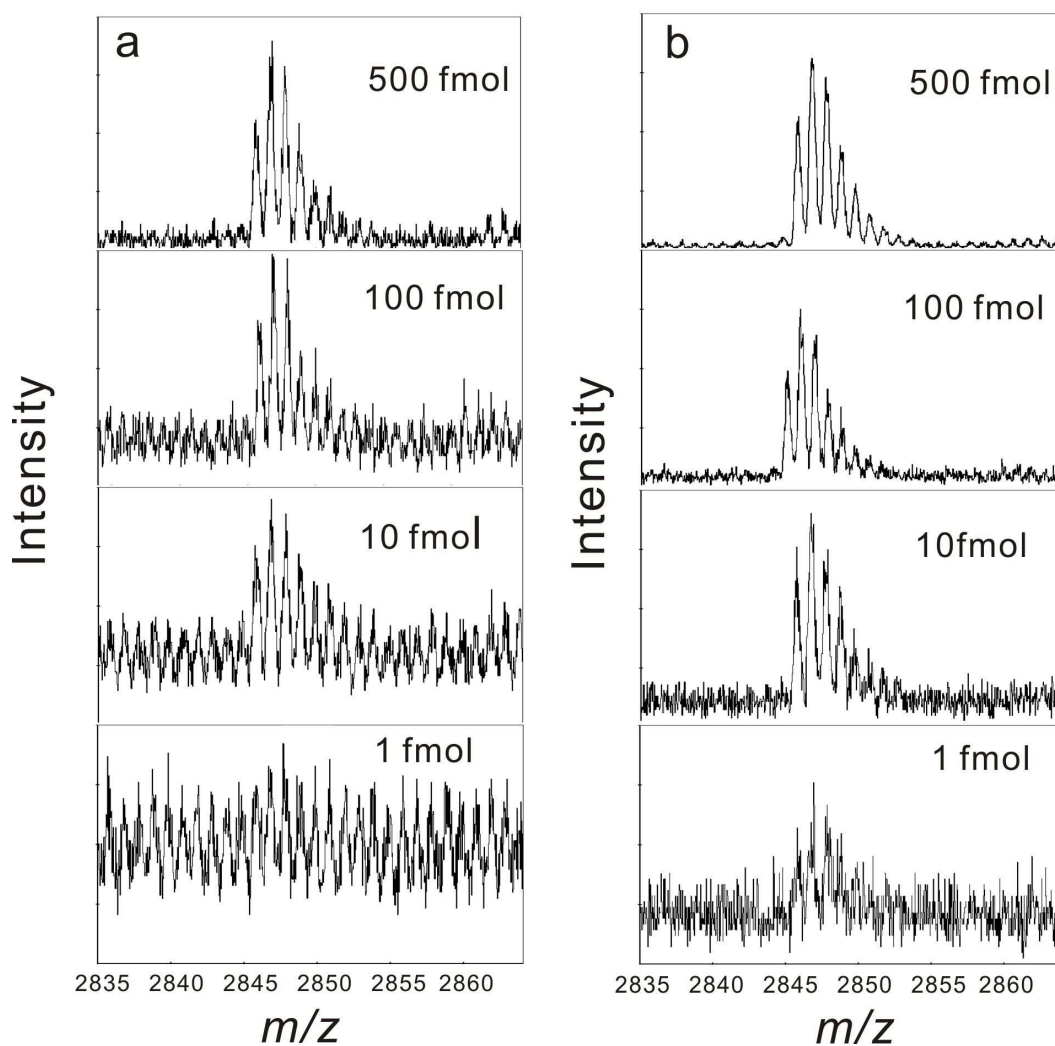
Figure 4.23: Comparison of the molecular ion region of the mass spectrum of melittin using (a) a 200 μm fiber and (b) a 25 μm fiber, with different amounts of deposited sample. Under identical conditions, the detection limit appears to be about an order of magnitude lower when the 25 μm fiber is used.
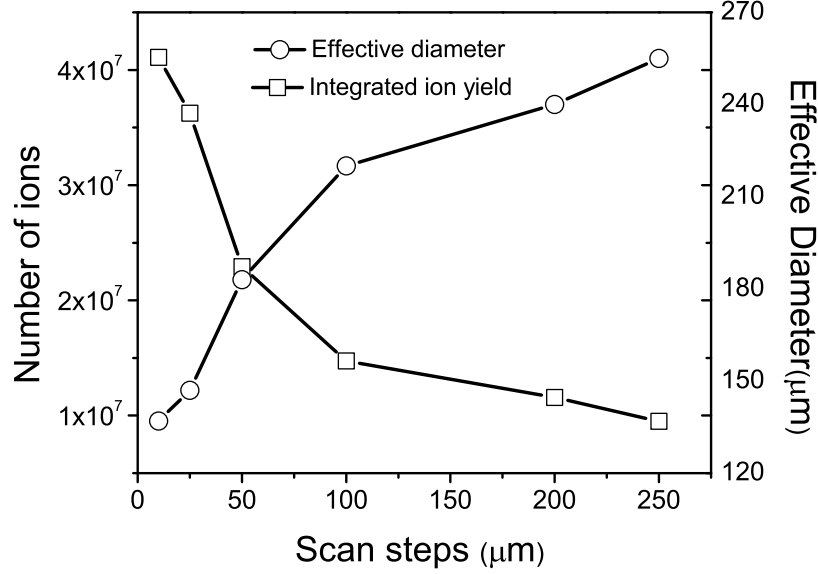
Figure 4.24: The variation of integrated ion yield scanning from a defined area by changing the scan step sizes. The integrated ion yield increases when the scan step size becomes smaller.

$$\frac{N_{spot}}{A_{eff}} = \frac{N_{scan}}{A_{scan}}$$
$$A_{eff} = \frac{N_{spot}}{N_{scan}} A_{scan} \tag{4.4}$$

where N_{spot} is the integrated ion yield from single sample spot. A_{eff} is the effective spot size of the fiber. N_{scan} is the integrated ion yield from scanning a defined area. A_{scan} is the defined scan area. It is found that for the 200 μm fiber the effective spot size, A_{eff}, increases as the increasing of the scan step size when N_{spot} and A_{scan} are fixed, indicating that the total number of ions from a defined area decreases as increasing the scan step size, shown in Fig.4.24.

This trend suggests that reducing the scan step size for large size fiber can improve the integrated ion yield for a defined area. This might be because the smaller scan step size
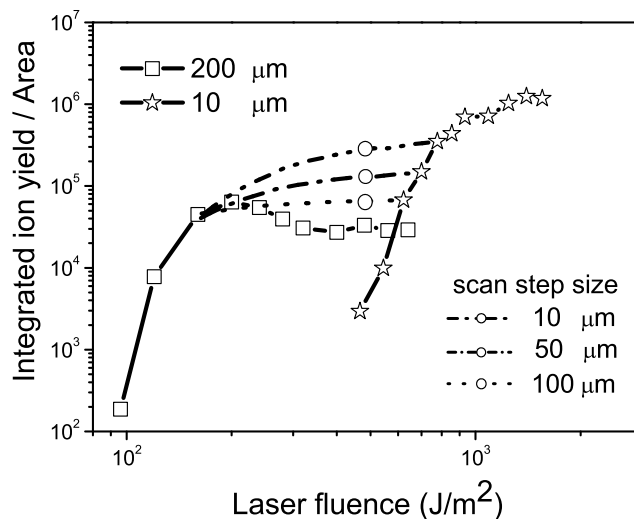
Figure 4.25: The effect of changing scan step size on the integrated ion yield using a 200 μm fiber compared with the use of a 10 μm fiber. A smaller step size results in a higher integrated ion yield for the same fluence, indicated by the open circles, and appears to be consistent with the yield measured with a smaller fiber.

will exposes new sample material a little at a time, and so may exhibit behavior consistent with a small fiber. For example, we have also observed that the yield from a given area increases when the step-size between raster lines is reduced (indicated by the open circles in Fig.4.25). For 10 μm steps, the yield from the 200 μm fiber seems to fall on a trend consistent with the measurements made with the 10 μm fiber. It also indicates that in the imaging experiments the rastering pattern is very important. In particular, continuous rastering seems much better than irradiating discrete spots in terms of sensitivity.

4.5 Conclusions

The total integrated ion yield from a given sample area has the same dependence on fluence as the yield per laser shot, indicating that the best sensitivity is achieved by using fluence at or above the level at which the yield per shot saturates. This is in contrast to the more common practice of using near-threshold fluence in axial MALDI instruments.

The dependence of the yield on area depends on the fluence range considered. For a fluence near threshold, the dependence is approximately cubic, but, for fluence above the saturation fluence, the dependence is closer to linear. This result, combined with the result that saturation occurs at higher fluence for smaller spots, means that higher integrated yield per unit area (sensitivity) can be achieved with smaller beam spots. In our experiments the highest yield per unit area was observed with a 10 μm beam spot.

References

[1] Caprioli, R. M.; Farmer, T. B.; Gile, J. *Anal. Chem.* **1997**, *69*, 4751–4760.

[2] Stoeckli, M.; Farmer, T. B.; Caprioli, R. M. *J. Am. Soc. Mass Spectrom.* **1999**, *10*, 67–71.

[3] McDonnell, L. A.; Heeren, R. M. A. *Mass spectrom. rev.* **2007**, *26*, 606–643.

[4] Garden, R. W.; Sweedler, J. V. *Anal. Chem.* **2000**, *72*, 30–36.

[5] Spengler, B.; Hubert, M. *J. Am. Soc. Mass Spectrom.* **2002**, *13*, 735–748.

[6] Ens, W.; Piyadasa, G.; Collado, V.; Krokhin, O.; Loboda, A.; McNabb, J. R.; Qiao, H.; Spicer, V. L.; Standing, K. G.; In *Proceedings of the 53rd ASMS conference on mass spectrometry and allied topics*, May,2005.

[7] Jackson, S. N.; Ugarov, M.; Egan, T.; Post, J. D.; Langlais, D.; Schultz, J. A.; Woods, A. S. *J. Mass Spectrom.* **2007**, *42*, 1093–1098.

[8] Baluya, D. L.; Garrett, T. J.; Yost, R. A. *Anal. Chem.* **2007**, *79*, 6862–6867.

[9] Brown, R. S.; Lennon, J. J. *Anal. Chem.* **1995**, *67*, 1998–2003.

[10] Vestal, M. L.; Juhasz, P.; Martin, S. A. *Rapid Commun. Mass Spectrom.* **1995**, *9*, 1044–1050.

[11] Chernushevich, I. V.; Ens, W.; Standing, K. G. *Anal. Chem.* **1999**, 452A–461A.

[12] Chaurand, P.; Schriver, K. E.; Caprioli, R. M. *J. Mass Spectrom.* **2007**, *42*, 476–489.

[13] Altelaar, A. F. M.; Taban, I. M.; McDonnell, L. A.; Verhaert, P. D. E. M.; de Lange, R. P. J.; Adan, R. A. H.; Mooi, W. J.; Heeren, R. M. A.; Piersma, S. R. *Int. J. Mass Spectrom.* **2007**, *260*, 203–211.

[14] Kruse, R.; Sweedler, J. V. *J. Am. Soc. Mass Spectrom.* **2003**, *14*, 752–759.

[15] Schwartz, S. A.; Reyzer, M. L.; Caprioli, R. M. *J. Mass Spectrom.* **2003**, *38*, 699–708.

[16] Ingendoh, A.; Karas, M.; Hillenkamp, F.; Giessmann, U. *Int. J. Mass Spectrom. Ion Processes* **1994**, *131*, 345–354.

[17] Ens, W.; Mao, Y.; Mayer, F.; Standing, K. G. *Rapid Commun. Mass Spectrom.* **1991**, *5*, 117–123.

[18] Eckerskorn, C.; Strupat, K.; Karas, M.; Hillenkamp, F.; Lottspeich, F. *Electrophoresis* **1992**, *13*, 664.

[19] Strupat, K.; Karas, M.; Hillenkamp, F.; Eckerskorn, C.; Lottspeich, F. *Anal. Chem.* **1994**, *44*, 464.

[20] Dreisewerd, K.; Schurenberg, M.; Karas, M.; Hillenkamp, F. *Int. J. Mass Spectrom. Ion Processes* **1995**, *141*, 127–148.

[21] Westmacott, G.; Ens, W.; Hillenkamp, F.; Dreisewerd, K.; Schurenberg, M. *Int. J. Mass Spectrom.* **2002**, *221*, 67–81.

[22] Feldhaus, D.; Menzel, C.; Berkenkamp, S.; Hillenkamp, F.; Dreisewerd, K. *J. Mass Spectrom.* **2000**, *35*, 1320–1328.

[23] Fournier, I.; Beavis, R. C.; Blais, J. C.; Tabet, J. C.; Bolbach, G. *Int. J. Mass Spectrom. Ion Process.* **1997**, *169/170*, 19–29.

[24] Schriver, K.; Chaurand, P.; Caprioli, R. M.; In *Proceedings of the 51st ASMS conference on mass spectrometry and allied topics*, 2003.

[25] Loboda, A. V.; Krutchinsky, A. N.; Bromirski, M.; Ens, W.; Standing, K. G. *Rapid Commun. Mass Spectrom.* **2000**, *14*, 1047–1057.

[26] Loboda, A. V.; Ackloo, S.; Chernushevich, I. V. *Rapid Commun. Mass Spectrom.* **2003**, *17*, 2508–2516.

[27] Vorm, O.; Roepstorff, P.; Mann, M. *Anal. Chem.* **1994**, *66*, 3281–3287.

[28] Fournier, I.; Tabet, J. C.; Bolbach, G. *Int. J. Mass Spectrom.* **2002**, *219*, 515–523.

[29] Fournier, I.; Marinach, C.; Tabet, J. C.; Bolbach, G. *J. Am. Soc. Mass Spectrom.* **2003**, *14*, 893–899.

[30] Qiao, H.; Collado, V.; Piyadasa, G.; Loboda, A. V.; Kozlovski, V.; Standing, K. G.; Ens, W.; In *Proceedings of the 53rd ASMS conference on mass spectrometry and allied topics*, May,2005.

Chapter 5

Studies on the detection properties of microchannel plate detectors

5.1 Introduction

A microchannel plate (MCP) (Fig.5.1) amplifies electron signal when a single incident particle (ion, electron, photon etc.) strikes the channel wall. Secondary electrons are accelerated by the electric field across both sides of the MCP. Due to the tilted angle of the channels, the secondary electrons will experience many collisions against the channel surface. As a result, the original signal is amplified by several orders of magnitude depending on the electric field strength and the geometry of the MCP. In general, a single MCP has a gain of $10^3 - 10^4$. If two or more MCPs are operated in series, the gain of MCPs can go up to 10^8 in the output. The output signals are typically collected in any of several ways, including metal or multi-metal anodes, resistive anode (one- or two- dimensional), wedge and strip anodes. It also has very short transit time in the range of 100 ps, which makes it suitable for applications demanding ultra-high time resolution [1].

Normally, MCPs are arranged in the Chevron configuration [2] shown in Fig.5.2. In the Chevron configuration, the MCPs are oriented so that the channel bias angles provide a sufficiently large directional change so as to inhibit positive ions produced at the output
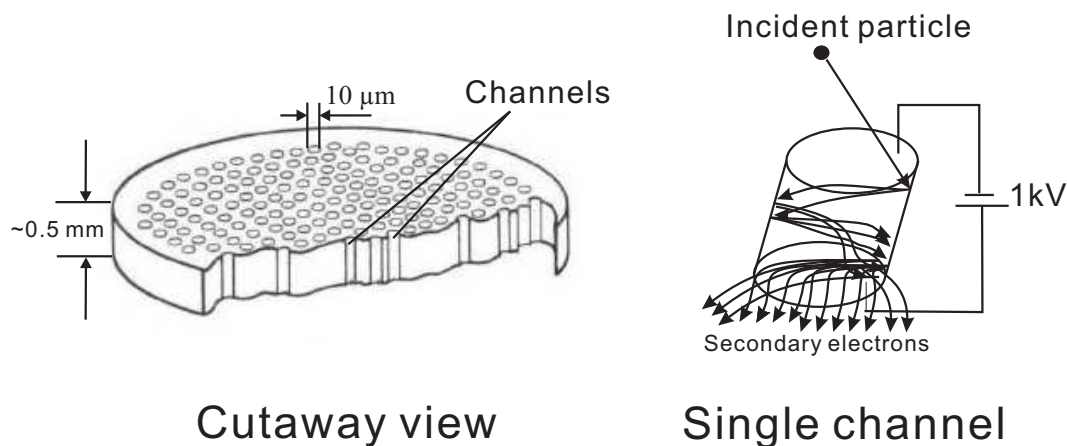
Figure 5.1: The schematic diagram of microchannel plate in cutaway view and single channel. After the incident particle strike the channel wall, secondary electrons are produced and multiplied through continuous collisions.

of the rear plate from reaching the input of the front plate. This will greatly suppress the ion feedback and reduce the background noise and therefore allow higher gain. With higher gains, it was found that the charge pulse height distribution changed radically from a negative exponential to a quasi-Gaussian shape with a full width at half maximum of typically 120 - 150%. But as the interplate bias voltage increases, the peak gain remains essentially constant while the pluse height distribution decreases to about 50%. This narrowing of the pulse height distribution is advantageous in many pulse processing schemes.

Since MCPs have some unique properties such as high gain, high spatial resolution, and high temporal resolution (subnanosecond), they are widely used in a variety of applications including imaging microscopy, electron spectroscopy and microscopy, mass spectrometry, etc. When using MCPs for ion detection in mass spectrometry, the detection efficiency is of primary importance. Studies on the MCP detection efficiency have been carried out for a long time. Different experiments have been performed to examine the detection characteristics of the MCP. The ions used in those experiments ranged from atomic ions, amino acid ions, peptides and proteins ions. With the increase of accessible mass range for molecular ions, it becomes more important to study the detection properties of the MCP especially for large molecular ions.
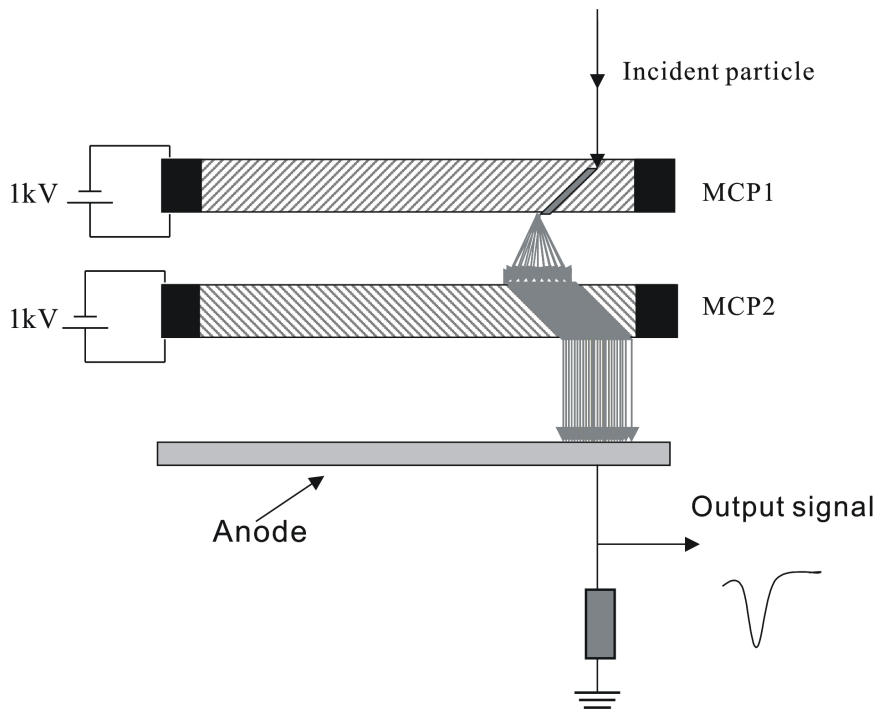
Figure 5.2: Schematic diagram of the Chevron arrangement of MCPs. These two MCPs are stacked together with orientation as (v-like) shape. The voltage potential across each plate is about 1 kV. This arrangement can not only greatly enhance the gain but suppress the ion feedback and reduce the background noise.

Detection efficiency measurement with atomic ions

Gao *et al.* [3] measured the absolute detection efficiency of MCP with H^+, He^+, and O^+ in the energy range from 250 to 5000 eV, showing that the absolute efficiency was proportional to the particle energy and saturated near 3 keV at about 60% efficiency, which is close to the open area ratio of typical MCPs ($\sim 60\%$). Muller *et al* [4] also measured the absolute detection efficiency of MCP for electrons and Mg^+ ions. They also showed that the detection efficiency is primarily a function of the particle impact energy. The efficiency went up to 80% at an impact energy of 4.4 keV which was well above the open area ratio of the MCP. They attributed such a high detection efficiency to the application of a repelling grid (~ 100 V) in front of the first MCP which could repel the secondary electrons generated from the 'dead areas' back to the MCP. Some rare gas ions such as Ne^+, Ar^+, Kr^+ [5–7] were also studied and showed similar dependence of detection efficiency of the MCP on the particle impact energy, consistent with the

previous measurements.

The above measurements and others were made by comparing the counting rate measured on the MCP detector with the corresponding current signal measured on a Faraday cup [3, 4, 8]. Although this method is straightforward, it does not seem to be an appropriate one for determining the single-particle detection efficiency. The typical current measured in those experiments was less than 5 fA, corresponding to a particle count rate $< 5 \times 10^4 s^{-1}$. However, the lowest ion currents detectable by an electrometer are in the range of $> \sim$ 10 fA, corresponding to particle rates $> 10^5 s^{-1}$, which is above the typical single-particle count rate in those experiments. At elevated count rates, MCP shows a decrease in gain [9], which could denote a source of error in the determination of the detection efficiency at higher count rates [4].

Another method based on coincidence techniques was introduced to determine the absolute detection efficiency of the MCP [5, 6, 10]. The basic idea of this technique is to determine the ratio between the coincidence and electron count rate. A photo-ionization technique was normally used to generate a well defined event which consists of a gas ion and an electron. This technique allows the determination of the detection efficiency of the MCP even at low count rates and without knowing the absolute event rates of ions. However, only low mass gas ions less than 100 Da with relatively lower impact energy < 5 keV were used to study the detection efficiency of the MCP in these experiments.

Detection efficiency measurement with large molecular ions

With the development of new ionization techniques, the accessible mass range has been greatly extended. Large molecular ions were also used to study the detection properties of the MCP. The 252-Cf plasma desorption mass spectrometer was used to study the secondary electron emission properties of the MCP with amino acids and small peptide ions up to (bradykinin: 1059 Da) [11]. The experiment showed that the secondary electron coefficient of the MCP was linearly proportional to the incident ion mass and exponential in the velocity. Secondary ion mass spectrometry (SIMS) was also used to study the relative detection efficiency of the MCP for larger mass ions (polystyrene oligomers, 10,000Da)

with an impact energy (20 keV) [12]. The relative detection efficiency is approximately 80%(related to the open area ratio $\sim 54.5\%$). Matrix-assisted laser desorption/ionization (MALDI) technique has enabled generation even larger molecular ions [13, 14] and molecular ions up to 66 kDa were used to study the detection efficiency of the MCP [15]. It was found that the detection efficiency of the MCP was only about 5% for molecular ions of 66 kDa with 30 keV energy and only slightly higher than 1% for 10 keV ion of the same mass. The secondary electron coefficient of the MCP was found to scale linearly with the ion mass, consistent with the previous study [11], but to about the fourth power of the ion velocity.

Ion detection with secondary electrons and secondary ions

Detection of ions in mass spectrometry is usually accomplished through the ion collision with a surface. Either secondary electrons or secondary ions produced in the collision are accelerated to produce a cascade, eventually amplifying the signal to a detectable level. Detectors designed to use secondary electron emission have better time resolution than those relying on secondary ion emission because of the multiple ion species and the longer transit time of secondary ions [16–18]. From this point of view, it is preferable to use secondary electrons for ion detection, which is one of the unique advantages of MCP detectors. On the other hand, the sensitivity and mass range depend on the emission yield of the secondary particles, so it seems reasonable to use the secondary ions with the highest yield for detection of large molecular ions.

It is well established that the secondary electron emission efficiency decreases as the ion velocity decreases [11, 17, 19–21]. Secondary electron emission efficiency has been measured on both CsI and stainless steel surfaces using a coincidence technique [20]. In this experiment, the emission efficiency of secondary electron was measured about 20% from both surfaces for transferrin ($\sim 79\,500$ Da) with 10 keV energy (0.13 eV/Da). This is, however, about 20 times higher than the 1% secondary electron emission efficiency from the MCP for molecular ions with similar mass and energy [15]. This large discrepancy might be related to the difference in the instrumentation or some artifacts in the experiments

which are not clearly understood.

The decreasing of secondary electron emission efficiency indicates that ion detection with secondary electrons will have a limitation for large, slow moving molecular ions. Spengler *et al.* [22] found that when a conversion dynode was used, the secondary electron emission was the main process for small projectile ions, and secondary ion emission was dominant for the detection of ions larger than $\sim$10,000 Da. 'Threshold' velocities about 1.8×10^6cm/s ($\sim$ 1.7 eV/Da) on a Cu surface bombarded by water clusters (up to 60,000 Da) and 1.0×10^4m/s on Al_2O_3 surface with collisions of insulin (5733 Da) have been found for efficient secondary electron emission, below which it is claimed that no electrons are emitted [23–25]. However, in MALDI molecular ions with mass up to $\sim$ 300,000 Da and with an accelerating voltage of 30 kV have been detected [26]. This corresponds to an energy per unit mass of $\sim$ 0.1 eV/Da, about 17 times lower than the threshold energies mentioned above. In light of the recent measurements, a 'threshold' velocity is better interpreted as the velocity of the molecular ion where the secondary electron yield drops below unity [15]. Although it remains possible to detect ions when the secondary electron yield is less than unity, the detection probability for large, slow moving molecular ions (66 kDa at 26 keV) is less than about 20% [21]. Diminished detection efficiency for high mass ions necessitates longer data acquisition times (or more sample) to achieve reasonable statistics and introduces limitations on quantitative assessments of the relative concentration of analyte ions.

However, the secondary ion emission yield for the primary ions below $\sim$ 1 eV/Da is much larger than the secondary electron emission yield [16–20]. From reported experiments [18, 20], it is still close to unity (>70%) even for large molecuar ions up to 100 kDa with energy about 5 keV. The secondary ion emission efficiency was almost constant and independent of the ion mass and the material of the surface [20]. The study of the secondary electron-to-ion ratio showed that this ratio decreased rapidly with decreasing velocity but appeared to approach a constant value about 0.2 below a velocity $\sim$ 1 eV/Da [17]. Overall, the comparison between the emission efficiency of secondary electrons and secondary ions suggests an advantage in using secondary ion emission for

the large molecular ion detection.

The characteristics of the secondary electron and secondary ion emission have been widely studied with some surfaces such as: Cu [23, 24], stainless steel [17, 20], CsI [17, 20, 21], and CuBe [20, 27]. A commercial high mass detector based on secondary ion emission has been introduced for detecting protein complexes such as Immunoglobulin M (1 MDa) [28]. However, most TOF instruments still use MCPs for better mass resolution and because high molecular ion detection is less important in modern proteomics although secondary ion emission is more efficient. Moreover, in linear MALDI, the low (but non-zero) efficiency for large proteins is often adequate. That is why MCPs are still by far the most common detector in TOF mass spectrometry. Therefore it is important to characterize them as carefully as possible.

An important difficulty in many of the measurements has been the interpretation of the analog signal producted by a plume of ions from a single MALDI event. This limits the reliability of the previous measurements. In the study of secondary electron emission of MCP with 252-Cf plasma desorption mass spectrometry [11], post-acceleration voltages up to 9 kV were applied onto the detector for small amino acids and peptides. By varying the energy and mass of incident ions, the secondary electron emission properties of MCP were studied with respect to the unity detection condition of MCP at high acceleration voltages. However, this condition can only be realized for smaller ions. Recently a specially designed detector consisting of a MCP and an energy-sensitive superconducting tunnel junction (STJ) detector was used in an axial-injection TOF mass spectrometer to study the secondary electron emission properties of the MCP [15]. The STJ detector is highly sensitive to the total energy of the incident ions and less sensitive to their velocities [29]. The STJ detector has 100% detection efficiency for molecular ions with sufficient kinetic energy (>5 keV). It was used as a reference to calibrate the detection properties of the MCP detector. A MALDI ion source was used to generate high mass molecular ions (up to bovine albumin at 66 kDa) for this measurement. However, it is difficult in MALDI to ensure single-ion counting because of the large number of ions produced per laser pulse. The situation was improved by drastically reducing ion transimission, but the

pulse-to-pulse fluctuations in MALDI make it difficult to neglect or evaluate the probability that two ions are transmitted. However, the introduction of orthogonal-injection time of flight mass spectrometers allows the MALDI ion plume to be spread over many injection events so that single-ion counting methods can be safely used [30].

In this chapter, the detection properties of the MCP detector were studied. The experiments were performed on an orthogonal-injection MALDI time of flight mass spectrometer. A novel detector based on the high emission efficiency of secondary ions was used as a reference. The mass of molecular ions went up to 79,500 Da (transferrin). The dependence of relative detection efficiency of the MCP on the energies and masses of ions was studied. The secondary electron emission properties of the MCP were also analyzed.

5.2 Experimental

5.2.1 Instrumentation

The experiments were performed on an orthogonal-injection MALDI TOF mass spectrometer. The schematic diagram is the same as the one used for the laser beam profile study in Chapter 3. The N_2 laser (VSL-337ND: Laser Science, Inc. Wavelength 337 nm) was used. The optical fiber is 200 μm in diameter and is used to transmit the laser energy onto the sample target. The advantages of an orthogonal-injection TOF instrument have been discussed in detail in the previous chapters. In this experiment, the orthogonal-injection geometry makes single ion counting feasible due to the high extraction rate of the ion beam into the TOF analyzer. By using the ion counting method, it is much easier to interpret the data compared to analogue data acquired with axial TOF instrument.

In this experiment, the acceleration voltages of ions were varied from 4.6 to 10.6 kV with an increment of 2 kV. The samples were prepared using the standard dried-droplet method. The analytes used were in a wide mass range: bacytracin (1400 Da), melittin (2845 Da), insulin (5733 Da), cytochrome C (12,327 Da), trypsin (23,460 Da), ovalbumin

(43,000 Da), bovine albumin (66,430 Da), and transferrin (79,500 Da). The matrix used was sinapinic acid. In the dried-droplet method, sinapinic acid matrix was dissolved in a mixture of acetonitrile/water (1:1, v/v) and 0.1% trifluoroacetic acid (TFA) at a concentration of 20 mg/mL. All analytes were dissolved in the bidistilled water with a concentration of about 1 pmol/μL. The analyte and matrix solution were mixed with the final molar analyte-to-matrix ratio of $\sim 2 \times 10^{-5}$ as typically used in MALDI. About 1 μL of the mixture solution was deposited onto the target and air dried.

5.2.2 The hybrid detector

A schematic diagram of the detector is shown in Fig.5.3. This detector consists of a pair of matched MCPs placed in front of four independent anodes. The MCPs were purchased from Burle Industries,Inc. (Lancaster, PA, U.S.). Some basic parameters of the MCP are shown in Table 5.1. There are four independent anodes which collect the secondary electrons. The generated current pulses will be preamplified and then fed to a constant-fraction discriminator (CFD). Its output will be delivered to a time-to-digital converter (TDC) to generate a spectrum. The MCPs are arranged in the Chevron configuration. In this specially designed detector, an intermediate electrode is placed in front of the MCPs, one half of which is a CuBe venetian blind converter, and the other half is a 95% transmission grid. Therefore the MCPs will be divided into two functional parts, which are simply called 'converter MCP' and 'bare MCP' corresponding to the portion of MCP behind the CuBe converter and the grid, respectively. The four indpendent anodes will also be divided into two groups, two of which will collect the signal from the 'converter MCP' and the other two anodes will work for the 'bare MCP'. The spectra can be recorded independently from these two parts. The images of the detector are shown in Fig.5.4.

CuBe venetian blind dynodes have been used previously for ion-to-electron conversion to detect large molecular ions by Hillenkamp and Spengler [22, 31]. In our experiment, the CuBe venetian blind converter is intended to provide normalization for characterizing the detection properties of the MCP detector. It is held at -12 kV for all the measurements,
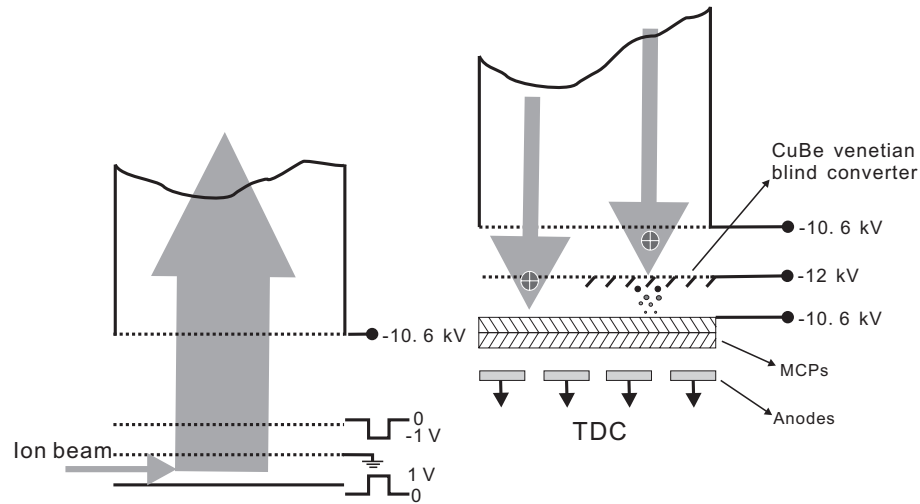
Figure 5.3: Schematic diagram of the hybrid MCP/CuBe venetian blind converter detector (right). The ion acceleration region is also shown on the left. In the hybrid detector, an intermediate electrode is placed in front of the MCP consisting of a 95% transmission grid and a CuBe venetian blind converter. The voltage on this electrode is fixed at -12 kV.

Table 5.1: List of typical parameters of the MCP used in this experiment.

Parameters	Value
channel diameter	10 μm
center to center spacing	12μm
thickness	0.46 mm
L/D ratio	46:1
bias angle	8^0
open area ratio	61%

where its efficiency based on earlier results is expected to be near unity and largely mass independent [18, 20]. The voltage potential across the two MCPs is about 2 kV, and this voltage is floated on the acceleration voltage. Therefore the potential on the first surface of the MCP is always equal to the acceleration voltage and the energy of the ions striking the MCP is equal to qV_{acc}. Since the acceleration voltage is always more positive than -12 kV, when the incoming ions collide on the CuBe converter, only negative secondary particles (electrons and negative ions) can be accelerated to the first MCP. The minimum potential is about 1.4 kV when the acceleration voltage is set as at -10.6 kV. Studies showed that the secondary particles produced after the collision of primary molecules with the dynode were
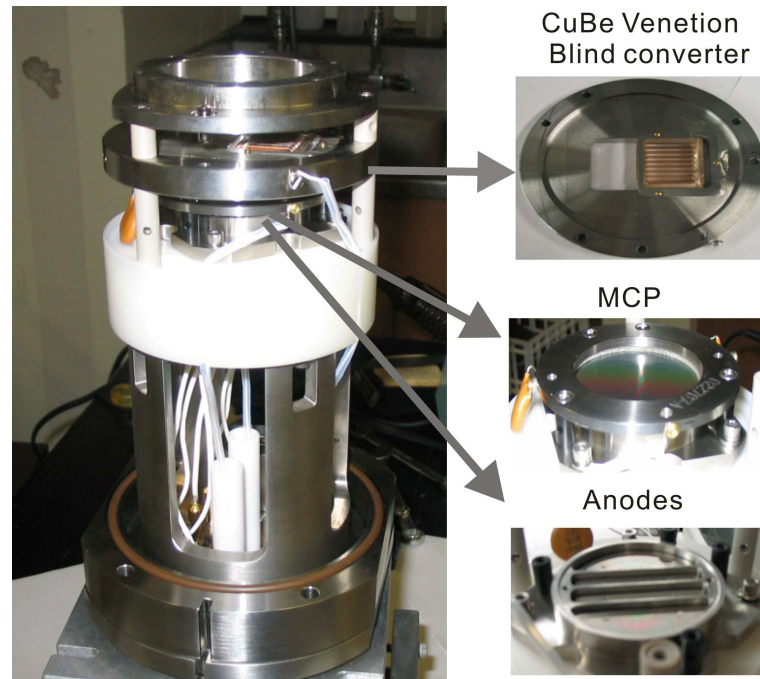
Figure 5.4: The images of the hybrid detector. An intermediate electrode consisting of grid and CuBe venetian blind converter is placed in front of the MCPs. The MCPs are arranged in Chevron configuration. There are four independent anodes used to collect secondary electron to generate current pulse for ion detection.

a sputtering process, rather than surface-induced dissociation. The secondary particles reflect the contamination of the dynode surface rather than the structure of the primary ions [17, 22]. Normally the secondary ions are species such as: H^-, O^-, OH^-, CN^-, I^- and so on [17, 19, 22]. The masses of the secondary ion species typically range from 1 to 100 Da. For these low mass secondary particles, the energy per unit mass of the secondary ions is larger than 14 eV/Da regardless of the primary ions. For this reason we assume that the secondary electron emission of the MCPs is near saturation according to the previous measurement [20].

For the CuBe venetian blind converter, more than one secondary species might be produced by the collision of one primary ion. Suppose the secondary electron emission efficiency of the MCP is $\epsilon_e (\leq 1)$ which is defined as the probability of producing one or more electrons from the MCP after the impact with one particle, the $(1 - \epsilon_e)$ is the probability of no secondary electron produced. Assuming the emission efficiency of the MCP is same

for all the secondary particles, the probability of producing no ions will be $(1 - \epsilon_e)^n$ for the multiple secondary particles, where n is the total number of secondary particles. So the total secondary electron emission efficiency of the MCP for n secondary particles will be $\epsilon_{en} = 1 - (1 - \epsilon_e)^n$. This shows that the total electron emission efficiency of the MCP increases as the multiplicity ($'n'$) of the secondary particles becomes larger. Therefore the 'converter MCP' will be always working at near saturation condition, in contrast to the 'bare MCP'.

It should also be mentioned that the secondary particles generated from the CuBe converter also include secondary electrons. From previous studies, the emission efficiency of secondary electrons decreases with the increasing of mass, but the emission efficiency of secondary ions is close to unity even for low velocities and independent of ion masses. In this experiment, both the secondary electrons and secondary ions produced from the converter are employed. When either of them is working at the unity emission condition as the change of the mass and energy of ions, the single ion counting method will record at most one event regardless of whether it is from secondary electrons or secondary ions. So the 'converter MCP' takes advantage of the unity emission efficiency from both secondary electrons and secondary ions, but mostly from the secondary ions for the energy per unit mass less than 1 eV/Da [19]. Due to the multiplicity and the high energy per unit mass of the secondary particles, the 'converter MCP' is always working in a 'saturated' mode, i.e., the detection efficiency of the 'converter MCP' is close to unity and independent of the ion mass of the primary ion. This makes the CuBe converter an ideal reference to characterize the detection efficiency of the MCP.

The distance between the converter and MCP is about 20 mm. The flight-time for secondary ions with mass of 100 Da is about 80 ns at -10.6 kV acceleration voltage, much shorter for lighter secondary ions or lower acceleration voltages. For the 'bare MCP', the primary ions will decelerate after passing through the grid on the intermediate electrode. The flight-time of the primary ions traveling from the gird to MCP is ~ 2 μs (for transferrin 79,500 Da, at -10.6 kV acceleration voltage). Therefore there will be about 2 μs time difference between the spectra recorded from the 'converter MCP' part and the 'bare

MCP' part for the ions with same mass.

The current signals collected on the anodes of the MCP detector are capacitively coupled (50 pF) to a pre-amplifier which, in turn, is connected to a constant fraction discriminator (CFD). It registers the pulses based on the shape of the pulses instead of their amplitudes. This improves the time resolution and sensitivity. Since more than one secondary particle might be generated from the converter and all these secondary particles belong to one primary ion striking, they all should be counted as one event. Therefore the single-ion counting method is designed to record at most one event no matter how many secondary particles are generated. This can be accomplished in two ways. One is to intentionally stretch the CFD time width to about 100 ns (dead time) so that only a single pulse is generated when one or more secondary particles are generated on the CuBe converter. An additional constraint can be applied using software so that at most one secondary particles within the selected range was registered for a given primary ion striking. The output of CFD is then fed into the time-to-digital converter (TDC) to record the spectrum.

5.2.3 Single ion counting

Measuring efficiency using single ion counting requires that no more than one primary ion strike the detector at a time. If two or more primary ions strike the detector simultaneously, only one pulse is recorded. In axial TOF measurement, an iris is normally used for this purpose. However, in the orthogonal TOF, as mentioned earlier, the quasi-continuous ion beam can be spread over many injections by setting a higher extraction frequency. Then the probability of producing multiple ions (particularly on the same anode) is much lower than the axial TOF system.

In spite of this, it is possible to produce multiple ions on a single anode, particularly with low mass species at high laser fluence. However, it is easy to avoid this by some complementary ways. First, the concentration of the sample can be decreased to reduce the number of ions produced. Second, the laser fluence can be set just above the threshold

since the ion yield is a power law dependence on the laser fluence in the low fluence range. Third, the ion optics can be finely tuned in order to make the ion beam evenly distributed over the four independent anodes.

Since the TDC employs single ion counting, at most one ion of a given m/z value is recorded whether one or more ions arrive at the detector at the same time. It is possible to detect distortion produced by high count rate from the isotopic distribution, but this is difficult to quantify. A better way to estimate the occurrence probability of one or more ions per injection pulse per anode for a given species is to calculate the average count rate per laser pulse. For example, Fig.5.5 shows the mass spectrum of substance P isotopes. The inset shows the ion count rate from each laser shot which contributes to the first isotope peak. The number of ions detected after each laser shot can be obtained by integrating the area of each peak, which is typically 0.05 s wide. The average number of ions is about 180 ions/shot, so the number of ions per injection pulse is about: $\frac{180}{0.05*5000} = 0.72$ ions/pulse. Considering there are four independent anodes, it becomes $0.72/4 \approx 0.18$ ions/pulse·anode. Assuming the multiplicity of ions per injection pulse per anode follows a Poisson distribution, the probability of n ions occurring can be expressed as:

$$P(n) = \frac{\mu^n}{n!}e^{-\mu} \tag{5.1}$$

where μ is average number of ions per injection pulse per anode,$n = (0, 1, 2...)$.

In this example, μ is equal to 0.18. The probability for zero, one and two ions per injection pulse per anode will be calculated as 0.835, 0.15 and 0.014, respectively. It is quite clear that the probability of having two ions per injection pulse per anode is 10× smaller than the probability of one ion. Thus multiple ions will produce at most a 10% correction, and this is mainly needed for small ions. This calculation gives an evidence that single ion counting works safely in the orthogonal TOF mass spectrometry.
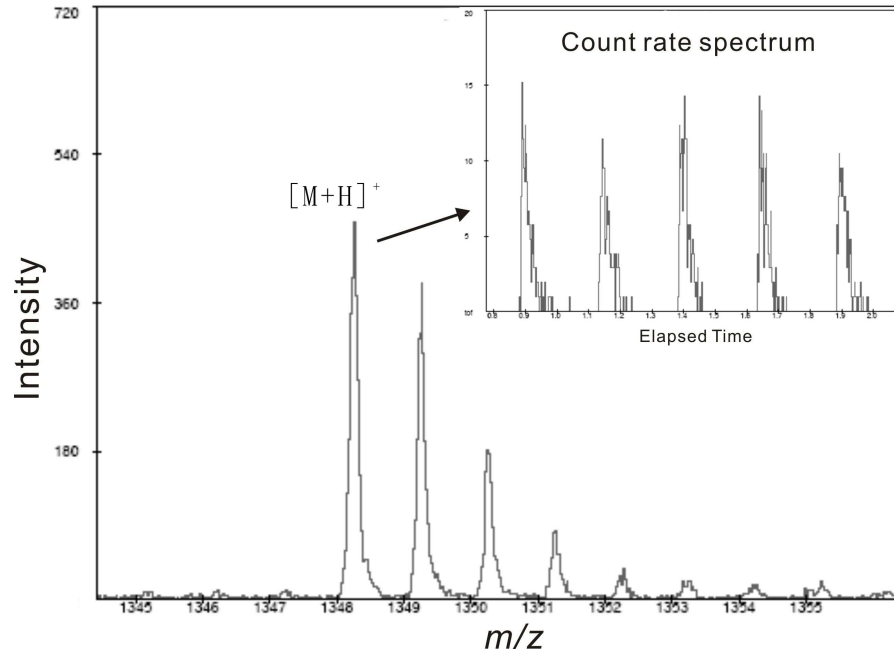
Figure 5.5: Spectrum of substance P. The inset shows the ion pulses from each laser shot which contribute to the first isotope peak of substance P.

5.2.4 Equations for data analysis

As described above, the orthogonal TOF geometry greatly reduces the probability of multiple ions striking the detector simultaneously and makes the single ion counting work very well. The secondary ion emission efficiency of CuBe converter is about unity and independent of the ion mass. Therefore the 'converter MCP' is suitable to calibrate the relative detection properties of the 'bare MCP'. Since both the 'converter MCP' and the 'bare MCP' have the same effective area, the comparison of the total ion counts from each MCP part allows direct measurement of the detection properties of the MCP, ϵ_{det}.

$$\epsilon_{det} = \frac{N_{MCP}}{N_{Converter}} \tag{5.2}$$

Where N$_{MCP}$ is the total number of ion counts from the 'bare MCP', N$_{Converter}$ is the total number of ion counts from the 'converter MCP'. These ion counts can be obtained

by integrating the area of ion peaks in the spectrum.

The fundamental physical quantity of interest is the secondary electron emission efficiency of MCP,ϵ_e, which is defined as the probability of detecting an ion (i.e. emitting one or more electrons) from the impact of a single molecular ion. The electron emission from the MCP follows the Poisson distribution [32], the probability of emitting n electrons from a single primary ion impact is

$$P_e(n) = \frac{\gamma_e^n}{n!}e^{-\gamma_e} \tag{5.3}$$

where γ_e is the secondary electron coefficient.

Based on the Poisson distribution, the secondary electron emission efficiency ϵ_e, corresponding to the probability of emitting one or more electrons from a single ion impact, can be expressed as

$$\epsilon_e = 1 - P_e(0) = 1 - e^{-\gamma_e}$$
$$\gamma_e = -ln(1 - \epsilon_e) \tag{5.4}$$

where $P_e(0)$ means there is no secondary electron emission. Thus, γ_e can be calculated from Eqn.(5.4). The dependence of γ_e on the mass 'm' and the velocity 'v' of the molecular ion will be discussed later.

5.3 Results and Discussion

5.3.1 Comparison between the 'converter MCP' and the 'bare MCP'

In this experiment the measurements have been made for a range of analytes from bacitracin to transferrin (from 1400 to 79,500 Da) and for a series of ion energies (4.6, 6.6, 8.6, and 10.6 keV). The ion beam was tuned by adjusting the ion optics to make it evenly distributed on the four anodes. The total number of ions from the first two channels ('converter MCP') and from the last two channels ('bare MCP') were examined to check the ion beam distribution. Once the instrument has been finely tuned, a series of analytes and different acceleration voltages have been examined on this detector.

First we made the comparison of mass spectra of transferrin (79,500 Da) acquired simultaneously from the 'converter MCP' and the 'bare MCP' with different acceleration voltages, shown in Fig.5.6. From these spectra, it shows that the intensity of ion peak from the 'converter MCP' is much higher than that from the 'bare MCP', although the ratio measured is much smaller than expected from earlier results [20].

As the acceleration voltage decreases from 10.6 kV to 6.6 kV, the intensity ratio between them increases rapidly from ~ 2.5 to ~ 10. This clearly demonstrates the advantage of using secondary ion emission instead of using secondary electron emission for large molecular ion detection. Assuming the CuBe converter has about unity secondary ion emission efficiency and the 'converter MCP' has constant detection efficiency, the decreasing intensity of the transferrin ion peak indicates that the secondary electron yield (detection efficiency) of the'bare MCP' decreases rapidly as the acceleration voltage decreases.

The mass scales (not labeled) are different in these cases because of different acceleration voltages. When the acceleration voltage goes down, the flight-time of transferrin becomes longer, so the spectra show that the molecular ion peak moves toward higher mass. The time delay between spectra from the 'converter MCP' and the 'bare MCP' is also obvious.
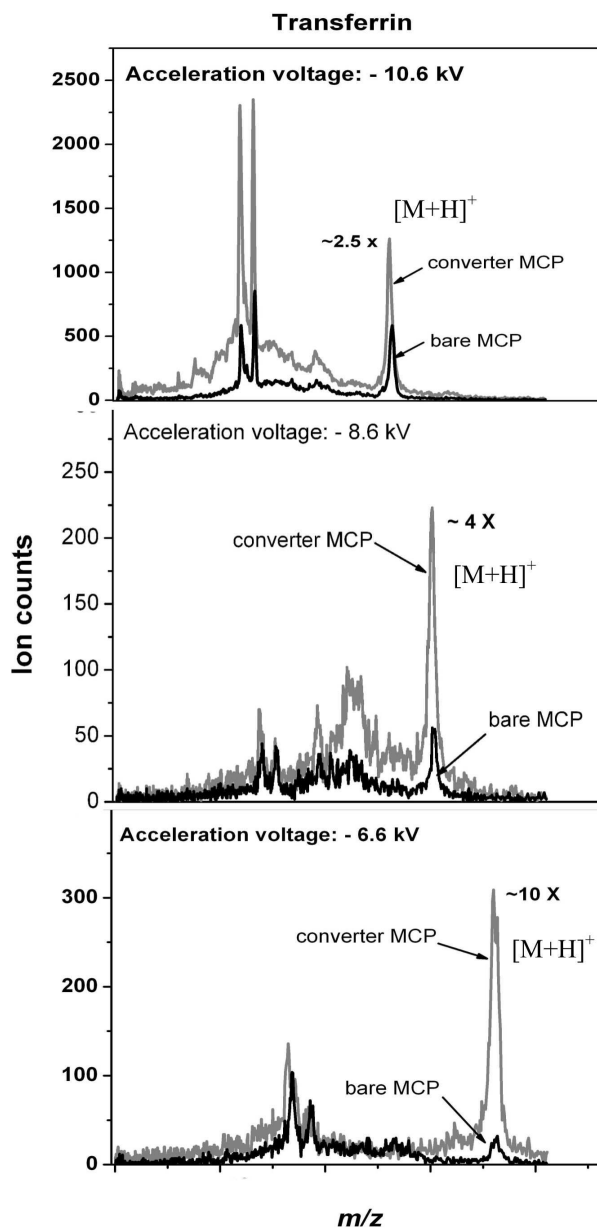
Figure 5.6: The comparison of mass spectra of transferrin from the 'converter MCP' and the 'bare MCP' at different acceleration voltages. It is obvious that the detection ability of 'bare MCP' drops rapidly with decreasing of the acceleration voltages, assuming that the detection efficiency of converter is close to unity.
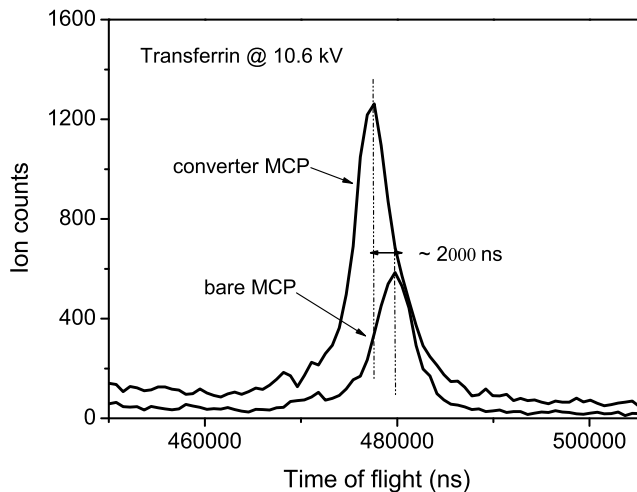
Figure 5.7: The time delay of transferrin detected from the 'converter MCP' and the 'bare MCP' at acceleration voltage of 10.6 kV. This time delay is due to the deceleration of the primary ions and the acceleration of the secondary ions from the intermediate electrode to the MCP. The flight-time is the total time of flight.

As mentioned earlier, the time delay is due to the fact that the deceleration of the primary ions and the acceleration of secondary ions when they travel from the intermediate electrode to the MCP. In the case of transferrin ion, the time difference is about 2 μs at -10.6 kV acceleration. The zoomed spectrum is shown in Fig.5.7. Due to the short distance ($\sim$ 20 mm) between the converter electrode and the MCP, secondary ion species cannot be resolved. The mass resolution of spectra from the 'converter MCP' becomes worse due to the multiple secondary ion species. This can be easily seen from the comparison of mass spectra for bacytracin (1400 Da), shown in Fig.5.8.
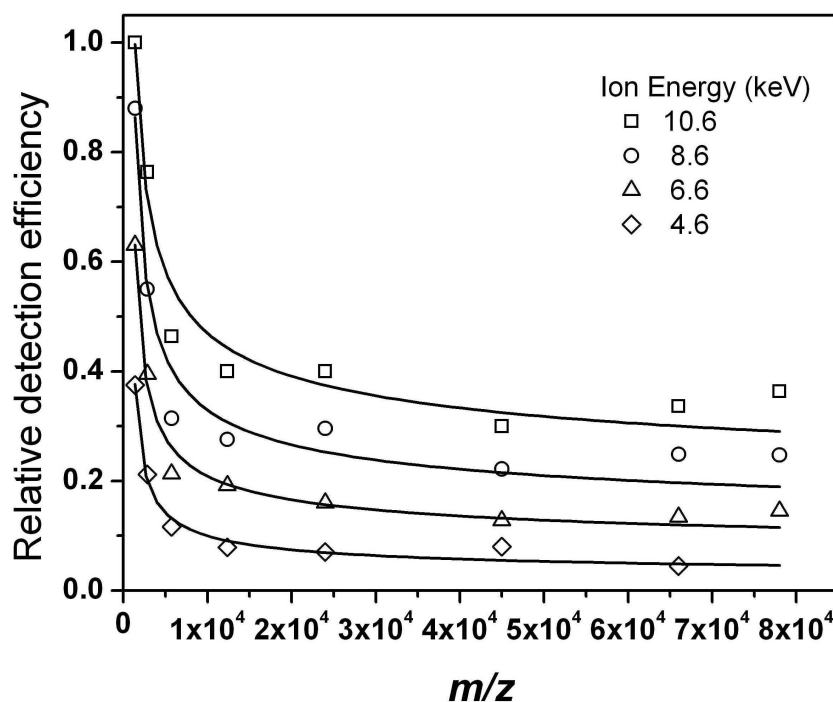
5.3.2 Detection efficiency of the MCP

The detection efficiency of the 'bare MCP', ϵ_{det}, was studied with a series of masses and acceleration voltages. It can be obtained by taking the ion count ratio between the 'bare MCP' and the 'converter MCP' assuming the secondary ion emission efficiency of the CuBe converter is 100% and the 'converter MCP' works always in the saturation
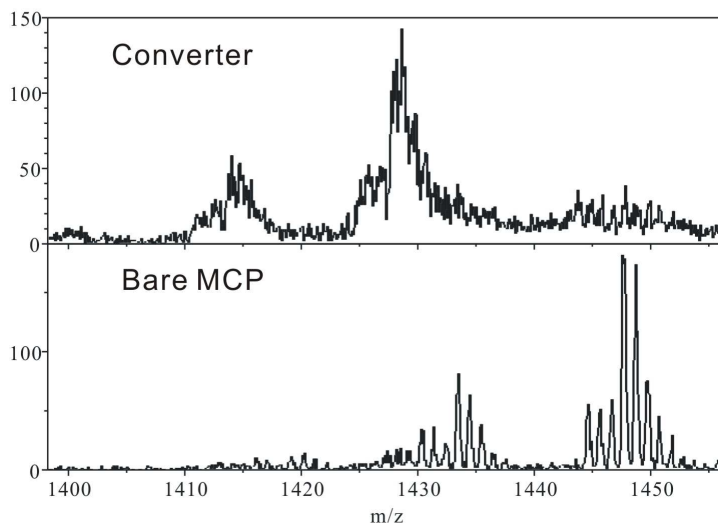
Figure 5.8: The comparison of spectra of bacytracin from the 'converter MCP' and the 'bare MCP' with respect to the mass resolution. The mass resolution from the 'converter MCP' is worse than that of the 'bare MCP' due to the multiple secondary ion species.

condition. The relative detection efficiency is plotted in Fig.5.9. Four data-sets are plotted corresponding to different energies of ions. The relative detection efficiencies at different acceleration voltages are normalized with respect to the efficiency at ion energy of 10.6 keV. This graph shows that the detection efficiency, ϵ_{det}, of the 'bare MCP' is a function of the ion mass and ion energy. It drops continuously with the increasing of ion mass for each of the given energy. The decreasing rate is much faster in the low mass range. For ion energy at 10.6 keV, the relative detection efficiency is about 100% for bacytracin ($\sim$ 1400 Da); it drops rapidly to about 50% for ion mass about 10,000 Da, and then drops gradually to about 40% for transferrin($\sim$ 79,500 Da). The trend seems consistent with the previous studies showing that the secondary electron emission is mainly dominant for the detection of small molecules and decreases with the increasing of ion mass [20, 22] although the absolute value is high here. For a given mass, the detection efficiency also drops when the acceleration voltage decreases. At $m/z \sim$ 66 kDa, the relative detection efficiency is about 34% at 10.6 keV (energy per unit mass: 0.16 eV/Da); the efficiency drops to only 8% at 4.6 keV (energy per unit mass: 0.07 eV/Da). The data were fit with

Figure 5.9: The relative detection efficiency of 'bare MCP' as functions of mass and energy of ions. The ion mass ranges from bacytracin(~ 1400 Da) to transferrin($\sim 79{,}500$ Da). The ion energies vary from 4.6 to 10.6 keV. The relative detection efficiency drops as the increase of ion mass and the decrease of ion energy. The curves were fit only as a guide for the eye.

a function $(A + B * x^C)^{-1}$ simply as a guide for the eye.

Although the dependence of detection efficiency of the MCP on ion mass and energy shows similar trend to previous measurements [11, 15], such high efficiency in the high mass range is not observed by others, and in contrast to previous results, the efficiency seems to level out or even increase slightly with increasing mass. We have observed that the efficiency is about 40% for transferrin ($\sim 79\,500$ Da) at 10.6 keV (0.13eV/Da), whereas this laboratory has reported 20% for secondary ions on CsI or on stainless steel for similar ion mass and energy, and Westmacott *et al.* reported only 1% for bovine albumin (66 kDa) for similar energy [15, 20]. Some effects might contribute to this discrepancy. First, we assumed that the secondary ion emission efficiency of the CuBe converter is about 100%, whereas it is actually close to 80% in the previous study [20]. This may decrease our measurement to some extent if taking this factor into account. Second, the potential

difference between the converter and the MCP changes with the change of acceleration voltages as discussed above. We assumed that the 'converter MCP' works in a saturation mode when secondary ions strike the MCP. However, the the minimum potential difference is about 1.4 kV when the acceleration voltage is about -10.6 kV. This energy might be not high enough to make the detection efficiency of the MCP reach saturation. This may also contribute to the relative higher efficiency we have observed. Third, as the primary ion increases in mass, a decrease in the relative intensity of secondary ion species was observed, causing an apparent shift to higher mass secondary ions [17]. Therefore the detection efficiency of the 'converter MCP' for the secondary ions will tend to decrease for high mass primary ions. This may result in an apparent increasing of MCP detection efficiency in the high mass range.
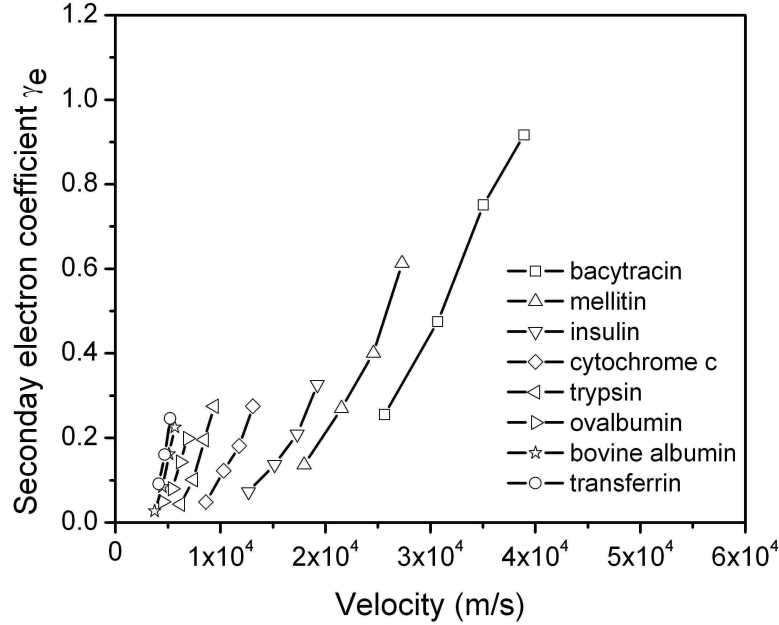
5.3.3 Reduced secondary electron coefficient of the MCP

The secondary electron emission efficiency, ϵ_e, is the probability of detecting an ion after one ion strikes the MCP. The secondary electron emission from a MCP follows a Poisson distribution as discussed above. The secondary electron coefficient, γ_e, can be calculated from Eqn.(5.4). The calculated secondary electron coefficient, γ_e, as a function of velocity is plotted in Fig.5.10.

For each molecular ion there are four data points which correspond to four different energies. It shows that the secondary electron coefficient increases with the ion velocity for a given species. And it also increases with the ion mass for a given velocity. As a result, it is possible to detect larger ions at a lower velocity. The 'threshold velocity' measured in this experiment is below 0.4×10^4 m/s, which is much lower than the previous measured ion detection 'threshold' velocity (1.8×10^4 m/s) [23, 25].

The secondary electron coefficient, γ_e, depends both on the mass of the molecular ion and its incident velocity. In order to separately study the dependence on the ion mass and velocity, the secondary electron coefficient was plotted as γ_e/m, the reduced secondary

Figure 5.10: Secondary electron coefficient γ_e as a function of the ion velocity. The molecular ions used range from bacytracin ($\sim$ 1400 Da) to transferrin ($\sim$ 79,500 Da).

electron coefficient, vs. the ion velocity which is shown in Fig.5.11. The data were fit using an exponential function $\gamma_e/m = Ae^{Bv}$ and a simple power law function. The curve denoted as 'Exponential fit1' is the best fit using the designated exponential function. It shows that the exponential function fits well only in the high velocity (low ion mass) region above 10,000 m/s. With the decreasing of ion velocity, this fit curve deviates significantly from the original data. The constants of 'A' and 'B' from this fit are about 8.9×10^{-6} and 1.1×10^{-4} which are quite different from the 'universal function' measured previously for the reduced γ_e of MCP impacted by some amino acid and small peptide molecular ions [11]. The 'universal function' was also plotted in Fig.5.11 denoted by 'Exponential fit2'. The expression of the 'universal function' is shown as follows:

$$\frac{\gamma_e}{m} = 2.58 \times 10^{-7}[e^{2.31 \times 10^{-4}v}] \tag{5.5}$$
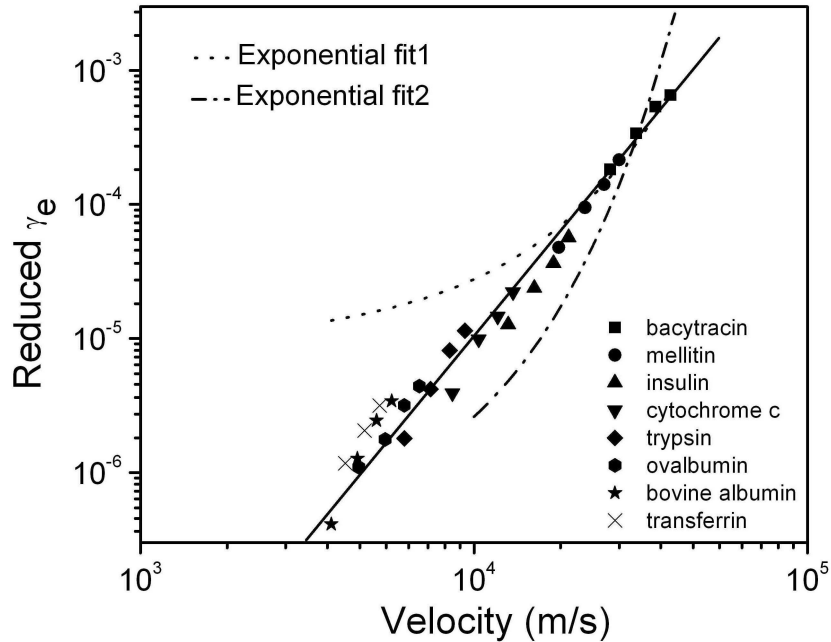
Figure 5.11: The reduced secondary electron yield as a function of the ion velocity. Exponential fit1 and Exponential fit2 are plotted with the same type of exponential function. The parameters for Exponential fit2 are from the previous measurements of the reduced γ_e of MCP [11]

It is obvious that the exponential function is not a good fit with the experimental data. However the reduced secondary electron coefficients fall on a straight line indicating a simple power law dependence,$\gamma_e/m = Av^B$. The slope, i.e. the exponent of the velocity, is found to be about 3.2 with our experimental data. The strong velocity dependence of the reduced secondary electron coefficient was also found in some other measurements. The measurement with a STJ detector in Lawrence Berkeley National Lab (LBNL) [15] gave a velocity exponent about 4.3 ± 0.4. Velocity exponents of 2.1 for stainless steel surface and 3.3 for CsI surface were obtained previously in our group [20]. The Orsay group measured a velocity exponent of 4 from CsI surface under the impact of large molecules [21]. The reduced secondary electron coefficient from different groups are plotted in Fig.5.12.

The reduced secondary electron coefficient falls on a straight line also indicates there is a linear mass dependence. This was also observed in other measurements from different surfaces such as MCP, Cu, CsI, and stainless steel [11, 20, 23]. The linear mass dependence of the reduced γ_e may indicate that the atoms of the incident molecular ions interact
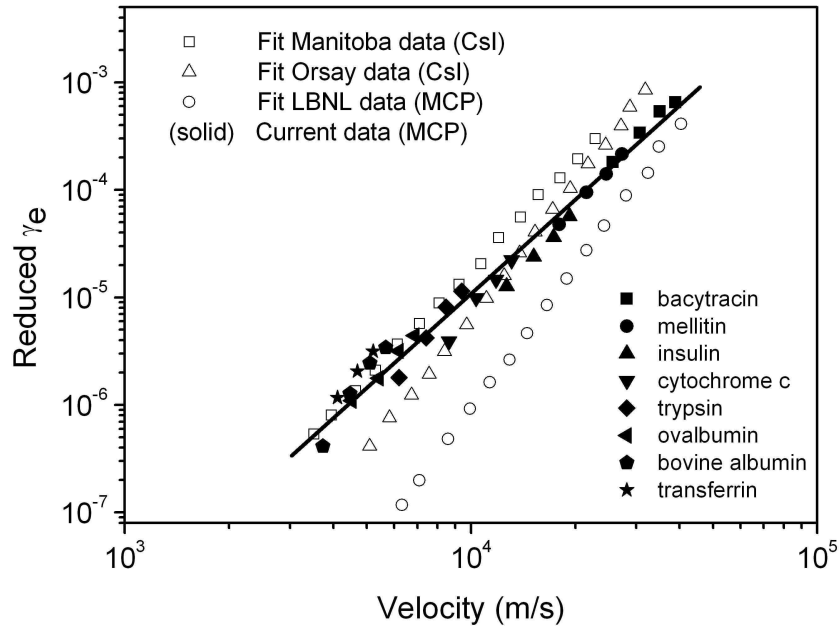
Figure 5.12: The reduced secondary electron coefficient as a function of the ion velocity. The data from different groups measured on different surfaces is also plotted. A power law of reduced γ_e on velocity is consistently shown with different velocity components.

independently on the surface, therefore the total collision effects of all atoms might be added up. However, deviation from the linear mass dependence was also found which showed that the mass dependence is correlated to the velocity regime, the size of the projectiles, and the material of the collision surface [25]. For the oxide surface such as Al_2O_3 struck by the water clusters, the reduced γ_e does not obey the additive relationship [25]. There is a sublinear dependence as a function of the mass which is close to $M^{0.7}$. A similar sublinear power dependence was also observed for the CsI surface at velocities from 1.5×10^4m/s to 7×10^4m/s [21].

The above comparison from different measurements of the reduced γ_e shows that it is more like a power law rather than an exponential relation with respect to the ion velocity. There is also a linear or sub-linear mass dependence from the different measurements. A steep velocity dependence is observed for all these measurements but with a large variation of the velocity exponents of 2.1 - 4.3. This variation could come from differences of the striking surfaces used in the experiments. In these measurements, MCP, stainless,

Cu, and CsI surfaces have been examined. It is well known that the CsI surface gives a significant enhancement in the ion and electron yield compared to the stainless steel surface when the incident energy per unit mass is >1 eV/Da [19, 33]. This is true even after both surfaces have been exposed to atmosphere and examined at 10^{-6} Torr, although the enhancement decreases with prolonged exposure to the atmosphere [19]. The CsI surface could also change rapidly under vacuum during the first hours with a decrease of the ion and electron emission yield for certain ions. This drop is probably due to a modification of the CsI surface owing to a molecular water deposit found in vacuum instruments. There is then a slow change over a period of two weeks [21]. There might be difference in secondary electron coefficient for different type of MCP. It may degrade gradually for a long period of usage. So the difference of the target surface and the surface condition may result in the different secondary electron coefficient and the different velocity dependence.

The different experimental setups may also affect the measurements on the velocity dependence. In our experiment, an orthogonal-injection MALDI TOF mass spectrometer with a reflection mirror is used which greatly reduced the number of ions reaching to the detector per pulse. So single ion counting method can be used safely. The other experiments used an axial TOF mass spectrometer. The multiplicity of the incident ions may be increased. In the different instrument geometry, the ion beam strikes the surface with different angles. It was about 45° between the primary ion beam and the conversion surface (CsI or stainless steel) in the previous measurement in our lab [17, 19]; the ion beam perpendicularly strikes the CsI surface in the Orsay group [21]; for the MCP measurement with a STJ detector, the titled angle of the MCP channels is about 8° from the direction of the ion beam which is about the same as our experiment [15].

In summary, one or more of these factors may affect the secondary electron coefficient which gives the difference of the velocity exponents in the power law relationship.

5.4 Conclusion

In this chapter, the detection efficiency and secondary electron emission properties of the MCP detector was studied in an orthogonal-injection MALDI TOF mass spectrometer. Single ion counting method was used safely to avoid the difficulty of interpreting the analogue data obtained with axial TOF system. A hybrid detector composing of a MCP and a CuBe venetian blind converter was used. The CuBe blind converter provides a normalization for the detection efficiency of the MCP. The measurements show that the detection efficiency of the MCP drops with the increasing of ion mass and the decreasing of the ion energy. The secondary electron coefficient shows a linear dependence on mass and a power law dependence ($\sim$3.2) on velocity. Electron emission from the MCP was observed for primary ion striking with velocity $\sim$ 4 km/s, which is much lower than the previous measured ion detection 'threshold' velocity (1.8×10^4 m/s), showing no clear evidence of a velocity threshold.

References

[1] Wiza, J. L. *Nucl. Instrum. Methods* **1979**, *162*, 587–601.

[2] Colson, W. B.; Mcpherson, J.; King, F. T. *Rev. Sci. Instr.* **1973**, *44*, 1694.

[3] Gao, R. S.; Gibner, P. S.; Newman, J. H.; Smith, K. A.; Stebbings, R. F. *Rev. Sci. Instrum.* **1984**, *55*, 1756–1759.

[4] Muller, A.; Djuric, N.; Dunn, G. H.; Belio, D. S. *Rev. Sci. Instrum.* **1986**, *57*, 349–353.

[5] Brehm, B.; Grosser, J.; Ruscheinski, T.; Zimmer, M. *Meas. Sci. Technol.* **1995**, *6*, 953–958.

[6] Oberheide, J.; Wilhelms, P.; Zimmer, M. *Meas. Sci. Technol.* **1997**, *8*, 351–354.

[7] Hellsing, M.; Karlsson, L.; Andren, H. O.; Norden, H. *J. Phys. E: Sci. Instrum.* **1985**, *18*, 920–925.

[8] Yagia, S.; Nagata, T.; Koideb, M.; Itohc, Y.; Koizumid, T.; Azumae, Y. *Nucl. Instrum. Methods B* **2001**, *183*, 476–486.

[9] Fraser, G. W.; Pain, M. T.; Lees, J. E.; Pearson, J. F. *Nucl. Instrum. Methods A* **1991**, *306*, 247–260.

[10] Barat, M.; Brenot, J. C.; Fayeton, J. A.; Picard, Y. J. *Rev. Sci. Instrum.* **2000**, *71*, 2050–2052.

[11] Geno, P. W.; Macfarlane, R. D. *Int. J. Mass Spectrom. Ion Processes* **1989**, *92*, 195.

[12] Gilmore, I. S.; Seah, M. P. *Int. J. Mass Spectrom.* **2000**, *202*, 217–229.

[13] Karas, M.; Hillenkamp, F. *Anal. Chem.* **1988**, *60*, 2299–2301.

[14] Tanaka, K.; Waki, H.; Ido, Y.; Akita, S.; Yoshida, Y.; Yoshida, T. *Rapid. Commun. Mass Spectrom.* **1988**, *2*, 151.

[15] Westmacott, G.; Frank, M.; Labov, S. E.; Benner, W. H. *Rapid Commun. Mass Spectrom.* **2000**, *14*, 1854–1861.

[16] Spengler, B.; Kirsch, D.; Kaufmann, R.; Karas, M.; Hillenkamp, F. *Rapid Commun. Mass Spectrom.* **1990**, *4*, 301.

[17] Martens, J.; Ens, W.; Standing, K. G.; Verentchikov, A. *Rapid Commun. mass spectrom.* **1992**, *6*, 147–157.

[18] Brunelle, A.; Chaurand, P.; Della-Negra, S.; LeBeyec, Y.; Baptista, G. P. *Int. J. Mass Spectrom.* **1993**, *126*, 65.

[19] Verentchikov, A.; Ens, W.; Martens, J.; Standing, K. G. *Int. J. Mass Spectrom. Ion Processes* **1993**, *126*, 75–83.

[20] Westmacott, G.; Ens, W.; Standing, K. G. *Nucl. Instrum. Methods B* **1996**, *108*, 282–289.

[21] Brunelle, A.; Chaurand, P.; Negra, S. D.; Beyec, Y. L.; Parilis, E. *Rapid Commu. Mass Spectrum.* **1997**, *11*, 353–362.

[22] Spengler, B.; Kirsch, D.; Kaufmann, R.; Karas, M.; Hillenkamp, F.; Giessmann, U. *Rapid Commun. Mass Spectrom.* **1990**, *4*, 301–305.

[23] Beuhler, R. J.; Friedman, L. *Nucl. Instrum. Methods B* **1980**, *170*, 309.

[24] Hedin, A.; Hakansson, P.; Sundqvist, B. U. R. *Int. J. Mass Spectrom. Ion Processes* **1987**, *75*, 275.

[25] Beuhler, R. J. *J. Appl. Phys.* **1983**, *54*, 4118–4126.

[26] Hillenkamp, F.; Karas, M.; Beavis, R. C.; Chait, B. T. *Anal. Chem.* **1991**, *63*, 1193A.

[27] Haberland, H.; Winterer, M. *Rev. Sci. Instr.* **1983**, *54*, 764–765.

[28] Wenzel, R.; Plet, B.; Nazabal, A.; In *Abstract of the Desorption meeting in 2008,*, June,2008.

[29] Frank, M.; Labov, S. E.; Westmacott, G.; Benner, W. H. *Mass Spectrom. Rev.* **1999**, *18*, 155–186.

[30] Chernushevich, I. V.; Ens, W.; Standing, K. G. *Anal. Chem.* **1999**, *71*, 452A–461A.

[31] Hillenkamp, F.; Karas, M.; In *Proceedings of the 37th ASMS Conference on Mass Spectrometry and Allied Topics*, May,1989; p 1168.

[32] Toglhofer, K.; Aumayr, F.; Kurz, H.; Winter, H.; Scheier, P.; Mark, T. D. *Nucl. Instrum. Methods B* **1994**, *88*, 44–48.

[33] Della-Negra, S.; Deprun, C.; LeBeyec, Y. *Rapid Commu. Mass Spectrum.* **1987**, *1*, 10.

Chapter 6

Conclusions

It has been about 20 years now since the introduction of MALDI mass spectrometry [1, 2]. It is still one of the most powerful analytical tools in biomolecular analysis [3]. However, some fundamental mechanisms related to MALDI process are still not fully understood. The more we know about it, the better we can take advantage of it. This thesis reported some systematic fundamental studies about the MALDI mass spectrometry mainly from three aspects: the analyte distribution in MALDI sample preparation, the influence of laser properties on laser desorption/ionization, and the ion detection properties of MCP detector.

All these experiments were performed on orthogonal-injection MALDI TOF mass spectrometers. The advantages of this geometry, such as collisional cooling, decoupled ion source, and single ion counting make it suitable for these fundamental studies. More comprehensive and precise measurements can be performed compared to those with axial TOF instruments.

The analyte distribution was first studied with high resolution MALDI imaging technique. Compared with the previous techniques, the essential advantage of this method is that it is a label-free technique and the analyte distribution can be directly studied. This study clearly demonstrates that the single analyte molecules are homogeneously incorporated into matrix crystals instead of adsorbed on the matrix crystal surface for 2,5-DHB matrix.

We observed no surface preference and mass discrimination for the analyte incorporation. These findings clarify some previous controversies about the analyte distribution. The comparison of analyte distribution with different sample preparations also sheds some light on choosing suitable matrix and sample preparation methods for better sensitivity and signal reproducibility. The studies on the hydrophobicity-related analyte segregations also allow us to understand the interaction between the analytes, and help to optimize the sample preparation in MALDI, especially in tissue imaging.

Good sample preparation is a prerequisite for successful MALDI mass spectrometry. The ion desorption/ionization is another important step for getting better mass spectrum. The laser properties play a major role in this step. In this thesis, the laser properties such as the laser beam profile, the laser fluence, and the laser beam spot size have been systematically studied. These studies also provide some useful suggestions for the MALDI imaging experiments in terms of sensitivity and spatial resolution.

The N_2 laser generally gives a better sensitivity than the Nd:YAG laser. Studies on laser beam profiles shows that the uniformity of the laser beam profile mainly contributes to the different performance between these two lasers. We found that twisting the fiber during irradiation or using a longer fiber can improve the uniformity of the laser beam profile and therefore reduce the difference between the two lasers essentially. This also indicates that in imaging experiments where the beam is rastered across the sample continuously instead of irradiating discrete spots, an averaging effect similar to twisting the fiber is achieved.

Since a much higher laser fluence can be used in an orthogonal-injection TOF instrument without sacrificing performance than the axial TOF in which near threshold fluence is typical, the laser fluence and spot size dependence of sensitivity can be studied in a much wider range in this experiment. It shows that sensitivity increases rapidly with fluence and gradually reaches saturation at high fluence range due to fragmentation and possible reduced transmission as a result of interactions in the dense plume. A strong area dependence (cubic) is found at fluence near threshold, consistent with previous measurements,

which has suggested to some that small spot sizes are not practical in MALDI and limit the spatial resolution in MALDI imaging experiments. However, an area dependence close to linear is observed in the high fluence range, indicating that the best sensitivity can be obtained with the smallest fiber because saturation occurs at high laser fluence. This has been demonstrated by scanning a defined area with two different size fibers. Smaller fibers show consistently higher sensitivity than larger ones. This study also suggest that in imaging experiments, continuous rastering mode is better than irradiating discrete spots and smaller scan step size is better than large one since in both cases new sample materials are exposed a little at a time, exhibiting behavior consistent with a smaller spot.

Once molecular ions are generated, ion detection becomes extremely important. Since the MCP is one of the most widely used detector in mass spectrometry, the detection properties of the MCP was comprehensively studied with a hybrid MCP and CuBe venetian blind converter detector. The orthogonal-injection TOF instrument is particularly suitable for this measurement because single ion counting method can be used without any ambiguity and avoid the difficulty in interpreting the data. The relative detection efficiency of the MCP decreases rapidly with the mass and energy of ions. This is fundamentally due to the decrease of the secondary electron emission efficiency of the MCP. The secondary electron coefficient of MCP shows a linear dependence on mass and a power law dependence ($\sim$3.2) on velocity. This experiment also clearly demonstrates the much higher detection efficiency of the CuBe converter especially for high molecular ions, indicating that the potential of using secondary ion emission for high mass ion detection.

The research works in this thesis also have some practical applications on the mass spectrometry. The novel design of MALDI imaging ion source utilizing an orthogonal laser irradiation makes much smaller laser spot size achievable. This ion source can be easily adapted onto the current commercial QqTOF mass spectrometry system for high resolution MALDI imaging experiments. The study of the influence of the laser beam profile, laser fluence and spot size on the MALDI performance first proves that the Nd:YAG laser can be used in the MALDI imaging experiments with compatible sensitivity as the N_2 laser with fiber optics. An electronic device can be designed to automatically twisting

the fiber during the laser irradiation in order to generate a time-averaged uniform laser energy distribution and therefore to improve the sensitivity. Small laser spot size has been demonstrated to produce not only higher sensitivity but also higher spatial resolution in an orthogonal TOF mass spectrometer, which was thought to be not applicable for MALDI imaging according to the experimental results with an axial TOF mass spectrometer. The study also suggests that in MALDI imaging experiments the continuous rastering mode is much better than irradiating discrete spots since similar effects as twisting the fiber and using smaller spot size can be achieved. All these studies can be used as guidance to optimize the quality of MALDI images for the continuing MALDI imaging experiments in our group. The study on the MCP detection efficiency gives direct comparison of two types of detectors and indicates that detectors using secondary ion emission are much better than that using secondary electron emission for high molecular ion detection. In fact some commercial detectors using secondary ion emission has been recently designed for high mass detection by some companies.

In summary, this thesis systematically studied some fundamental aspects from analyte distribution, laser desorption /ionization, and ion detection in MALDI mass spectrometry. It not only provides some substantial proofs for the previous studies, but gives some new insights about the fundamental mechanisms of MALDI mass spectrometry. It also helps to optimize the performance of MALDI mass spectrometry and MALDI imaging mass spectrometry.

References

[1] Karas, M.; Hillenkamp, F. *Anal. Chem.* **1988**, *60*, 2299–2301.

[2] Tanaka, K.; Waki, H.; Ido, Y.; Akita, S.; Yoshida, Y.; Yoshida, T. *Rapid. Commun. Mass Spectrom.* **1988**, *2*, 151.

[3] Hillenkamp, F.; Karas, M.; Beavis, R. C.; Chait, B. T. *Anal. Chem.* **1991**, *63*, 1193A–1203A.